![Energy Dynamics Laboratory — EDL — Utah State University Research Foundation]

Final Report:
Uinta Basin Winter Ozone and Air Quality Study

December 2010 - March 2011

Submitted To:
Uintah Impact Mitigation Special Service District
320 North Aggie Boulevard
Vernal, Utah 84078

Submitted By:
Energy Dynamics Laboratory, Utah State University Research Foundation (USURF)
Bingham Research Center
320 North Aggie Boulevard
Vernal, Utah 84078

Randal Martin, Utah State University, Utah Water Research Laboratory
Kori Moore, Utah State University Research Foundation, Energy Dynamics Laboratory
Marc Mansfield, Utah State University Research Foundation, Energy Dynamics Laboratory
Scott Hill, Utah State University Research Foundation, Energy Dynamics Laboratory
Kiera Harper, Utah Division of Air Quality, Air Monitoring Center
Howard Shorthill, Utah State University Research Foundation, Energy Dynamics Laboratory

ACKNOWLEDGEMENTS

Finally, and most importantly, we are indebted to those who have gone above and beyond in facilitating monitor siting and access assistance.

- Mayor Clyde Watkins and Shawn Keel, Altamont city
- Mike Lefler, Duchesne Co. Fire & Emergency Management
- Day DeLaHunt and Heather Campbell, Split Mountain Garden Center
- Tyler McKee, Dax Nyberg, and Lapoint city firefighters
- Matt Mahler, QEP
- Jeremy Raymond, Uintah County Fire Marshall
- Enefit American Oil
- Oil Shale Exploration Company
- Utah Bureau of Land Management
- Utah Division of Air Quality

Table of Contents

EXECUTIVE SUMMARY

The Uintah Impact Mitigation Special Service District (UIMSSD) enlisted a team from Utah State University Research Foundation's (USURF) Energy Dynamics Laboratory (EDL) and Utah State University's (USU) Department of Civil and Environmental Engineering to perform an air quality monitoring program to measure baseline ozone concentrations. The program consisted of two integrated elements: (1) a three-month winter ozone monitoring program throughout the Uinta Basin and (2) a more intensive, week-long monitoring program that simultaneously measured ozone, volatile organic compounds (VOCs), nitrogen oxide pollutants (NO_x), fine particulate matter with a diameter less than 2.5 micrometers ($PM_{2.5}$), and vertical profiles of relevant meteorological parameters during a strong winter inversion event at two sites.

Ozone concentrations were measured at 18 locations throughout the Basin during the three-month monitoring program. Eight of the locations had previously established ozone-monitoring stations operated by outside agencies. The other ten locations utilized 2B Technology Model 205 Dual-Beam ozone monitors installed by the EDL-USU team specifically for this study. EDL-USU monitors were strategically located to provide adequate spatial coverage, to account for variations in topography and meteorology, and to avoid results bias due to proximity of potential ozone precursor sources. Every two weeks, the monitors were serviced, data were collected, and recalibrations were performed (if necessary).

The results of the Basin-wide winter ozone study showed elevated wintertime ozone concentrations throughout most of the Uinta Basin during wintertime temperature inversion events. The inversion events had the effect of reducing the vertical movement of the precursors involved in the formation of ozone, resulting in increased ozone formation below the inversion layer. Low surface winds (< 2 m/s) within the inversion layer were also observed throughout the Basin during periods of elevated ozone levels. Low surface winds limited the horizontal movement and dispersion of precursors and pollutants.

Although the data collected for this study cannot be used for regulatory purposes, a high number of 8-hr National Ambient Air Quality Standard (NAAQS) exceedances were observed at multiple locations throughout the Basin, with the fewest exceedances occurring in the higher elevations along the periphery of the study area. The highest ozone values typically were observed in the area centered along the Ouray/Pariette Draw locations and extending north to the Cedarview/Lapoint area, east to the Red Wash area, and west to Duchesne. The highest 1-hr value was observed at Ouray (149 ppb), and Pariette Draw was the site of both the highest observed 8-hr value (134.6 ppb) and the greatest observed fourth-highest (regulatory) ozone value (121.6 ppb). The highest number of 8-hr exceedances (25) was observed at both Ouray and Horse Pool. And while Fruitland and Nine Mile Canyon were the only sites to show no exceedances of the 8-hr standard, the Altamont, Rabbit Mountain, and Rangely, CO, sites (one, three, and three exceedances, respectively) would also be considered attainment areas under the current ozone NAAQS.

These results from the study suggest that the ozone concentrations observed during the wintertime inversion periods are a function of local topography, meteorology, and ozone precursor abundance rather than of any exterior mid- or long-range transport. Results also showed that the lower elevation monitoring locations with the greatest number of nearby wells tended to have the highest ozone concentrations (1-hr and 8-hr averages) and the greatest number of NAAQS exceedances. Locations at higher elevations, approximately 5500-6000 ft above sea

level (asl), had relatively few exceedances despite being near significant numbers of oil and gas wells.

The long-term, Basin-wide ozone measurement was supplemented with a short, high-intensity effort focused on the collection of $PM_{2.5}$, NO_x, and VOCs concentrations during a strong winter inversion event. This intensive monitoring portion of the winter ozone study was conducted from February 21 through February 25, 2011 at the Red Wash and the Vernal/Jensen sites. Ambient samples of NO_x, $PM_{2.5}$, non-methane hydrocarbons (NMHC)/VOCs, and vertical meteorological parameters (temperature, pressure, wind speed, and wind direction) were collected at both sites. Though not part of the proposed study, grab samples for methane analysis (whole air vials) were collected at both sites, and vertical ozone data were taken at Red Wash.

NO_x measured highest at the Vernal location but at levels typical of rural/semi-urban areas. The NO_x measurements also displayed a typical traffic-related diurnal profile. All measured levels of NO_2 were well below the 100 ppb, 1-hr NAAQS. Also, an observed dominance of NO_2 suggests the presence of a readily oxidized air mass, indicating that plenty of ozone was available to convert initially emitted NO to NO_2.

The CH_4 concentrations measured at Vernal were consistent with Northern Hemispheric background levels (1.7-1.8 ppm). The observed CH_4 concentrations at Red Wash (2.7-5.5 ppm) were significantly above the Northern Hemispheric background levels. CH_4 is usually considered non-reactive due to its relatively slow reaction rates, but at such elevated levels, CH_4 could be a significant player in atmospheric photochemistry of ozone formation in the Basin. Measured levels of NMHC at the Red Wash location were more than twice the observed concentrations at the Vernal site. The measured ratio of indicator compounds, benzene-to-toluene, is suggestive of oil and gas exploration and production.

Observed $PM_{2.5}$ concentrations were well below the NAAQS (35 $\mu g/m^3$) at both Vernal and Red Wash, but concentrations at the Vernal location were approximately twice those of the Red Wash location. These results are inconsistent with measurements previously observed by the Utah Division of Air Quality (UDAQ) that showed some exceedances of NAAQS in Vernal in the mid-2000s. The chemical composition of the particulate matter measured at both sites was approximately 80% carbonaceous material, with just under 70% being organic carbon (as opposed to elemental/black carbon). This percentage indicates an abundance of long-chain VOCs characteristic of the oil and gas industry.

Vertical meteorology measurements at the Red Wash site indicate that during an inversion event, the mixing height (surface layer) was on the order of 20-80 m (65-265 ft) above ground level (agl) and was dependent on time of day; vertical ozone data also show similar surface layer depths and patterns. Meteorological data indicate that horizontal winds were light (< 2 m/s) during inversion conditions throughout the Uinta Basin. The higher elevation areas, > 6500 ft above sea level (asl), showed more variable wind directions and higher wind speed during the same period. These higher elevation areas were probably located above the inversion. Limited vertical ozone profiles observed at the Red Wash location showed higher levels of ozone near the ground, an indication that ozone is being formed at ground level rather than from precursors being transported into the Basin.

Meteorological stations at lower elevations (<6500 ft asl) within the Basin indicated that horizontal winds were generally light (< 2 m/s) during inversion conditions. The higher elevation stations (> 6500 ft asl) showed wind data more consistent between sites and at higher

---

wind speeds than those at lower elevations. This finding suggests that the surface level winds within the lower elevation areas of the Basin, where the temperature inversions and elevated ozone concentrations were measured, were effectively disconnected from the regional air flow.

Modeling of winter ozone was performed as part of this project. The results of these efforts indicated several concerns about the chemical mechanisms used for modeling ozone reactions. For these calculations, a base model was designed to simulate a late-winter day, Feb. 20, 2008 in the Upper Green River Basin (UGRB). Three concerns were identified from these modeling efforts: 1) current mechanisms neglect temperature dependence of all photolytic reactions; 2) many reactions appear with negative activation energies, an indication that their rates may not extrapolate well to lower temperatures; and 3) many non-photolytic reactions also appear without temperature dependence, which probably indicated that they were only measured at a single temperature in the vicinity of 300 K. These concerns may lead to a positive bias in modeled levels of ozone of up to 10 ppb.

LIST OF FIGURES AND TABLES

1.   INTRODUCTION

1.1   BACKGROUND

During the winter of 2009-10 in the Uinta Basin, limited air quality monitoring revealed periods of elevated daytime ozone concentrations exceeding the current NAAQS established by the U.S. Environmental Protection Agency (EPA) (data are available on the EPA Air Explorer website, http://www.epa.gov/airexplorer/). Eight-hour averages above 100 ppb were measured during some days, exceeding the current 75 ppb NAAQS for surface ozone. Although the Uinta Basin 2009-10 winter measurements were not made at regulatory stations, the results raised concerns regarding the winter ozone levels in the region. Of particular concern was the potential impact these ozone levels might have on the health of Uinta Basin residents. Concern was also expressed that a failure to meet NAAQS for ozone levels could result in a nonattainment designation for Uinta Basin's counties, a consequence that could severely impact the economy of eastern Utah and the State as a whole. Such pressing concerns moved the Uintah Impact Mitigation Special Service District (UIMSSD) to obtain additional information and understanding about the levels of ozone and associated species in the Uinta Basin.

1.1.1   Problem Statement

At present, UDAQ has yet to determine the cause(s) of the elevated ozone readings from the winter of 2009-10 but has expressed concerns (http://www.airquality.utah.gov) that oil and gas development and production in the Basin may play a significant role. The uncertainty regarding the cause(s) of the elevated ozone levels stems from the region's lack of sound, continuous ambient air quality data. Prior to this study, the existing air monitoring data was very sparse, a fraction of the data necessary to make accurate and successful policy decisions.

If similar ozone levels are measured in subsequent years, the EPA could designate the Uinta Basin as a nonattainment area, and the potential impact on development and utilization of the Basin's energy resources due to air quality is of major concern to the local communities. Such restrictions would significantly impact not only the economy of the Basin but the economies of the State of Utah and of the region as a whole. The potential negative impacts of elevated ozone levels on the health of residents and on the economic development in the Basin compelled the UIMSSD to fund this study to measure ozone, associated species, and meteorological data during the winter months of 2010-11. The main objectives of the study were to establish the geographical extent and significance of elevated ozone within the Uinta Basin and to provide insight into possible anthropogenic influences and mitigation options. The additional data will help to characterize the Basin's wintertime ozone pollution (as a baseline dataset) and to help direct future ozone studies and mitigation strategies, activities and technologies.

The results of this study also provide information to help guide comprehensive, long-term airshed monitoring, analysis, and modeling programs to adequately understand winter ozone formation in the Uinta Basin and to help develop and implement appropriate mitigation strategies.

The UIMSSD enlisted a team from Utah State University Research Foundation's (USURF) Energy Dynamics Laboratory (EDL) and Utah State University's (USU) Environmental Engineering Department to perform an air quality monitoring program to measure baseline ozone concentrations in the Uinta Basin during the winter months of 2010-11. The program consisted

of two integrated elements: (1) a three-month Basin-wide winter ozone monitoring program and (2) a more intensive, week-long monitoring program at two selected sites that simultaneously measured ozone, volatile organic compounds (VOCs), nitrogen oxide pollutants (NO_x), fine particulate matter with a diameter less than 2.5 micrometers ($PM_{2.5}$), and vertical profiles of relevant meteorological parameters during a strong winter inversion event. It should be noted that the measured concentrations of ozone and $PM_{2.5}$ **were** not regulatory data and cannot be used in determining the attainment/nonattainment status of the counties of the Uinta Basin with respect to these pollutants.

1.1.2   Ozone Environmental Regulations

Oxygen exists in several allotropic forms, the most important being ordinary oxygen (O_2) and ozone (O_3) comprised, respectively, of two and three atoms per molecule. Ozone is a strong oxidizing compound found naturally in both the stratosphere and troposphere that readily reacts with most molecules and surfaces. It is also a known health hazard and often contributes to air quality problems in major cities throughout the world (Finlayson-Pitts and Pitts, 2000). For example, maximum ozone levels in Mexico City from 2000 to 2006 were measured above 200 ppb (Sanchez and Garfias, 2008), well above the natural tropospheric background concentrations of 20-40 ppb (Finlayson-Pitts and Pitts, 2000; Seinfeld and Pandis, 2006). Ironically, ozone is also critical to the preservation of life on earth because the so-called ozone layer (in the stratosphere at altitudes from about 15 to 40 km) absorbs nearly 99% of the harmful ultraviolet radiation produced by the sun (Finlayson-Pitts & Pitts, 2000, p. 56).

The U.S. Environmental Protection Agency (EPA) is authorized by the Clean Air Act (CAA) and its amendments to set ambient air quality standards for pollutants of primary concern with respect to impacts on human health at levels sufficient to protect the health of at-risk members of the population (i.e., children, elderly, and those with compromised health), based on the best available science. Even at low concentrations, ozone has been shown to adversely affect human health by irritating the linings of the nasal, throat, and lung passages, irritating the eyes and skin, reducing lung functionality, and increasing susceptibility to respiratory illnesses (Ilhorst et al., 2004; EPA, 2006a, 2006b, 2007). Adverse effects on both short- and long-term mortality have also been detected (Bell et al., 2004; Jerrett et al., 2009). Due to these effects, ozone is one of the pollutants of primary concern, referred to as a "criteria pollutant," and currently has a NAAQS of 0.075 parts per million (ppm), or 75 part per billion (ppb), based on the three-year average of the fourth-highest daily maximum 8-hour average for each year (EPA, 2010a). The EPA is mandated by the CAA, however, to review NAAQS standards periodically in light of new scientific data, and the NAAQS value for ozone is currently under review, with announcement of a new, lower NAAQS (presumably in the 60 - 70 ppb range) anticipated as early as July 2011 (C&E News, 2010; EPA, 2011).

1.1.3   Ozone Photochemistry

Ozone does not have a significant direct emission source but instead is formed in the atmosphere when solar radiation initiates a series of chemical reactions between volatile organic compounds (VOCs) and nitrogen oxides (NO_x). As such, ozone is often referred to as a secondary pollutant. The VOCs and NO_x are considered precursor compounds, and their emissions are regulated as a means of controlling surface ozone concentrations. Consequently, measurements of VOCs, NO_x,

and relevant meteorological parameters (i.e., wind, temperature, water, incident sunlight) are important to understanding the ozone formation processes in a given region.

The overall reaction process for ozone formation may be represented in simplest form as adapted from Finlayson-Pitts and Pitts (2000):

$$VOC + NO_x + \text{sunlight} \rightarrow O_3 + \text{other products} \tag{Eq. 1-1}$$
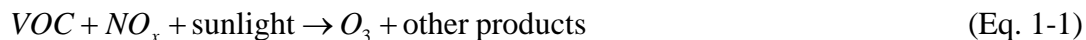
where "other products" may include nitric acid, aldehydes, peroxyacetyl nitrate and sulfate, nitrate particles, and others, many of which may further contribute to ozone production or destruction. Almost all of the sunlight responsible for these reactions occurs in the near ultraviolet (UV-A) wavelength. Finlayson-Pitts and Pitts (2000) and Seinfeld and Pandis (2006) describe detailed chemical reactions involved in ozone formation and destruction.

Sources of NO_x are generally combustion processes; VOCs are emitted from a variety of sources that include but are not limited to oil and natural gas production, liquid fuel or other solvent evaporation, incomplete fossil fuel combustion, and vegetative or biogenic processes (Finlayson-Pitts and Pitt, 2000). Since solar radiation provides the energy for many of these reactions, a diurnal pattern of ozone concentrations is typically evident with the lowest concentrations occurring in early morning and the highest concentrations in early to mid-afternoon. Temporal and spatial variations in the concentrations of ozone precursors, such as elevated NO_x emissions during rush hour, may affect diurnal ozone patterns.

Significant factors that contribute to the formation of ozone are the concentrations of ozone precursors, availability of solar radiation energy (a function of time of day, time of year, elevation, cloud cover, and surface albedo), and meteorological conditions (temperature, air movement, relative humidity, etc.). General conditions found to enhance the production of ozone above the NAAQS include but are not limited to stagnant high pressure systems (inversions), degree of cloud cover, high solar intensity, calm or low wind speeds, and abundant and widespread ozone precursor sources (Cooper and Alley, 2002). This combination of conditions has historically been found during the summertime in metropolitan areas such as Los Angeles, Houston, and Mexico City (Finlayson-Pitts and Pitts, 2000); however, unexpectedly elevated ozone concentrations were observed by the State of Wyoming Division of Air Quality in the Upper Green River Basin (see Fig. 1-1) that exceeded the NAAQS multiple times during January-March of 2005 and during several subsequent winter periods.
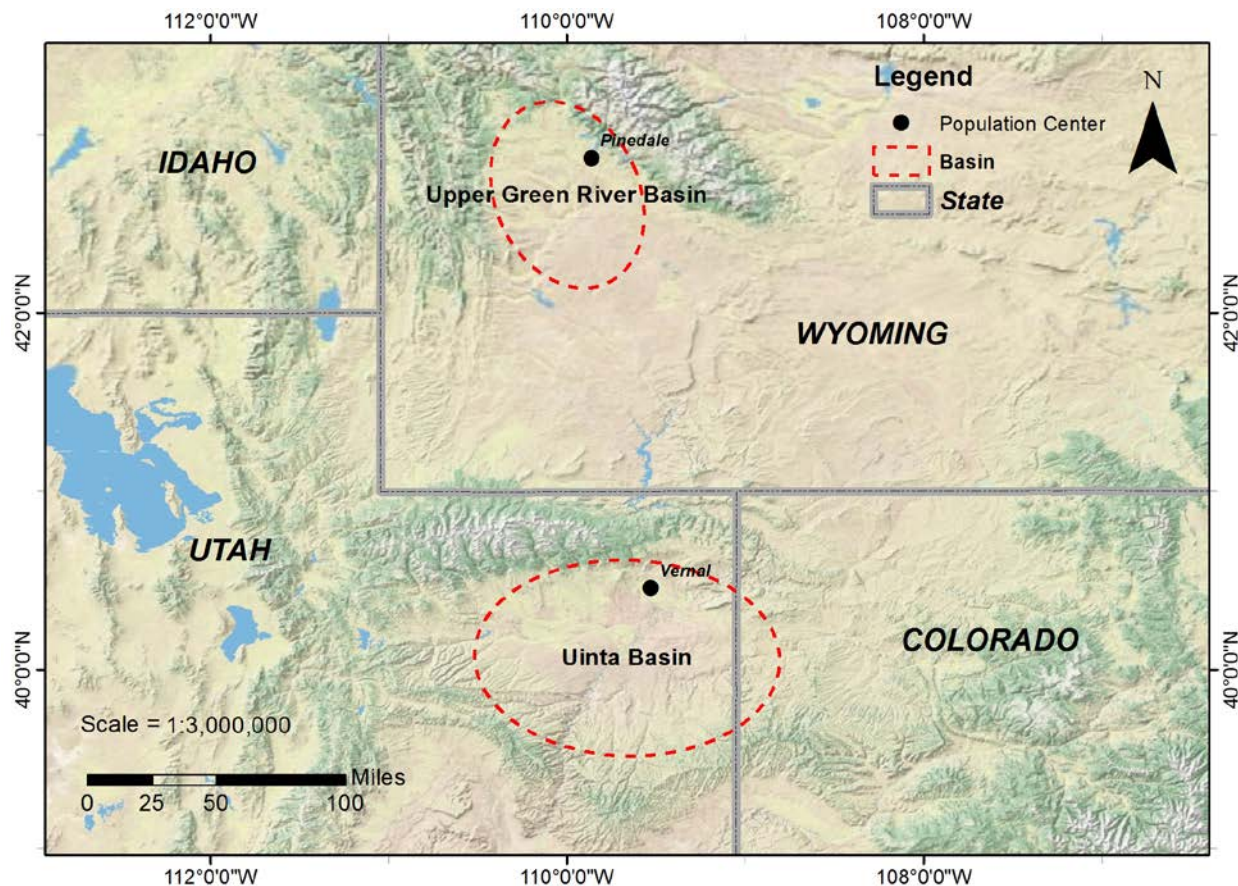
Figure 1-1. Geographic location of the Uinta Basin relative to Wyoming's Upper Green River Basin.

1.2 RELATED STUDIES

Very high wintertime ozone concentrations with patterns similar to those experienced in the Uinta Basin in 2009-10 have been recorded in the rural Upper Green River Basin (UGRB) of Wyoming since 2005. The UGRB is in rural Sublette County (2010 population: 10,247; population density: 0.8 people per km^2) in western Wyoming and covers roughly 5600 km^2 (Census Bureau, 2011). Since 2005, annual wintertime air quality studies have been conducted in the UGRB to understand the causes of elevated ozone concentrations and the most effective remediation strategy for the area. These studies (i.e., Schnell et al., 2009) have shown that severe, low level temperature inversions during periods of stagnant winds, a shallow mixing layer (≤100 m), clear skies under synoptic high pressure systems, combined with snow cover and abundant VOCs and NO$_x$ result in, "rapid photochemical production of ozone at high concentrations in a rural site during winter."

In contrast to the typical atmospheric condition in which ambient temperature *decreases* with increasing altitude, a temperature inversion refers to the condition in which ambient temperature *increases* with increasing altitude. These inversions engender ozone because they form stagnant pools of air that prevent dispersion and vertical mixing of ozone precursors. Schnell et al. (2009) point out that strong temperature inversions can last several days in the UGRB, during which time all precursor emissions originating near the surface are trapped in the shallow mixing layer.

The low surface wind conditions allow precursor concentrations to build dramatically through decreased advection and dispersion.

Snow cover is also important in the UGRB for two reasons. First, snow has a noontime surface albedo (~90%) that is much higher than most other surface types and can nearly double the amount of solar energy available to drive photochemical reactions through reflection. Second, snow cover reinforces the temperature inversion by preventing the heating of the ground and the air immediately above the ground. The high elevation of the UGRB (~2,300 m at the lowest point) is also significant in that the total attenuation path length through the atmosphere is reduced, resulting in greater incoming solar radiation than at lower elevations, all other factors being equal. Schnell et al. (2009) note that surface level wintertime ozone production may be occurring in other areas of the U.S. and the world with similar fossil fuel production, terrain, and meteorological conditions. Measurements in such locations, however, were lacking at the time of their report.

One-hour average ozone levels above 140 ppb were recorded in February 2008 in the UGRB, and the EPA's 8-hr average standard was exceeded 14 times during the corresponding winter months. It should be noted that the only significant industrial sources of ozone precursors in the UGRB are associated with the production of natural gas in the 400 km^2 Jonah-Pinedale Anticline gas fields, which have seen a large increase in extraction activities over the past decade. Changes to the equipment used for drilling and production were made in an attempt to reduce these emissions and avoid nonattainment status. However, in March 2009, the state of Wyoming submitted a letter and supporting technical documents to the EPA recommending that Sublette County in the UGRB be designated a nonattainment area for ozone due to persistently high values over multiple years (http://deq.state.wy.us). EPA's designation of Sublette County, WY, as a nonattainment are has been delayed until after the release of the new ozone NAAQS currently under review.

The Uinta Basin has meteorological conditions and oil and gas exploration and production processes similar to those attributed to high winter ozone levels in the UGRB of Wyoming. These parallels suggest that the high winter ozone levels in the Uinta Basin result from factors similar to those observed in Wyoming. Despite these similarities, however, each region has unique air quality characteristics and patterns that must be considered to achieve a thorough and accurate environmental study.

Such seemingly atypical wintertime, photochemically-driven secondary pollutant issues have also been observed in other areas around the region. Similar meteorological conditions (very low, persistent temperature inversions with clear skies) in Utah's Cache Valley and Wasatch Front have been shown by USU and UDAQ to lead to high wintertime PM$_{2.5}$ problems with slight increases in surface level ozone. During such episodes, fine particles are formed as another product of photochemical reactions that include additional precursor gas-phase species such as ammonia which is in relative abundance locally. Although similar meteorological conditions prevail in these areas, the ultimate pollutant problem (PM$_{2.5}$) is reflective of the differing precursor species.

1.3   PROGRAM OBJECTIVES

The Uinta Basin Winter Ozone and Air Quality Study reported herein consisted of two integrated components. First, a study was performed to provide a preliminary assessment of general ozone

concentrations in the Uinta Basin during a three-month period starting in late December 2010 and concluding in March 2011. Second, a more intensive study was performed over a five-day period during a winter inversion. Data collected and analyzed during this time included ozone, VOCs, NO_x, $PM_{2.5}$, and relevant meteorological parameters at two selected locations. The general intent was that these data be used by the larger community to help identify possible causes of ozone formation, possible sources of NO_x and VOCs accumulation, and variables key to future monitoring studies and photochemical airshed models.

The monitoring program outlined above had the following specific objectives:

1. To provide baseline data of ozone concentrations throughout the Uinta Basin during the 2010-2011 winter months,
2. To provide information on the ambient concentrations of VOCs, NO_x, $PM_{2.5}$ and relevant meteorological parameters during a winter inversion event,
3. To contribute to the long-term understanding of the relationship between winter inversion events and VOCs, NO_x, $PM_{2.5}$ and relevant meteorological parameters,
4. To provide sufficient information to enable some preliminary photochemical modeling activities,
5. To provide insights regarding possible anthropogenic factors involved in winter ozone formation and possible mitigation steps to reduce winter ozone levels, and
6. To guide the design of a more comprehensive, long-term airshed monitoring, analysis, and modeling program of the Uinta Basin. The intent of the more comprehensive, multi-year, air quality study would be to understand the physical and chemical processes significant to ozone formation and to determine and implement mitigation steps to reduce winter ozone levels in the Basin.

As a particular note, this effort was only the first step toward identifying mechanisms of ozone or ozone precursor generation in the Basin. Measuring, understanding, and modeling air quality impacts that originate from numerous sources, including oil and gas development, pose a significant challenge. It will take multiple efforts spanning several years to fully understand the winter ozone problem in the Uinta Basin.

In addition, pollutant concentrations measured during this study shall not be used to determine the attainment status of the counties of the Uinta Basin. The motive of this effort, rather, grew from a central goal shared by many federal, state and local organizations including the Uintah Impact Mitigation Special Service District (UIMSSD), the Utah Bureau of Land Management (BLM), the Utah Department of Environmental Quality (UDEQ) and its Division of Air Quality (UDAQ), Utah State University (USU), industry, and others ultimately to understand the spatial extent and physical and chemical processes leading to wintertime ozone production in the Basin. This information will assist in developing a meteorological and photochemical airshed model capable of addressing the environmental and economic needs of the Basin. One of the first steps in developing this comprehensive model was to determine "baseline" ozone levels in the Uinta Basin, a significant milestone accomplished by this study. The air quality and meteorological data obtained during this study will guide future measurement efforts and the construction of an environmental model that will lead to a better understanding of the factors contributing to ozone formation in the Basin.

2. MONITORING PROGRAM

As previously mentioned, the monitoring program consisted of two integrated elements: (1) a three-month, Basin-wide winter ozone monitoring program and (2) a more intensive, short-term monitoring program that simultaneously measured ozone, VOCs, NO_x, $PM_{2.5}$, and vertical profiles of relevant meteorological parameters during a strong winter inversion event. These two program elements are described in separate sections below.

2.1 BASIN-WIDE WINTER OZONE MONITORING

Ozone concentrations were measured at 18 locations in the Uinta Basin (Fig. 2-1 and Table 2-1) over the course of this study. None of the 18 monitors was established for regulatory purposes and, therefore, cannot be used in official consideration for NAAQS compliance.

2.1.1 Established Monitoring Stations

The USU/EDL team sought access to data from eight previously established Uinta Basin area ozone-monitoring stations that would be in operation during the planned study period (responsible agency in parentheses):

- Dinosaur National Monument (National Park Service - NPS)
- Fruitland (UDAQ for BLM Utah)
- Myton (Meteorological Solutions, Inc. for Ute Tribe)
- Nine Mile Canyon (BLM Utah)
- Ouray (Golder Associates, under EPA consent agreement)
- Rangely, CO. (NPS for BLM Colorado)
- Red Wash (Golder Associates, under EPA consent agreement)
- Whiterocks (Meteorological Solutions, Inc. for Ute Tribe)

Golder Associates provided access to the data from the Ouray and Red Wash monitoring stations, and BLM Utah permitted access to the data from the Fruitland station. BLM Utah and NPS agreed to provide access to the data from the Nine Mile Canyon and Dinosaur National Monument sites, respectively; and NPS and BLM Colorado granted access to the data from the station at Rangely, CO. Data from the Whiterocks and Myton monitoring stations were not available when this report was finalized.

2.1.2 New Monitoring Stations

The USU/EDL team deployed ten additional ozone monitors throughout the Basin to enhance the existing ozone monitoring network for the purposes of this study. The ten monitors were in place only during the study period of this project and were strategically located to provide adequate spatial coverage and to account for variations in topography and meteorology and to avoid biasing the monitor results by proximity to potential ozone precursor sources. The monitor locations were developed through consultation among the USU/EDL sampling team, UDAQ, BLM, county government, industry, local contacts, and others. Monitor placement provided a diverse sampling of environments: population centers, oil/gas fields, farms/ranches, open ranges, wetlands, etc.

2B Technology Model 205 Dual-Beam ozone monitors were used. For reliable operation, the Model 205 required 120 V AC power and a temperature-consistent enclosure for proper operation; these requirements were among the considerations in the selection of monitor

---

locations. The 2B Technology Model 205 ozone monitor has a dynamic range of 1.5 ppb to 250 ppm with an accuracy of 2% of the reading, and baseline drift of less than 2 ppb/day and less than 5 ppb/year. Ozone concentrations were logged as 5 min averages and subsequently compiled into 1-hr and 8-hr averages. Such fine time resolution could be essential to future high fidelity airshed regional modeling efforts.

2.1.3   Ozone Monitor Placement

In an effort to determine optimal placement of the ten ozone monitors installed for this study, discussions were held with several stakeholders. Placement decisions were guided by the stipulations that candidate sites:

- Fulfill guidelines given in 40 CFR 58 Appendix E, "Probe and Monitoring Path Siting for Ambient Air Quality Monitoring," including the avoidance of proximity to potentially interfering air pollutant sources;
- Represent adequate spatial distribution throughout the Uinta Basin, including the consideration of existing monitoring stations operated by other organizations that allow data access; and
- Provide winter access to allow adequate monitor servicing.

Once general monitoring areas were determined, Uintah and Duchesne County commissioners, local and state officials, local residents, and local businesses and industries proved very helpful in determining precise locations for the monitoring stations.

During the week of December 26, 2010, the USU/EDL team and a representative from the Utah Division of Air Quality (UDAQ) placed ozone monitors at seven locations:

- Altamont (city ambulance garage)
- Cedarview (private residence)
- Duchesne (city fire station)
- Lapoint (city fire station)
- Roosevelt (USU campus utility shed)
- Vernal (USU Highway 40 building)
- Horse Pool (QEP pump house, Wonsits Valley)

On January 11-13, 2011, the remaining three sites were determined, and monitors were installed in the following locations:

- Jensen (commercial nursery shed)
- Rabbit Mountain (private meteorological/air quality station)
- Pariette Draw (BLM field building)

The average above ground height of the installed probes was 6.9 m (min. 3.0 m/max. 15.0 m), with an average above-roof height of 1.2 m (min. 1.0 m/max. 2.0 m). Geospatial coordinates for each site were collected on multiple site visits using a handheld GPS unit and are given in Table 2-1. It should be mentioned that where the flexibility existed, the above sampling locations were selected using the previously listed site selection criteria.

Table 2-1. Uinta Basin ozone monitoring site location and above sea level elevations (per GoogleEarth™).

Location	Responsible Organization	Longitude (°W)	Latitude (°N)	Elevation (m)
Altamont	USU & EDL	110° 17' 8.609"	40° 21' 36.785"	1947
Cedarview	USU & EDL	110° 4' 34.189"	40° 22' 7.862"	1692
Dinosaur NM	NPS/ARS	109° 18' 16.785"	40° 26' 13.439"	1463
Duchesne	USU & EDL	110° 24' 3.895"	40° 9' 41.260"	1681
Fruitland	UDAQ/AMC	110° 50' 25.179"	40° 12' 31.433"	2021
Horse Pool	USU & EDL	109° 28' 1.849"	40° 8' 37.339"	1567
Jensen	USU & EDL	109° 21' 7.993"	40° 22' 1.595"	1451
Lapoint	USU & EDL	109° 48' 56.700"	40° 24' 14.717"	1672
Myton	Ute Tribe	110° 3' 43.82"	40° 11' 41.25"	1550
Nine Mile Canyon	BLM	110° 12' 12.67"	39° 47' 30.70"	1732
Ouray	Golder Assoc.	109° 40' 37.68"	40° 5' 18.39"	1419
Pariette Draw	USU & AMC	109° 49' 48.2"	40° 2' 4.57"	1424
Rabbit Mountain	USU & EDL	109° 5' 50.361"	39° 52' 7.318"	1879
Rangely, CO	NPS/BLM	108° 45' 41.8"	40° 5' 12.8"	1648
Red Wash	Golder Assoc.	109° 21' 9.00"	40° 11' 49.79"	1689
Roosevelt	USU & EDL	109° 58' 42.302"	40° 18' 2.630"	1543
Vernal	USU & EDL	109° 33' 39.67"	40° 26' 35.73"	1661
Whiterocks	Ute Tribe	109° 55' 49.59"	40° 28' 9.80"	1841
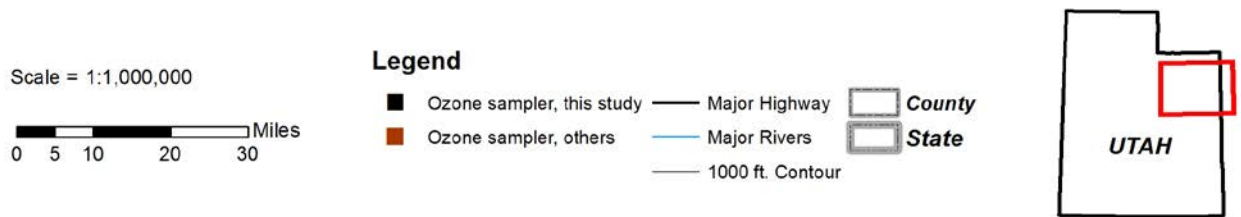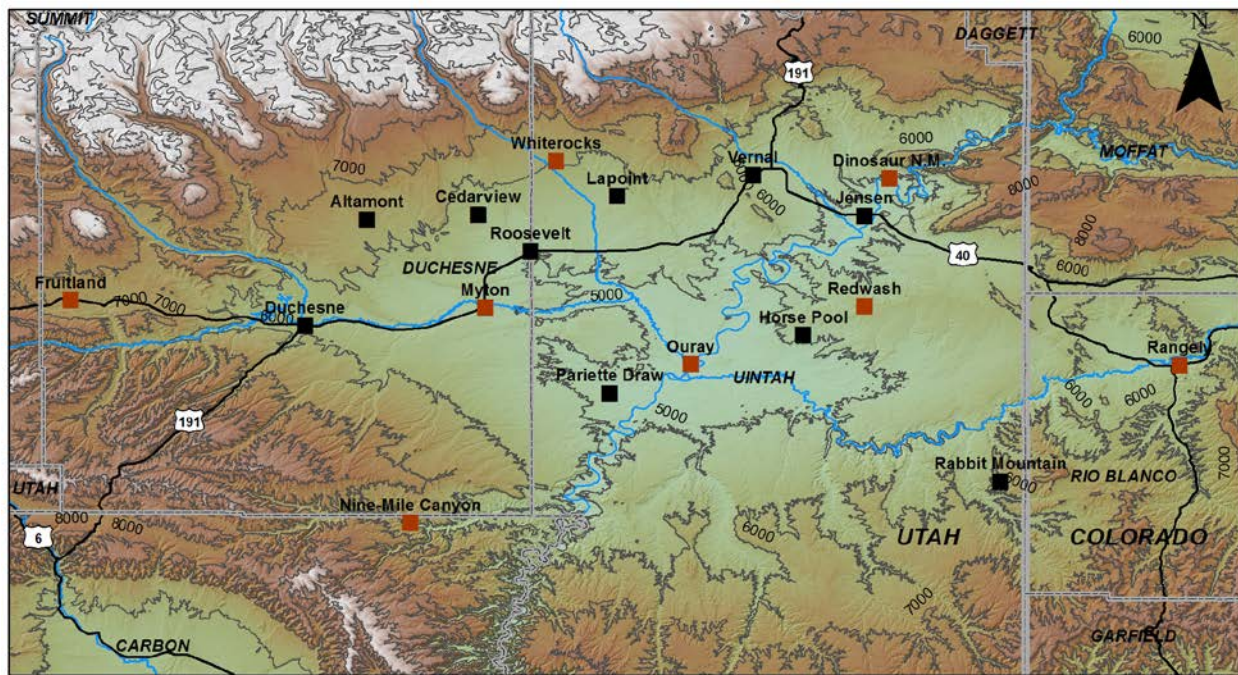
Figure 2-1. Locations of ozone monitors operated in the Uinta Basin during the winter of 2010–11.

It is of interest to examine the site locations in terms of relative proximity to potential ozone precursor (hydrocarbons, oxides of nitrogen) sources. Fig. 2-2 shows the same information as Fig 2-1, with the added complexity of known locations of permitted precursor point sources and active oil/gas wells.
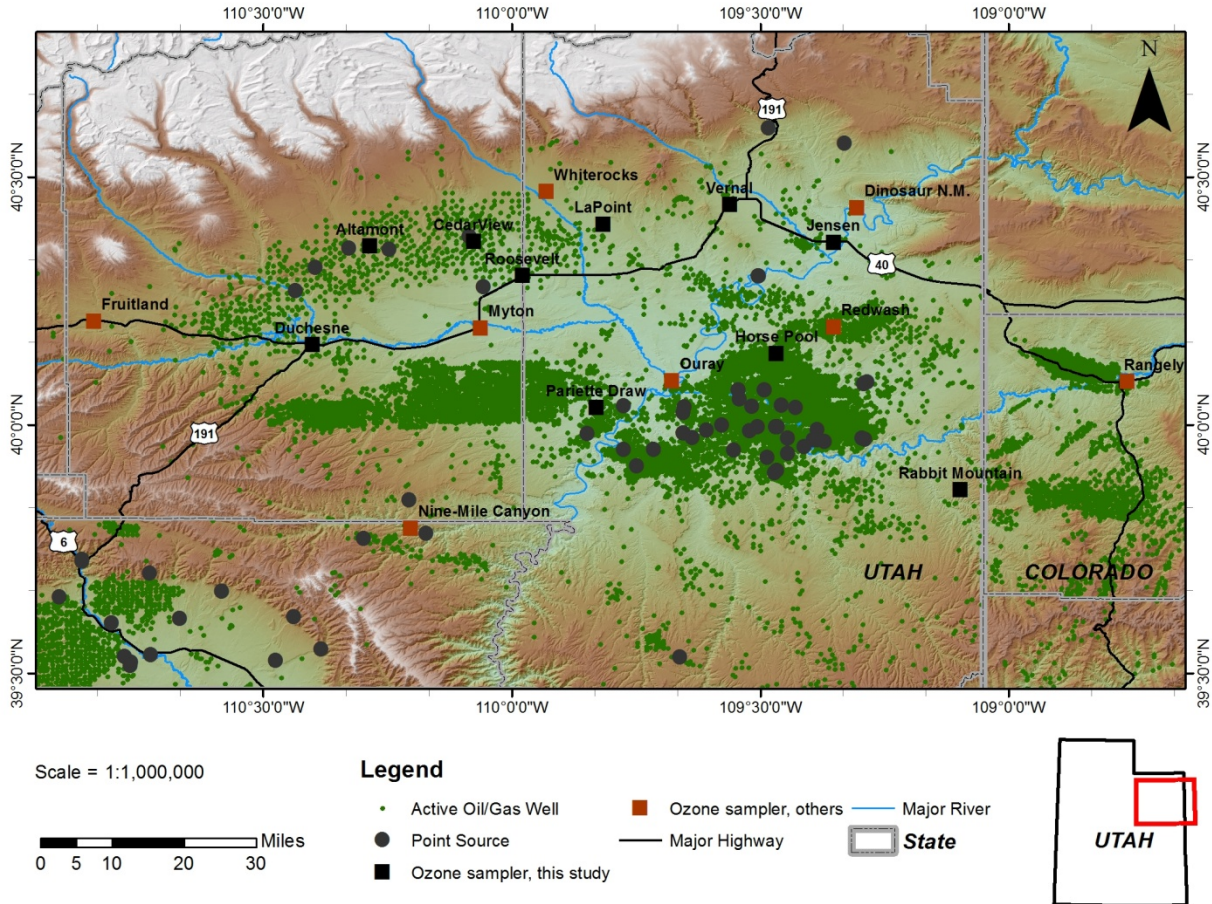
Figure 2-2. Winter 2011 Uinta Basin ozone sampling locations with an overlay of known ozone precursor point sources and active oil/gas wells.

2.1.4   Data Acquisition Procedures

Every two weeks, the study's ten ozone monitors were serviced, data were collected, and units were recalibrated (if necessary, as determined by audit procedures). These procedures were performed according to specific QA/QC protocols. The ozone monitoring was performed continuously for the entire winter season, with the exceptions of planned down time for periodic servicing and calibration checks.

2.2   INTENSIVE, SHORT-TERM OZONE, PM$_{2.5}$, NO$_X$, AND VOCS MONITORING

The long-term, Basin-wide ozone measurement was supplemented with a short, high-intensity effort focused on the collection of PM$_{2.5}$, NO$_x$, and VOCs concentrations during a strong winter inversion event. This intensive monitoring portion of the Winter Ozone Project was conducted from February 21 through February 25, 2011 at the Red Wash and the Vernal/Jensen sites. In addition to the ongoing measurement of ground-level ozone, ambient samples of NO$_x$ (FRM chemiluminescence monitor), PM$_{2.5}$ (five parallel, filter-based samplers), non-methane hydrocarbons/VOCs (staged activated carbon sorption tubes), and vertical meteorology (tethered balloon with a sonde package) were collected.

Throughout the test period, vertical meteorological parameters, including temperature, pressure, wind speed, and wind direction were collected via tethered balloons. These measurements were collected multiple times during daylight hours at both the Red Wash and Jensen locations. It should be noted that Federal Aviation Administration regulations prohibited vertical balloon operations in the Vernal area. The Jensen site, located at the commercial nursery, served as a reasonable substitute for the Ashley Valley vertical meteorology.

The maximum above ground elevations (agl) monitored were from approximately 800 - 1200 feet agl (244 - 366 m), depending on location and meteorological conditions. A separate 2B Technologies ozone monitor, purchased and modified for balloon and UAV flight as part of another project, was deployed at the Red Wash location for a single day of data collection. On February 24, 2011, multiple vertical ozone profiles were collected throughout the day, when ground level ozone at the collocated Red Wash location measured over 80 ppb.

Additionally, though not part of the proposed study, collocated methane samples were collected at the Red Wash and Vernal sites. Methane was measured at each field location by whole vial collection and later analyzed at USU's Utah Water Research Laboratory (UWRL) in Logan, UT, via gas chromatography. Owing to its slow reactivity, methane (CH$_4$) is generally not considered a significant contributor to tropospheric photochemistry; however, when present in high enough concentrations, methane has been shown to be a significant factor in ozone formation (e.g., Pinedale, WY).

3. METHODOLOGIES: INSTRUMENTATION AND ANALYTICAL PROTOCOLS

3.1 GROUND LEVEL OZONE

The instruments deployed during this study were Model 205 Dual-Beam Ozone Monitors from 2B Technologies (Boulder, CO). These instruments were approved by the EPA in 2010 as an ambient ozone monitoring Federal Equivalent Method (FEM; EPA, 2010b) and are routinely used by the NPS, UDAQ, BLM, and other research groups in ambient ozone monitoring. Five minute-averaged data were recorded and averaged up to 1-hr and 8-hr intervals in post processing. The monitors were located within structures or buildings, with a ¼-inch Teflon sample tube, between 5 m and 10 m long, running to the roof. Sample heights were nominally one meter above the roof level and three to five m above the ground level, with the exception of the Vernal site, which was 2 m above the roof and 15 m above the ground level. Fig. 3-1 shows an example of sample line and ozone monitor deployment.

Figure 3-1. Installation of the sample line and 2B Ozone Monitor at the Roosevelt location.

A concern at some sites during this study was maintaining the temperature of the instruments within the manufacture-stated operating range of 0 to 50 °C while ambient temperatures dropped to less than -30 °C. Effective site-specific solutions were developed in each case. Temperature was also recorded at each site with HOBO temperature dataloggers (Onset Computer Corporation, Pocasset, MA) set to 5-min averaging periods.

Instrument locations were visited every two weeks to download data, perform a precision, zero and span (PZS) check, and, if necessary, recalibrate the ozone monitor. PZS checks were performed at 0, 90, and 200 ppb ozone levels during January, then changed to 0, 90, and 140 during February and March. The change was initiated in order to bring the highest PZS and calibration check level more in line with expected maximum ozone concentrations. Following manufacturer's recommendations, an instrument did not pass the PZS check if it reported a mean deviation ($n = 10$) of more than 7% at any level greater than zero or a mean absolute value greater than 5 ppb at the zero check. Calibrations were performed at five points linearly spaced between 0 and 200 for January, and 0 and 140 for February and March. The ozone calibration sources were Model 306 Ozone Calibration Source systems from 2B Technologies, which were calibrated against the UDAQ in-house standard ozone calibration instrument. These PZS check and calibration procedures are used by the UDAQ for their portable monitors and are modeled after manufacturer recommendations (2B Technology, 2010).

Monitor servicing and calibration at sites operated by external organizations were not under the direction of the USU/EDL team and were assumed to meet similar standards of quality control. In addition to ozone, meteorological parameters were recorded at most sites operated by external organizations. The Dinosaur National Monument, Fruitland, Ouray, Red Wash, and Rangely locations recorded hourly averaged wind speed, wind direction, temperature, relative humidity, and pressure. The Ouray and Red Wash sites also measured incoming solar radiation, vertical wind speed, and aspirated temperature at two heights (2 m and 10 m). The vertically spaced temperature measurements typically are used to examine vertical temperature profiles and estimate atmospheric stability.

3.2 DATA MAPPING ANALYSIS

Geospatial analyses and map production were performed using ArcMAP 10 (ESRI, Redlands, CA). Geographic Information System (GIS) data utilized in these operations were downloaded from the following sources: Utah GIS Portal, BLM Colorado, BLM Wyoming, Colorado Department of Transportation, Colorado Oil and Gas Conservation Commission, Colorado's Decision Support System, Idaho Department of Water Resources, and U.S. Geologic Survey National Elevation Dataset. The GIS data sources are shown below.

3.3 GIS DATA SOURCES

BLM Colorado. Available: http://www.blm.gov/co/st/en/BLM_Programs/geographical_sciences/gis.html. Last accessed: April 28, 2011.

BLM Wyoming. Available: http://www.blm.gov/wy/st/en/resources/public_room/gis/datagis.html. Last accessed: April 27, 2011.

Colorado Department of Transportation. Available: http://www.coloradodot.info/. Last accessed: April 27, 2011.

Colorado Oil and Gas Conservation Commission. Available: http://cogcc.state.co.us/. Accessed: March 24, 2011.

Colorado's Decision Support System. Available: http://cdss.state.co.us/DNN/default.aspx. Accessed: March 24, 2011.

Idaho Department of Water Resources. Available: http://www.idwr.idaho.gov/GeographicInfo/ GISdata/gis_data.htm. Accessed: April 28, 2011.

U.S. Geologic Survey National Elevation Dataset. Available: http://ned.usgs.gov. Accessed: March 22, 2011. Last modified: August 2006.

Utah GIS Portal. 2011. Available: http://agrc.its.state.ut.us/. Last accessed: April 27, 2011. Last updated: April 9, 2011.

Ozone concentration distributions throughout the Basin were examined through interpolation of hourly averaged measured values for visualization. Interpolated surfaces from hourly averaged measurements were estimated using the Kriging interpolation tool in ArcMAP. The following default options were used in the interpolation: the ordinary Kriging method, a spherical semivariogram model, and a variable search radius to include 12 data points in the interpolation process. The quality of the fit of the interpolated surfaces to corresponding measured values was evaluated for a randomly selected 10% of analyzed hourly surfaces (n=17) and quantified using the root mean square error (RMSE). The calculated RMSEs ranged from 0.07 ppb to 16.4 ppb, with the values for the first, second, and third quartiles being 0.14 ppb, 1.2 ppb, and 5.8 ppb, respectively. Most RMSEs were within the error of the ozone instruments while high RMSEs (>7 ppb) were found for hours with low mean ozone concentrations (<60 ppb averaged across all sites). These results show the interpolated surfaces fit the data well, except during some hours with low spatially-averaged concentrations.

3.4 OXIDES OF NITROGEN (NO$_X$)

Ambient NO$_x$ was measured by the USU/EDL team at the Vernal location only, pulling a sample directly from a teed branch of the same tube used to collect the ozone sample. The data were collected from the start of the intensive period (February 21, 2011) through the overall end of the Uinta Basin study (March 11, 2011). The instrument used was a USU-owned Thermo Environmental Model 42 Chemiluminescence NO$_x$ analyzer, which uses a molybdenum converter of NO$_2$ reduction. The instrument was calibrated prior to deployment using certified calibration gas-phase NO standard with dilution provided by commercially purchased zero air. As with the 2B ozone monitors, the NO$_x$ data collection was set for 5-minute averages and the data were post-processed into hourly averaged values. Additional ambient NO$_x$ data, collected using similar analytical techniques and protocols, were also obtained from Golder Associates for the Red Wash and Ouray locations.

3.5 HYDROCARBONS (VOLATILE ORGANIC COMPOUNDS – VOCS)

Two paired VOC tubes were collected nominally at 7:00 and 15:00 at each of the two main field sites, additional paired samples were also collected at other periods throughout the daylight hours, as time allowed. Each of the paired tubes sampled approximately 1 liter (L) of ambient air. The flow rates through each of the tubes were determined at the start and end of each sample period with a calibrated mass flow meter (Red Wash) or rotameter (Vernal). The purpose of the paired tube collections was to allow dual GC/MS analysis at UWRL: one tube for light hydrocarbon (C2-C6) analysis and one tube for heavy hydrocarbon (C6-C10) analysis. Additionally, field blanks and laboratory-spiked transport samples were obtained.

A modified EPA TO-15 and TO-17 approach was selected to meet the VOC data requirement. In general, this modified method consisted of sample collection on Supelco Air Toxics 3-phase Sorbent Tubes, desorption of analytes onto a capillary gas chromatographic columns, followed by separation, identification and quantification of analytes based on retention time and presence of quantification ions. The following modifications were used:

1. TO-15 protocols suggest an internal standard be used for calibration and quantification; in this study, an external calibration curve was used.
2. BFB spectral check was not performed; however, the PFTBA spectrum was examined prior to analysis to ensure the m/z 69, 131, 219 and 505.2 ion ratios were normal.
3. TO-15 recommends the collection of pairs of samples at each point to compare results at a high and low flow rate to ensure sufficient sample collection. In this study, only one sample per carbon range (C2-C6 and C6-C12) per site, at the lower recommended flow rate, was collected.

The specific thermal desorption GC/MS system setup used for this project is described below. The generic TO-15 GC method assumes cryogenic capability for the GC oven. Since UWRL does not have that capability, it was necessary to run the method in two ways, each using a different column, to capture the desired C2-C12 analyte list. The methods are designated herein as the Light Hydrocarbon (LHC) and Heavy Hydrocarbon (HHC) methods. The fundamental difference in these methods was the analytical column used. The LHC method was used to quantitate analytes from ethane to benzene in volatility; while the HHC method captured analytes from n-hexane to n-dodecane. The specific GC configurations for the LHC and HHC analyses are described below.

3.6 THERMAL DESORPTION UNIT: PERKIN ELMER TURBOMATRIX ATD THERMAL DESORBER

- Sorbent Sample Tubes: Carbotrap 300, Supelco pn: 25085
- Secondary cryofocussing trap: Perkin Elmer Air Toxics Trap for Turbomatrix, PE pn: M0413628
- Dry gas purge time: 5 min
- Dry gas purge temperature: 25 C
- Tube desorb temperature: 300 C
- Primary desorb time: 20 min
- Secondary trap cryofocussing temperature: -40 C
- Secondary trap desorb temperature: 300 C
- Cryotrap ballistic heating rate: 40 C/s
- Injection mode:
  - o LHC method: split, 10:1
  - o HHC method: splitless

3.7 GC/MS SYSTEM CONFIGURATION: LHC METHOD

- Instrument: Agilent 6890 GC/5973 MS
- Column: Thermo Scientific TG-Bond Alumina Na2SO4 PLOT. 50m x 0.32 mm x 1 μm phase. Thermo pn: 26001-6050

- Carrier gas: helium, 12 psi constant head pressure.
- GC Oven parameters: 105°C for 5 min, ramp to 140°C @15°C/min, hold 6 min, ramp to 160°C @ 15°C/min, hold 5 minutes, ramp to 200°C at 20°C/min, hold 40 min.
- Mass Spectrometer: SIM mode, 2-6 ions per analyte, 80-100 ms dwell per ion.

The analysis of the lighter fraction of compounds on the Alumina PLOT column yielded baseline resolution of analytes in most cases. Using a split injection increased peak sharpness and aided in this separation. Because of the increased possibility of non-target analyte interference in SIM mode for hydrocarbons in the C6 to C12 range, the LHC method was run in Scan Mode to obtain definitive mass spectra. With the exception of using a splitless injection, the desorber parameters were the same.

3.8   GC/MS SYSTEM CONFIGURATION: HHC METHOD

- Instrument: Agilent 6890 GC/5973 MS
- Column: Restek Rxi-5ms, 60m x 0.25 mm x 1 μm phase. Restek pn: 13456
- Carrier gas: helium, 17 psi constant head pressure.
- GC Oven parameters: 40°C for 3 min, ramp to 260°C @8°C/min, hold 10 min
- Mass Spectrometer: Scan mode, scanning 35-260 amu, 3.25 scans/sec

All data processing was done on either Enhanced Chemstation G1701DA v. D.00.01.27 or MSD Chemstation version E.02.00.493.

A set of trip QC samples were prepared. These samples consisted of two 10 ppbv 0.5 L volume samples, two 100 ppbv 0.5 L samples, and two trip blanks. The 10 ppbv trip QC samples were prepared by adding 5 mL of a certified 1000 ppbv Ozone Precursor standard (Fisher part number 06-802-385) to 495 mL of air in a 1.0 L tedlar bag. This bag was then mixed, attached to a clean Carbopack sampling tube, and drawn through the tube at approximately 15 mL/minute until empty. The 100 ppbv samples were prepared similarly, with the exception that 50 mL of standard was added to 450 mL air.

The trip blanks, blank sample tubes and calibration standard tubes were prepared by conditioning the tubes at 300°C for 30 minutes, and then capping them hand-tight with brass Swagelok caps. Teflon ferrules were used in the caps.

The initial calibration curves for each analysis were prepared using standard concentrations of 2, 10, 20 and 55 ppbv per analyte. The samples were made up in 1 L total volumes, in tedlar bags, as described above. The lab temperature and time was recorded. The ambient pressure was later recovered from meteorological station data. Each calibration standard was then loaded on a blank carbopack tube using an SKC personal sampling pump with a flow restrictor, so that the measured loading rates varied from 15 to 18 mL/minute, nominally the same flow rate as the field samples. The flow rates were checked at the beginning and end of loading using an Alltech Digital Flow Check mass flow meter.

Despite its slow reactivity with most atmospheric oxidants and though it is not generally considered a significant contributor to tropospheric photochemistry, methane (CH_4) was collected at each field location by whole vial collection and analyzed at the UWRL via gas chromatography . When present in high enough concentrations, methane has been shown to be a significant player in ozone formation (e.g., Wyoming's Pinedale region). The CH_4 vials were

collected at the start and end of each sorption tube collection period and intermittently throughout the daily periods. Fig. 3-2 shows collection of a CH_4 vial at the roof top Vernal site. Furthermore, the ice chest in the lower left portion of fig. 3-2 houses the paired VOC sorption tubes.

Figure 3-2. Hand-held methane (CH_4) vial collection and paired VOC sorption tube collection (red ice chest) at the Vernal, Highway 40 sampling location.

3.9 PARTICULATE MATTER LESS THAN 2.5 μm (PM$_{2.5}$)

During the weeklong intensive study period at both the Vernal and Red Wash locations, five (5) collocated PM$_{2.5}$ samples were collected using AirMetrics MiniVol portable particulate samplers. The samplers nominally operated for 23 hours each, from 12:30 (pm) to 11:30 (am), leaving an hour to exchange filters between sample periods. The samplers operate at an average flow rate of 5 Lpm, provide particle fractionation via a specifically designed impactor/plate system, and collect the particulate matter on a 47 mm filter. Prior to the field test, each system's flow monitoring rotameter was calibrated using a certified transfer standard (orifice) and adjusted in the field to maintain the required flow rate at actual conditions. Fig. 3-3 shows the collocated PM$_{2.5}$ MiniVol on the roof of the former USU building, Vernal (Highway 40) location.
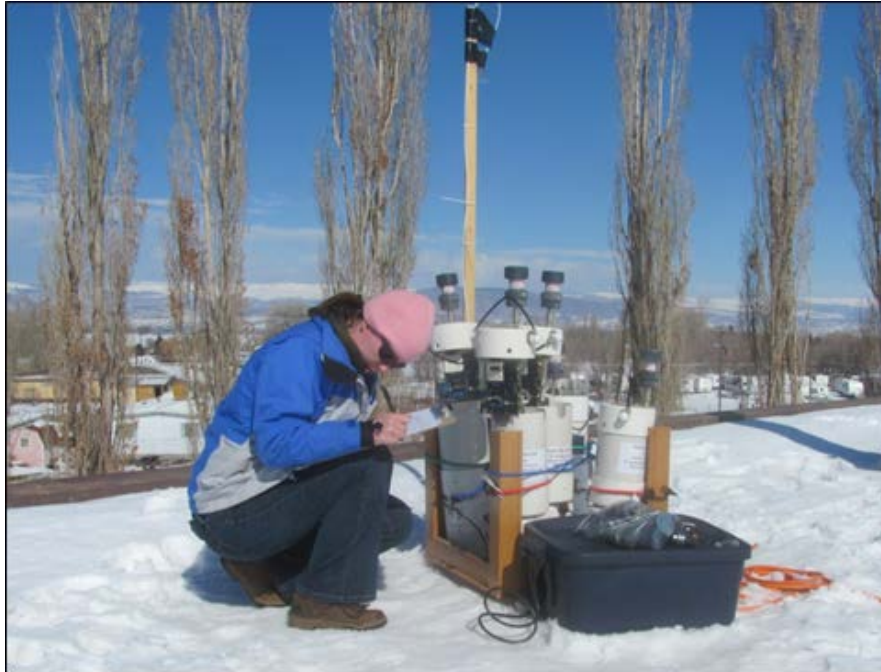
Figure 3-3. USU graduate student Wendy Merkley recovering flow data from the MiniVol PM$_{2.5}$ samplers at the Vernal, Highway 40 sampling location.

Through its Interagency Monitoring of Protected Visual Environments (IMPROVE) studies, the National Park Service has demonstrated that most fine particulate matter can be shown to be composed primarily of crustal (elemental) species, organic carbon, elemental carbon (black carbon or soot), ammonium sulfate, and ammonium nitrate (IMPROVE, 2011). Chemical speciation of the collected particulate matter is briefly described below.

Three MiniVol samplers were outfitted with pre-conditioned and pre-weighed 47 mm Teflon (TFE) membrane filters for gravimetric (total mass), ionic (soluble compounds), X-ray fluorescence (elemental composition) and Raman spectroscopic analysis (carbon and other chemical functional groups); one 47 mm pre-washed nylon filter as a duplicate method for examination of potential ionic particulate evaporation (especially nitrate); and one pre-conditioned 47 mm quartz filter for organic and elemental carbon analysis. The TFE filters were pre- and post-conditioned by storage at room temperature in a silica-gel desiccator for a minimum of 24 hours before weighing the filters on successive days until a consistency of ±2.5 µg was obtained on three consecutive weights. PM$_{2.5}$ concentrations were then determined by dividing the observed mass caught by the measured sample volume, with daily concentration at any particular site calculated as the average of the three TFE-filter based MiniVol samplers. Owing to post-test analytical requirements, no weights were determined for the collocated nylon and quartz filters; rather, it was assumed that their total captured mass would be similar to the mass captured with the TFE filter.

Ion chromatography (IC) analysis was used to quantify the soluble ionic species composition on the collected particulate matter. The analyses were performed at UWRL following standard protocols briefly described herein. All de-ionized water used in preparation, extraction, and IC analysis was purified using a Barnstead Nanopure Infinity water purification system and was

purified to 18.3 ΩM-cm resistance then filtered through a 0.2 μm-membrane filter. Prior to sample collection, nylon filters were rinsed three times in de-ionized water and allowed to air dry. For the extraction process, the collected Teflon and nylon filters were soaked in triplicate in 10 mL of de-ionized water, while being sonicated for 10 minutes. Following each individual extraction, the samples were combined for a total volume of 30 mL. Immediately following the final extraction, 15 mL were removed and spiked with 10 μl of 0.5 M HCl to fix the ammonium (NH_4^+), thus preventing it from evaporating as the gas-phase ammonia (NH_3) form. The remaining 15 mL was left untreated for anion analysis. Samples were stored in a refrigerator at ≤4°C until final IC analysis, which was within two to three weeks of original collection.

In order to remove any insoluble particulate matter, samples were filtered through a 0.2 μm nylon 13 mm Fisher syringe filter prior to being loaded on the IC for analysis. A Dionex ICS 3000 IC system (Dionex, Sunnyvale, CA) was used to determine cation and anion concentrations. The IC system consisted of a dual pump (DP1), eluent generator (EG2) and detector chromatography module (DC2). CSRS 300 4mm and ASRS 300 4mm suppressors were used as well as AS-11 HC and CS12A columns for the respective ionic species. A CRD 200 4mm carbonate removal device was used for the anion analysis. Anions were analyzed using 30 mM potassium hydroxide eluent produced in the eluent generator. Cations were analyzed using 0.3 N sulfuric acid eluent separately prepared in the laboratory, which was diluted to 10% by the IC pump, for a final concentration of 0.03 N sulfuric acid. A 283 μl sample loop was used for anions and cations. Chromeleon version 6.8 SR6 software was used to process the data.

Stock standards of 1000 mg/L were prepared using ACS reagent grade salts. Anion calibrations included fluoride, chloride, nitrate, nitrite, and sulfate with dilutions of 5, 2, 1, 0.5, 0.2 and 0.1 mg/L. A linear fit was used for chloride and nitrate calibrations, while a quadratic fit was used for the other anions. Cation calibrations included sodium, ammonium, potassium, magnesium and calcium with dilutions of 5, 2, 1, 0.5, 0.2 and 0.1 mg/L, except ammonium, magnesium and calcium which achieved a better fit with dilutions of 2, 1, 0.5, 0.2 and 0.1 mg/L. Ammonium, magnesium and calcium calibrations used a quadratic fit; while sodium and potassium used a linear fit. De-ionized water and quality control samples were checked prior to any analysis and rechecked approximately every ten samples. Field blanks of both filter types were collected and analyzed, as well as duplicate lab blanks, in both cases filters were treated as samples. Duplicate analyses were performed on no less than 10% of the samples.

One TFE filter from each run was analyzed for PM$_{2.5}$-bound elemental composition via X-ray fluorescence (XRF) as determined through a commercial laboratory (CHESTER LabNet, Tigard, OR) following EPA IO-3.3. Target elements included Na, Mg, Al, Si, P, S, Cl, K, Ca, Ti, V, Cr, Mn, Fe, Co, Ni, Cu, Zn, Ga, Ge, As, Se, Br, Rb, Sr, Y, Zr, Mo, Pd, Ag, Cd, In, Sn, Sb, Ba, La, Hg, and Pb. It should be noted here that most of the target elements were observed, but not at levels statistically above the reported limits of detection. Only the most significant elements will be included in subsequent discussions.

Organic carbon (OC) and elemental carbon (EC) PM$_{2.5}$ content were similarly determined through the use of a commercial laboratory (Sunset Laboratory, Tigard, OR). Pre-conditioned 47 mm quartz filters were obtained from the vendor and stored refrigerated until used in the field. After exposure, the filters, along with unused blank filters, were returned to Sunset Laboratory for carbon determination. The protocol is more fully described by Birch and Cary (1996), but briefly the filter is exposed to an oxygen-free, helium atmosphere and heated through a stepped series to approximately 700°C which vaporizes any organic carbon. The gas-phase carbon is

transferred to an oxidizer oven where it is converted to carbon dioxide, followed by methanization, and quantified via flame ionization detection (FID). To account for non-carbon components of the organic compounds' mass, the OC concentrations reported were increased by the recommended multiplier of 1.7 (Malm and Hand, 2007). The remaining filter sample is then further heated to 850°C, vaporizing the remaining elemental carbon and quantifying the EC concentrations following the same procedure as the OC concentrations.

3.10 GROUND LEVEL METEOROLOGY

Ground level meteorology data were not directly collected at any of the monitoring locations by the USU/EDL sampling team. Any presented meteorology data were collected by external parties already mentioned (NPS, BLM, Golder Associates, etc.) and other resources, as available (e.g., MesoWest).

3.11 VERTICAL METEOROLOGY

Vertical profiling of meteorological parameters was carried out during daylight hours at the Red Wash and Jensen sites from about noon on February 21, 2011 until sunset on February 24, 2011. Ideally, closer proximity to the Vernal site would have been preferred; however, Federal Aviation Administration (FAA) requirements prohibited operating a tethered balloon within five miles (8 km) from the local airport. The nearby Jensen location, therefore, was used as a spatially and geographically similar surrogate. Measurements at both sites were accomplished using a tethered balloon carrying a meteorological tethersonde or on-board data collection package. Fig. 3-4 shows the tethersondes as deployed at the Jensen and Red Wash sites, respectively**.**

Figure 3-4. Meteorological tethersonde operations at Jensen (left) and Red Wash (right).

The instruments employed at the Red Wash site were the SmartTether Flight Module and the SmartTether Ground Station, both from Anasphere, Inc. The Flight Module relayed

instantaneous measurements of temperature, relative humidity, pressure, wind speed, and wind direction every three seconds to the Ground Station, which was connected to a computer running SmartTether, Ver. 3.1.1 communications and datalogging software provided with the tethersonde system. The meteorological package was suspended about 3 m below the balloon on the string attaching the balloon to the electronic winch and was free to spin about the string.

Ascent and descent of the balloon were manually controlled, with a standard initial height above ground level (agl) of the package set at 2.0 m. Final heights of the package, determined by the lifting capacity of the balloon, were between 250 and 350 m agl. The descent was usually initiated within three minutes once the maximum height was reached to reduce the time between the start of the ascent and end of the descent. A total time for the ascent and descent of 20-30 minutes was targeted. Vertical profile meteorological characterization was performed throughout the day, with special focus on the following time periods: shortly after sunrise, around sunset, at midday, and at mid-afternoon. Calibrations of the electronic compass in the Flight Module to true north were performed on February 22, 23, and 24, 2011. In addition, calibration checks were performed with the differences between reported and actual direction recorded for correction in post-processing.

Measurements collected at the Jensen site were made on the same days as those at the Red Wash site and during daylight hours only. Data collection at Jensen varied from that at Red Wash, however, since vertical soundings were generally made once every hour, with the total time for a descent and ascent being less than 20 minutes. The maximum height above ground level (agl), as measured by a handheld commercial laser range finder, was 290 m and a standard minimum height of 2.0 m was maintained.

Winds at the various elevations were monitored at the Jensen site using a custom wind speed and wind direction measurement system developed at EDL. This custom unit measures wind speed using a #40C cup anemometer from NRG (accuracy ±0.1 m/s, threshold speed 0.78 m/s) and wind direction by 3-axis electronic compass from Honeywell. Unfortunately, the wind direction sensor was not operating correctly and did not produce usable data. Wind data were transmitted wirelessly to a receiver at the ground and logged by a computer. In addition, a small pressure, temperature, and relative humidity sensor, model PRHTemp 101, from MadgeTech (Contoocook, NH) was attached underneath the custom wind measurement system in a small opaque enclosure with several perforations to allow for passive air exchange to separately characterize vertical profiles for temperature, pressure, and relative humidity. The PRHTemp 101 logged three-second averaged data throughout the day, and the data were downloaded each night. Due to abnormally high readings on February 22 and 23, 2011 of nearly 20°C, well above the actual ground conditions (<5°C), a radiation shield made of aluminum foil was placed around the enclosure for the February 24, 2011 sample times.

The recorded temperatures for February 24, 2011 were much lower throughout the day than for the previous days. Significant lag times found between changes in pressure and temperature on each day, however, suggest that the enclosure was not adequately ventilated by the passive air exchange, particularly during ascents, and likely did not represent actual temperature and relative humidity conditions during vertical movement. As a result, the data for these two parameters collected by the PRHTemp 101 did not pass QA/QC and were not used in any subsequent analysis.

The elevation of the tethersonde packages were calculated based on their pressure measurements. Heights agl at the Red Wash site were calculated using the integrated hydrostatic equation that relates changes in pressure to changes in elevation, (Cooper and Alley, 2005). The modified equation is

$$z = z_0 - \frac{R_d T_v}{g} \ln\left(\frac{P_z}{P_0}\right)$$

(Eq. 3-1)

where z is the height of the tethersonde package in m, z_0 is the reference height (2.0 m), P_0 is the pressure in Pascals at z_0, P_z is the pressure measured at height z in Pa, g is the gravity constant of 9.81 m/s^2, R_d is the specific gas constant for dry air in J/kg-K, and T_v is virtual temperature in K. The virtual temperature of a moist parcel of air (i.e., with water vapor) is the temperature at which a theoretical parcel of dry air would have the same pressure and density as the moist parcel of air and is approximated using Eq. 3-2.

$$T_v \approx T_a(1 + 0.61q)$$

(Eq. 3-2)

where T_a is the ambient temperature in K, and q is specific humidity in dimensionless units of kg of water vapor per kg of moist air. Specific humidity is related to saturation specific humidity (q_s) and relative humidity (RH) through Eq. 3-3.

$$q = q_s\left(\frac{RH}{100}\right)$$

(Eq. 3-3)

Saturation specific humidity (q_s) is the maximum amount of water vapor that can exist at the current air temperature and occurs at $RH = 100\%$.

The elevations for the measurements at the Jensen site were not calculated in this manner due to the problems with the temperature measurements. The relative pressure differences recorded between the z_0 and maximum heights were assumed, nevertheless, to be valid due to the faster response time and the holes within the instrument housing which permitted pressure equilibration between the enclosure and the ambient air. Instead, the pressure differences were used in combination with recorded maximum heights measured by the laser range finder. Assuming that the pressure change over the <300 m distance was linear, a relationship between the maximum elevation and the lowest measured pressure for each vertical profile was calculated and used to estimate the measurement height.

The height of the first boundary layer above the ground, referred to as the depth of the surface layer, was estimated through examination of graphs of the vertical profiles of temperature, potential temperature, dewpoint temperature, wind speed, and wind direction. Potential temperature represents the theoretical temperature of a parcel of air after being brought to a standard pressure adiabatically (i.e., without transferring heat or energy to/from the surrounding air) and is calculated for each measured height z according to Eq. 3-4.

$$\theta_z = T_z \left(\frac{1000}{P_z} \right)^{0.286}$$

<div align="right">(Eq. 3-4)</div>

where T_z is the ambient temperature in K, P_z is the pressure in mb, the standard pressure is 1000 mb, and the units of θ are K. Calculating the potential temperature along a vertical profile allows comparison of air at all heights and is very useful in locating boundaries between different layers in the atmosphere. Dewpoint temperature is the temperature at which the air reaches water vapor saturation based on the amount of water vapor measured in the air. An example vertical profile from the Red Wash location is shown in Fig. 3-5 and shows actual ambient temperature, potential temperature, and dewpoint temperature in the same graph, with a dashed line marking the depth of the surface layer.
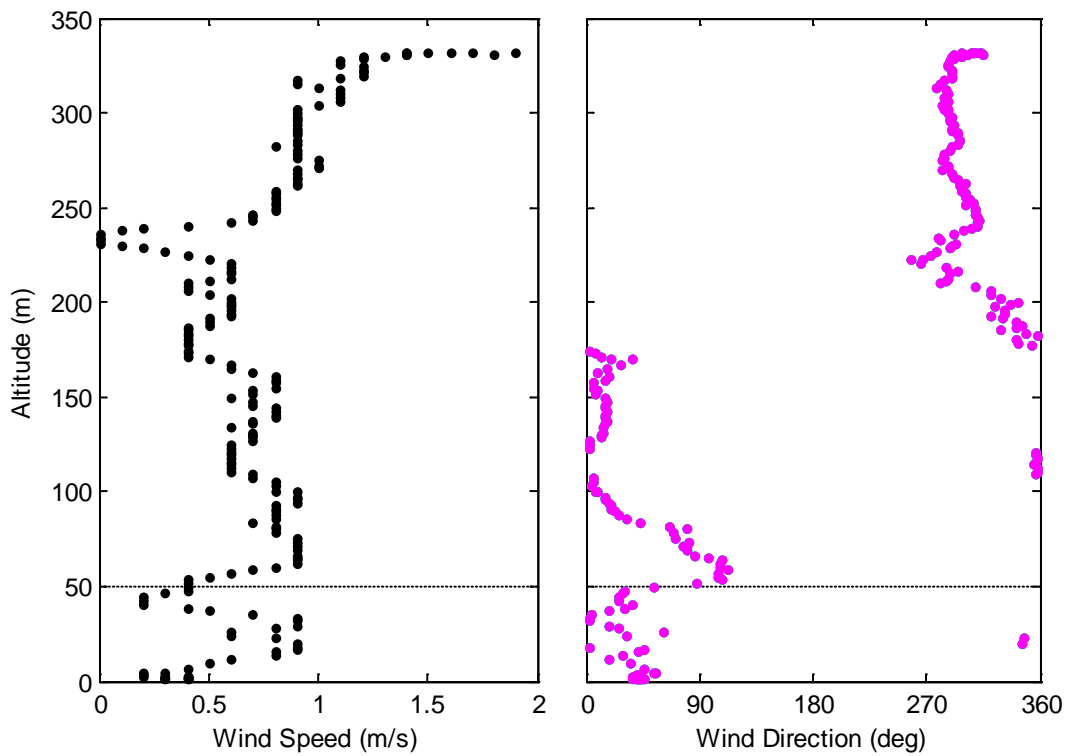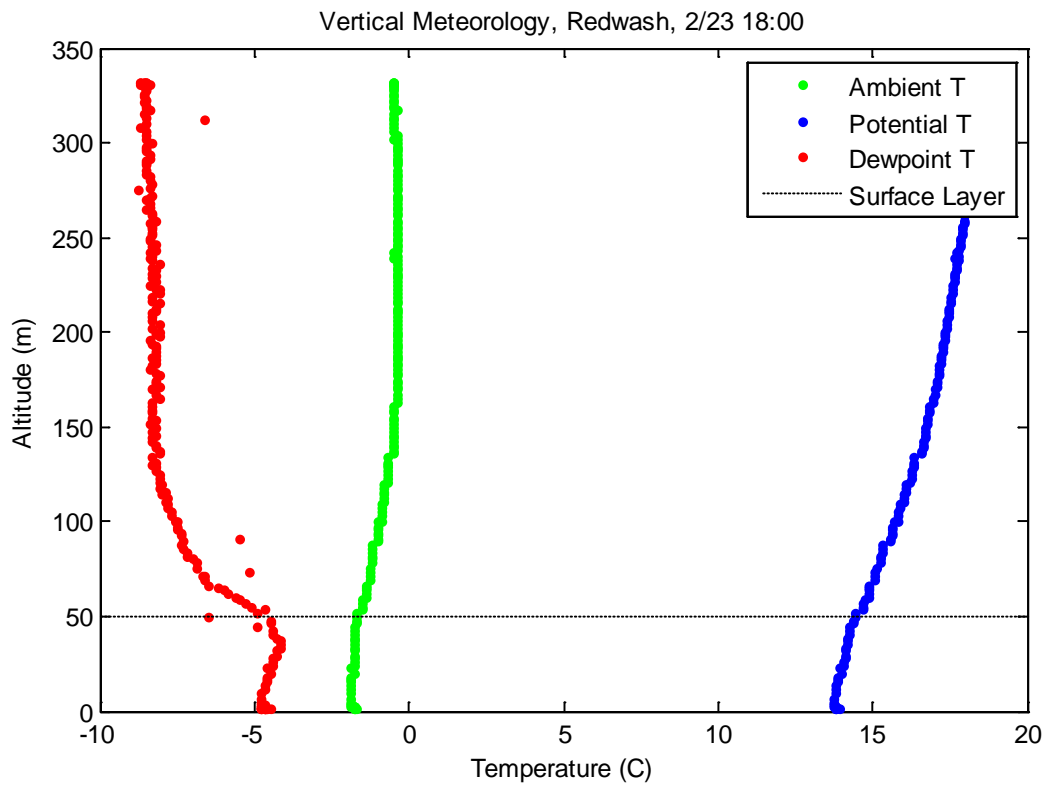
Figure 3-5. An example of vertical meteorology observed at the Red Wash site on Feb. 23, 2011, with a dashed line showing the approximate depth of the surface layer.

3.12 VERTICAL OZONE PROFILES

In order to measure vertical ozone profiles, a 2B Technologies Model 202 (single channel) Ozone Monitor was modified and used in conjunction with the previously discussed tethered balloon system. To use the 2B monitor for the purpose of collecting vertical ozone profiles, it was necessary to reduce the weight as much as possible. The monitor is originally built around a heavy aluminum plate and encased in an aluminum housing. To reduce weight, the housing was removed and the components of the monitor were remounted to a 6x9 inch copper/epoxy circuit board.

During balloon operation, a Thunder Power RC Li-Polymer 2100mAh 4S 14.8V 20C battery was used to supply power to the monitor. Due to the cold conditions of the winter time atmosphere, the battery was wrapped in a single layer of small bubble wrap and kept warm during flights by attaching a HotHandS HeatMax hand warmer to the outside of that bubble wrap. The entire unit was then encased in a single layer of small bubble wrap, followed by a double layer of large bubble wrap, a single layer of foam wrap and, finally, a layer of emergency blanket foil material. In order to protect the internal tubing and absorption cell from potential contamination due to particulate matter, a 2B technologies 2-mm PTFE particle filter in a PVDF 25-mm filter housing was attached to the inlet. External housing components were removed, and the Teflon tape was used to seal the housing. A 10-inch long, ¼-inch diameter sampling tube ran from the filter housing as the monitor inlet. All connectors and tubing were Teflon.

Prior to sampling, the monitor was allowed to warm up for thirty minutes on AC line power. After the initial warm up period, the monitor was quickly switched to battery power, the digital faceplate was removed, and the monitor was given a few minutes to equilibrate. Data averaging was set to 10-second intervals. The modified monitor and the in-field system can be seen in Fig. 3-6.

Figure 3-6. Modified 2B Technologies Model 202 ozone monitor remounted to circuit board and deployment at the Red Wash location.

Prior to field use, the ozone monitor was calibrated at the UWRL using a Thermo Environmental Instruments 49 C Ozone Calibrator. Ten data points were collected and averaged for a calibration curve of 0, 10, 20, 35, 40, 50, 70, 105, 120, and 140 ppb. The internal instrument offset (Z) and slope (S) were then adjusted as per manufacturer's protocol.

Vertical lift was achieved using an A.I.R, Inc. (Atmospheric Research Company) blimp-shaped, three cubic meter balloon, which was tethered to a TS-2AW A.I.R., Inc. electric winch. In order to assess mixing conditions, a HOBO temperature sensor was attached to the outside of the ozone monitor and sheltered from direct sunlight and set to collect data on three second intervals. During operation, the balloon was brought to the highest achievable point (determined using a range finder and estimated angle). That point was divided into nine segments, and the monitor was lowered to each target elevation, where it remained stationary for one and a half to two minutes. Time span, elevation and estimated elevation angle were recorded for each segment. Elevation for data points between stationary segments was then estimated using a linear relationship

4.   RESULTS AND DISCUSSION

4.1   BASIN-WIDE OZONE

The main goal of this initial study was to identify the spatial extent and severity of the wintertime ground level ozone concentrations in the Uinta Basin. The compiled, summarized data will be presented first, with individual site-specific ozone profiles presented in subsequent sections. The compiled, hourly averaged ozone concentrations for all of the available sites can be obtained as described in the Appendix. Currently, ambient ozone is regulated on a running eight hour (8-hr) average value. In other words, the consecutive 8-hr period throughout a midnight-to-midnight day with the highest average value is deemed to represent the regulatory value for that given day. As of this writing, the U.S. 8-hr NAAQS for ozone is set at 75 ppb. Furthermore, the U.S. Code of Federal Regulations specifies that yearly ozone exceedance will be based on the fourth highest 8-hr value rather than on the highest recorded 8-hr value. This designation allows for theoretically anomalously high concentrations to be discounted. Finally, an area's official regulatory or "design" value actually is determined as the average fourth highest 8-hr values from three (3) consecutive years. It should also be noted, that the U.S. EPA gave official notice in December 2010 that owing to continually evolving health-based evidence, the 75 ppb standard would be revisited by mid-July of 2011, and the ozone NAAQS is expected to be lowered to between 60 and 70 ppb. As a point of comparison, prior to a 1997 NAAQS revision, ozone was regulated in the U.S. as a 1-hr standard at a maximum allowable concentration level of 120 ppb.

Ground level ambient concentrations in the Uinta Basin throughout the wintertime 2010-2011 study period seemed to be functions of regional weather patterns (frontal passage vs. stagnant inversion), local site elevation and adjacent topography, and relative proximity to likely ozone precursor sources. As was also previously discussed in the "Ozone Photochemistry" section of this report, the snow-reflected, augmented available solar radiation (insolation) likely is a significant contributor to enhanced winter time ozone formation in the area. Since the entire region was snow covered during the study duration, however, it is not expected to be a contributor to site-to-site ozone differences and will not be discussed further in this regard.

Figures 4-1(a) and 4-1(b) show fitted (kriging interpolation) 1-hr ozone concentration contours for the test region for a "clean" period (15:00 MST, Feb. 10, 2011) and a "dirty" period (15:00, February, Feb. 16, 2011). As can be seen during the clean period, Fig. 4-1(a), the observed afternoon ozone concentrations were uniformly around 50 ppb throughout the Basin. This time period was characterized by unsettled weather following a storm system that came through the area approximately three days earlier. In contrast, after a lengthy, six-day inversion episode, it can be seen from Fig. 4-1(b) that the highest ozone levels formed in a region centered along the Ouray/Pariette Draw locations and extended north to the Cedarview/Lapoint area, east to the Red Wash area, and west to Duchesne. Furthermore, it can be seen that even during this high-ozone period, upper elevation and "fringe" locations such as Fruitland, Altamont, Nine Mile Canyon, Rabbit Mountain, and Rangely (CO) remained essentially at clean or background concentrations.
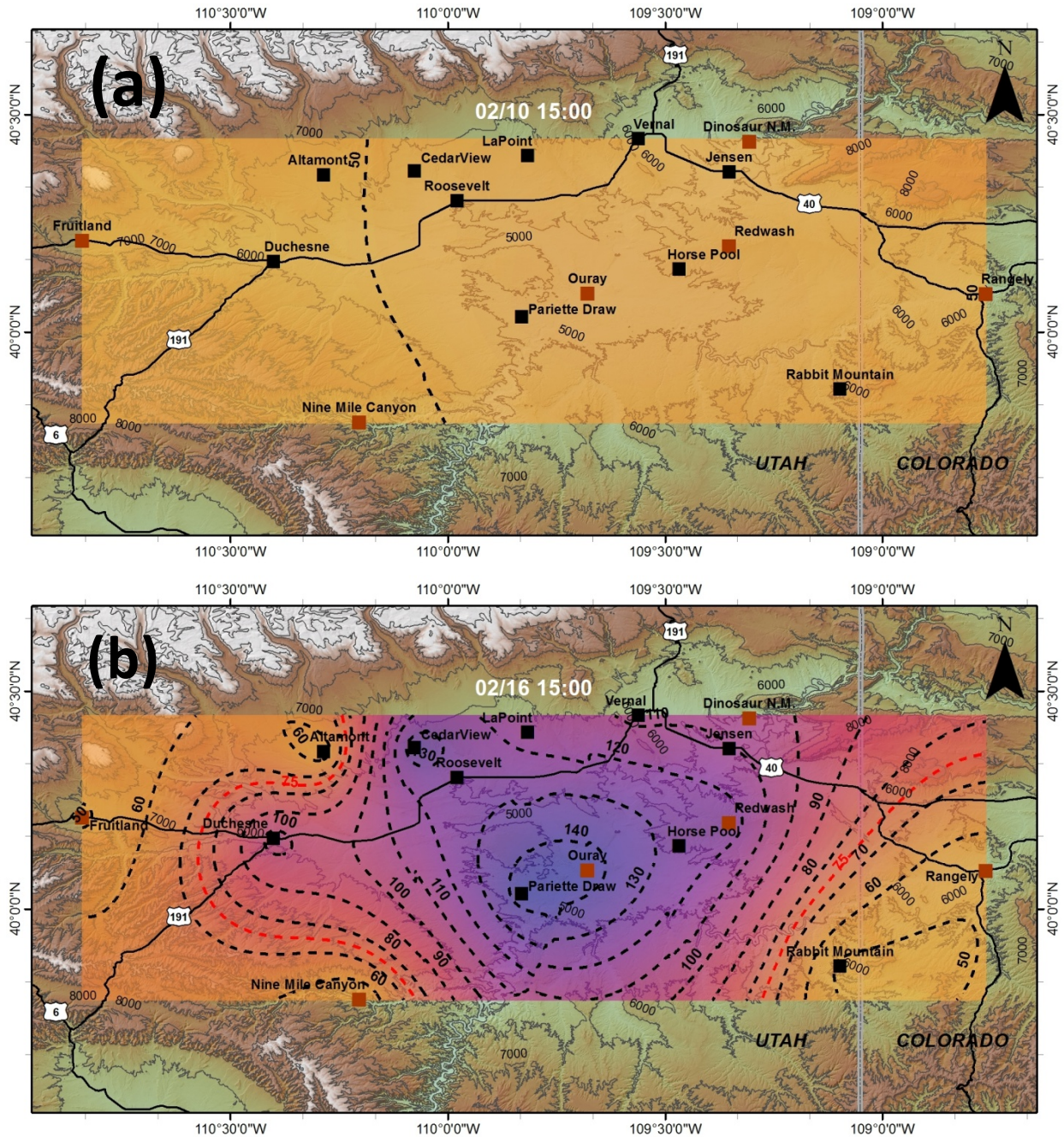
Figure 4-1. Uinta Basin 1-hr ozone concentrations during a clean period (a) 15:00 MST, Feb. 10, 2011 and a "dirty" period (b) 15:00 MST, Feb. 16, 2011. The dotted lines represent 10 ppb contour intervals.

The likely relationship between the abundance of precursor source emissions and the local ozone formation can be further inferred by examination of the ozone spatial concentrations and the suspected source locations. This is shown in Fig. 4-2 by combining the contour map shown in Fig. 4-1(b) and the active well map discussed in the "Ozone Monitor Placement" section.

Fig. 4-2 shows that the regions with the highest observed ozone concentrations tend to follow along the areas of greatest active well density. Furthermore, the fitted contour lines seem to

follow the well densities even in areas where in the sampler spacing was less than ideal (e.g., the area between Pariette Draw, Nine Mile Canyon, and Duchesne).
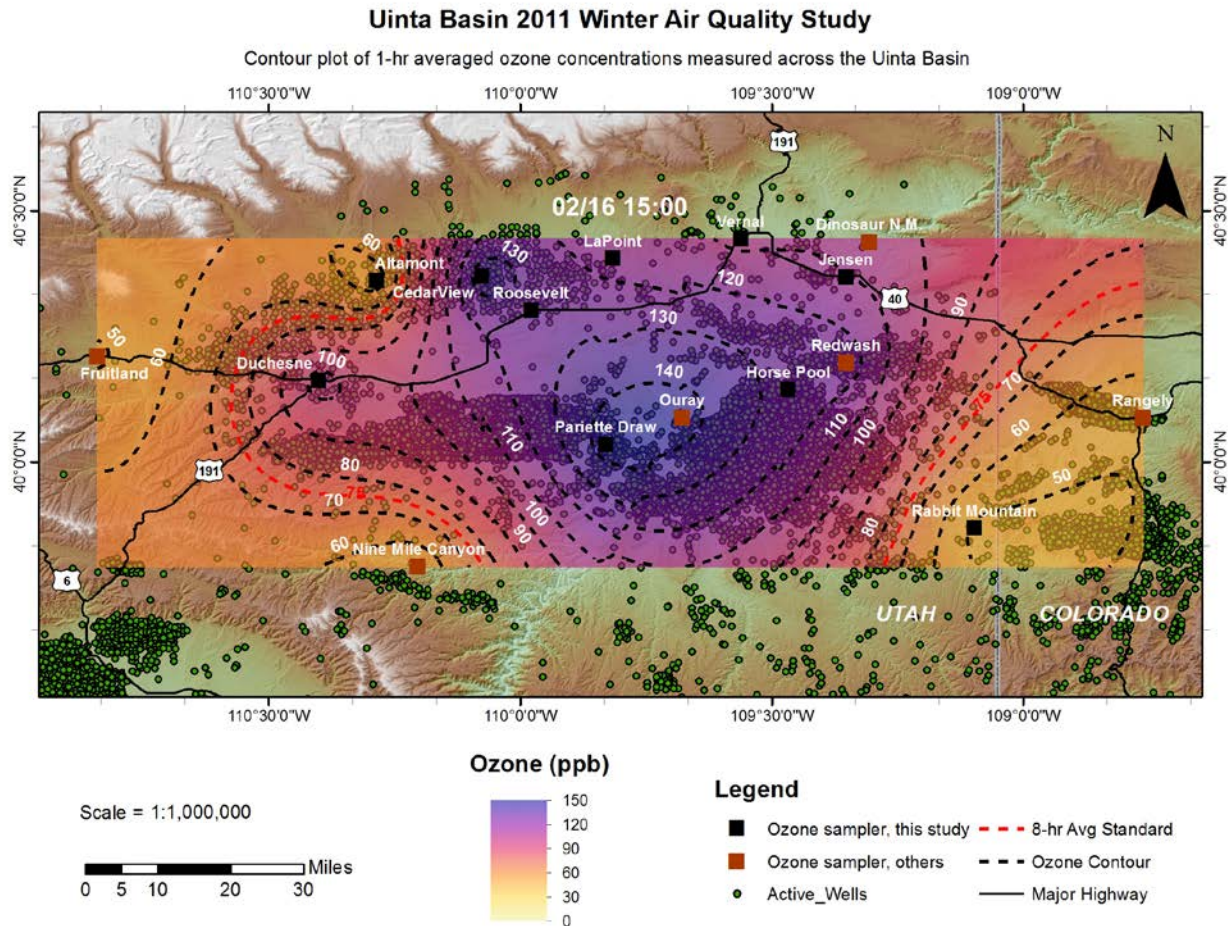
Figure 4-2. Observed 1-hr ozone concentrations within Utah's Uinta Basin (15:00, Feb. 16, 2011) in spatial relation to the region's active oil and gas wells.

Table 4-1 summarizes the available data from the Uinta Basin ozone sampling stations previously discussed. As can be seen, only two sites within the study region, Fruitland and Nine Mile Canyon, showed no exceedances of the 8-hr ozone standard with maximum 8-hr values of 48.6 and 55.6 ppb, respectively. From these data, it can be seen that these locations, at a minimum, represent the outer boundaries of the ozone-impacted areas of the Uinta Basin. Additionally, three other sites, Altamont, Rabbit Mountain, and Rangely (CO), had fewer than four 8-hr exceedances and would not be consider nonattainment with fourth highest 8-hr concentrations of 68.5, 73.4 and 73.4 ppb, respectively, for this winter measurement period. The data from these "fringe" sites suggest that the ozone concentrations observed during the wintertime inversion periods are a function of local topography, meteorology, and ozone precursor abundance rather than any exterior mid- or long-range transport.

Table 4-1. Compiled ozone concentration data from the Uinta Basin 2010–2011 wintertime ozone study.

Site ID	Highest 1-Hr (ppb)	Highest 8-Hr (ppb)	4th Highest 8-Hr (ppb)	# of 8-hr Exceedances
Altamont	91.1	79.8	68.5	1
Cedarview	137.5	122.7	101.0	18
Dinosaur N.M. (NPS)	112.1	106.8	91.0	9
Duchesne	127.0	105.7	81.5	6
Fruitland (UDAQ/BLM)	55.4	48.6	45.9	0
Horse Pool	136.5	129.3	117.1	25
Jensen	110.4	102.2	81.6	9
Lapoint	125.9	118.7	101.3	20
Nine Mile Canyon (BLM)	68.3	55.6	50.2	0
Ouray (Golder)	149.0	139.1	116.4	25
Pariette Draw	144.5	134.6	121.6	19
Rabbit Mountain	102.0	91.5	73.4	3
Rangely, CO (BLM/NPS)	93.6	88.6	73.4	3
Red Wash (Golder)	140.0	125.1	100.6	22
Roosevelt	123.7	116.3	103.6	19
Vernal	107.0	95.1	84.9	7

Table 4.1 also shows that all of the other sites exceeded the 8-hr standard four or more times. The fewest exceedances of these nonattainment sites were observed at Duchesne (six exceedances, fourth highest 8-hr ozone = 81.5 ppb). Two sites, Ouray and Horse Pool, tied with the greatest number of exceedances (25) with fourth highest concentrations of 116.4 and 117.1 ppb, respectively. The Pariette Draw location recorded the highest 8-hr value at 121.6 ppb.

The data tabulated in Table 4.1 are also shown graphically in Fig. 4-3. The contour lines represent an interpolated fit (Kriging method) to the observed number of 8-hr exceedances as a function of the site location; the red line represents the approximate, fitted boundary of the area that could potentially be perceived to be nonattainment relative to the current ozone NAAQS (75 ppb, 8-hr). The shaded region represents a color-graded exceedance scale (the darker the color the more 8-hr exceedances) bounded by the locational coordinates of the observed region. Fig. 4-3 shows that the greatest number of exceedances occurred in the central region of the Basin near Ouray, Horse Pool, and Pariette Draw.
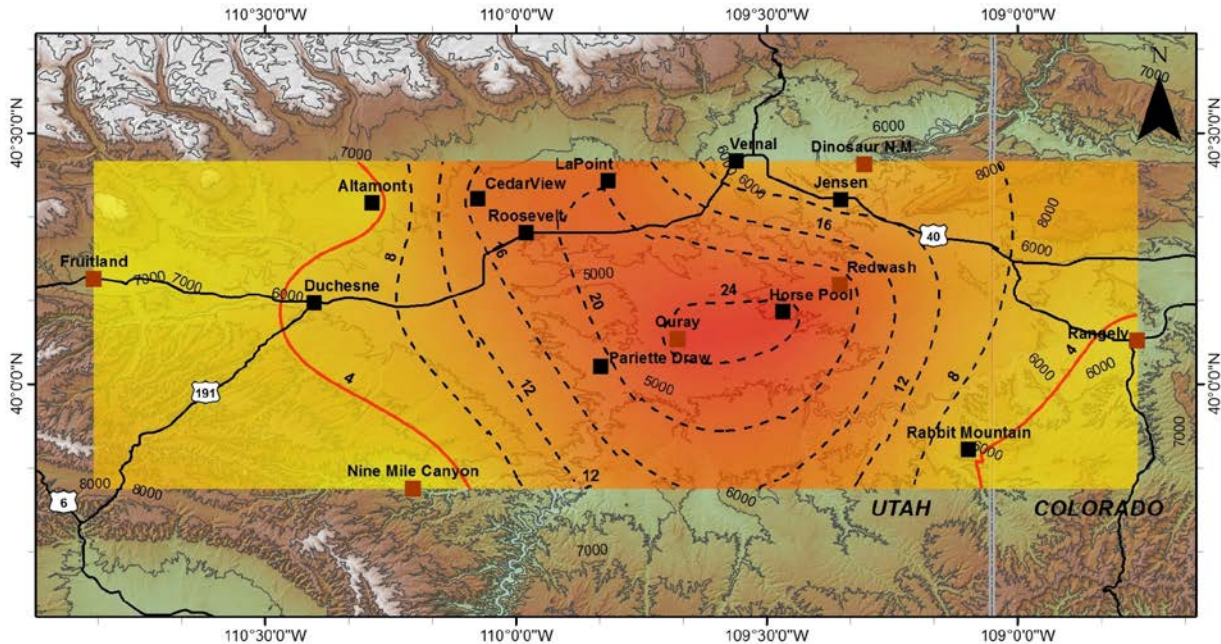
Figure 4-3. An isoplethic representation of the number of 8-hr ozone NAAQS exceedances observed during the 2010-11 winter study period. The red contour line approximately bounds the region observed to be nonattainment based on the fourth highest 8-hr average.

It has been speculated that the Uinta Basin ozone concentrations may also be partially a function of local elevation, with the hypothesis that ozone, or perhaps even the precursor species, tend to concentrate in lower regions due to drainage air flows. In other words, even under the apparent light winds within an inversion event, the air parcels would tend to concentrate ozone and precursor species following the general topography of the region's broad river valleys. This process is often referred to as orographic flow. The potential for this phenomenon is examined in Fig. 4-4. As can be seen, there is a moderate linear relationship ($R^2 = 0.7218$) between some of the sites and the local elevation, but seven of the locations (Cedarview, Lapoint, Red Wash, Roosevelt, Horse Pool, Pariette Draw, and Ouray) displayed no obvious relationship between elevation and number of exceedances. These sites essentially represent the core of the oil and gas field source areas where the ozone concentration is high enough to exceed the NAAQS regardless of the elevation of this region. Additionally, Fig. 4-4 indicates that the average Basin-wide inversion elevation can be estimated somewhere between 5500 and 6000 ft asl (1676-1829 m agl), and sites located above the inversion do not experience levels of ozone that exceed the NAAQS. The argument could be made that Rangely, CO, and Nine Mile Canyon should also be listed as "out of the Basin inversion area" based on number of exceedances, but these sites may also represent fairly isolated locations on the edge of the Basin's topographical boundaries.
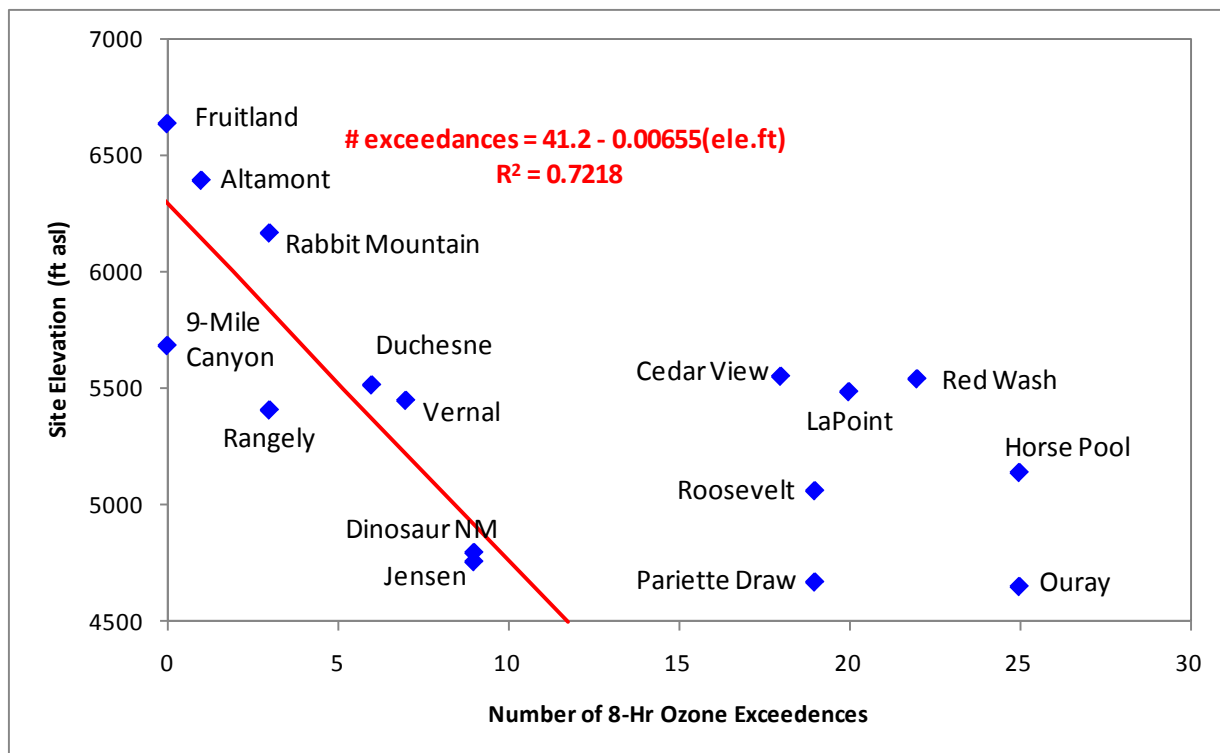
Figure 4-4. Number of 8-hr exceedances at each sampling site as a function of site elevation.

It could also be speculated that the concentration of ozone precursors was related to the proximity of the monitoring site to oil and gas wells. Table 4-2 summarizes available information on the number of wells within 5 km and 10 km radii of each of the sample locations. As can be seen, the monitoring locations with the greatest number of nearby wells also tended to have the highest ozone concentrations (1-hr and 8-hr) and the greatest number of NAAQS exceedances. Curiously, a few of the locations with a significant number of nearby wells (Altamont, Nine Mile Canyon, and Rangely, CO) were shown to have relatively few exceedances. These seeming exceptions may be a function of the previously discussed topographic "fringe" locations or of elevation above the Basin-wide inversion layer (approximately 5500-6000 ft asl).

Table 4-2. Available number of active wells within 5 and 10 km radii of each ozone monitoring site.

Site	# of wells (5 km radius)	# of wells (10 km radius)
Altamont	46	176
Cedarview	62	204
Dinosaur	1	37
Duchesne	26	91
Fruitland	1	8
Horse Pool	397	1083
Jensen	27	90
Lapoint	14	70
Nine-mile	68	152
Ouray	46	412
Pariette Draw	135	492
Rabbit Mtn.	9	75
Rangely, CO	112	295
Red Wash	155	442
Roosevelt	34	109
Vernal	8	55

4.2   SITE SPECIFIC OZONE PROFILES

For each sampling location, the following subsections show the overall winter-long ozone (1-hr average) time series as well as average 1-hr diurnal patterns for two specific time periods: (1) a basin-wide clean, low-ozone period from February 2 through February 6, 2011; and (2) an inversion, high-ozone period from February 10 through February 16, 2011. These specific periods were selected to show the average diurnal behavior for a time period dominated by dynamic meteorology (frontal/storm passages) and a time period typified by a sustained inversion event. The graphs for these time series plots are shown alphabetically in Fig. 4-5 through Fig. 4-36. The error bars included on the diurnal figures represent the 95% confidence intervals about each of the hourly averaged data points. The following discussion is limited to examples of ambient ozone behavior at a few representative sites; however, data from all of the sites collected by the USU/EDL sample team or external partners are included.

Table 4-1 showed that the site with the consistently lowest ambient ozone concentrations was the Fruitland location. The Fruitland ozone concentration time series for the sample period is shown in Fig. 4-13. Throughout the observed period, the ozone measured at the Fruitland sampling site remained relatively low, without significant diurnal changes or inversion-related buildups. This is consistent with sites believed to represent free tropospheric background air masses. This assumption is further supported by the fact that, at the 95% confidence interval, the average diurnal profiles for a "clean" (Feb. 2-6) period and a "dirty" period (Feb. 12-16) were statistically indistinct, as shown in Fig. 4-14. Furthermore, in neither the time series chart nor the average diurnal behaviors graph did the daily ozone concentrations change by more the 20-30 ppb between the daylight and nighttime hours, indicating very little local photochemical ozone formation. The consistently low ozone concentrations at the Fruitland site also suggest that neither ozone nor its precursor species are transported into the Uinta Basin from the Wasatch Front area (i.e., Salt Lake City), which generally lies upwind from the Basin.

The observed Duchesne ozone concentration time series for the winter sample period is shown in Fig. 4-11. In contrast to the Fruitland observations, the recorded ozone concentrations for the same period varied considerably. Unlike the previously described Fruitland time series, the Duchesne data showed obvious diurnal behavior, indicating direct influence of local or regional area ozone formation and destruction reactions, as well as systematic buildup and removal of inversion-driven ozone episodes. The average diurnal profiles for a "clean" (Feb. 2-6) period and a "dirty" period (Feb. 12-16) show (Fig. 4-12) statistically different behavior, particularly during the daylight and early evening hours. During the clean period, as was also observed at the Fruitland location, the day/night differences in ozone concentrations were on the order of 20-30 ppb. During the inverted period, however, the concentrations varied by around 80 ppb throughout the day. Once again, this latter behavior is indicative of significant local/regional photochemical ozone reactions. These concentration levels and diurnal behaviors were also similar to those observed at Dinosaur National Monument (Figures 4-9 and 4-10), Jensen (Figures 4-17 and 4-18), and Vernal (Figures 4-35 and 4-36).

The observed Altamont ozone concentration time series and average diurnal patterns are shown in Figures 4-5 and 4-6, respectively. As can be seen, the behaviors are similar to the Duchesne observations, but generally at lower concentrations and more consistent with those observed at Fruitland. As previously discussed, although near a relatively large number of active wells, the ozone concentrations remained relatively low; however, there were statistically different afternoon/evening hourly values between the low and high ozone periods. The higher, above inversion, elevation of Altamont likely contributed to greater levels of advective (wind-driven) mixing, even during regionally stagnant periods, and, therefore, resulted in lower average ozone concentrations. Similar concentrations and behaviors were also observed at Nine Mile Canyon (Figures 4-21 and 4-22), Rabbit Mountain (Figures 4-27 and 4-28), and Rangely, CO. (Figures 4-29 and 4-30).

As was previously shown in Table 4-1 and Figure 4-1(b), the highest 1-hr and 8-hr ozone concentrations, as well as the greatest number of NAAQS exceedances, were typically observed in a core area centered in the Horse Pool/Ouray/Pariette Draw region. The ozone time series and clean and dirty diurnal behaviors for the Horse Pool site are shown in Figures 4-15 and 4-16, respectively. The ozone time series and diurnal behaviors for Ouray are shown in Figures 4-23 and 4-24, respectively. The ozone time series and diurnal behaviors for the Pariette Draw sampling location are shown in Figures 4-25 and 4-26, respectively. High ozone concentrations and similar differences in diurnal ozone behaviors were noted at Cedarview (Figures 4-7 and 4-8), Lapoint (Figures 4-19 and 4-20), Red Wash (Figures 4-31 and 4-32), and Roosevelt (Figures 4-33 and 4-34).

4.2.1   Altamont

Figure 4-5. Winter 2010–11 Altamont 1-hr average ozone time series observations.
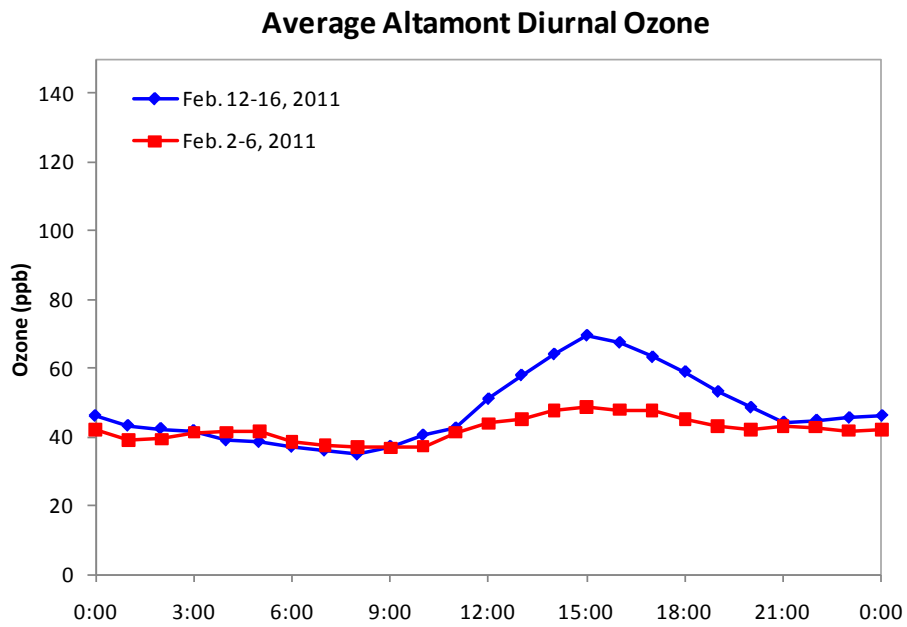
Figure 4-6. Average diurnal ozone measured at the Altamont location for Feb. 2–6 and Feb. 12–16, 2011.

4.2.2   Cedarview

Figure 4-7. Winter 2010–11 Cedar View 1-hr average ozone time series observations. The data gap represents a period when the sample line became blocked by water and ice.

Figure 4-8. Average diurnal ozone measured at the Cedar View location for Feb. 2–6 and Feb. 12–16, 2011.

4.2.3   Dinosaur National Monument

Figure 4-9. Winter 2010–11 Dinosaur National Monument 1-hr average ozone time series observations.
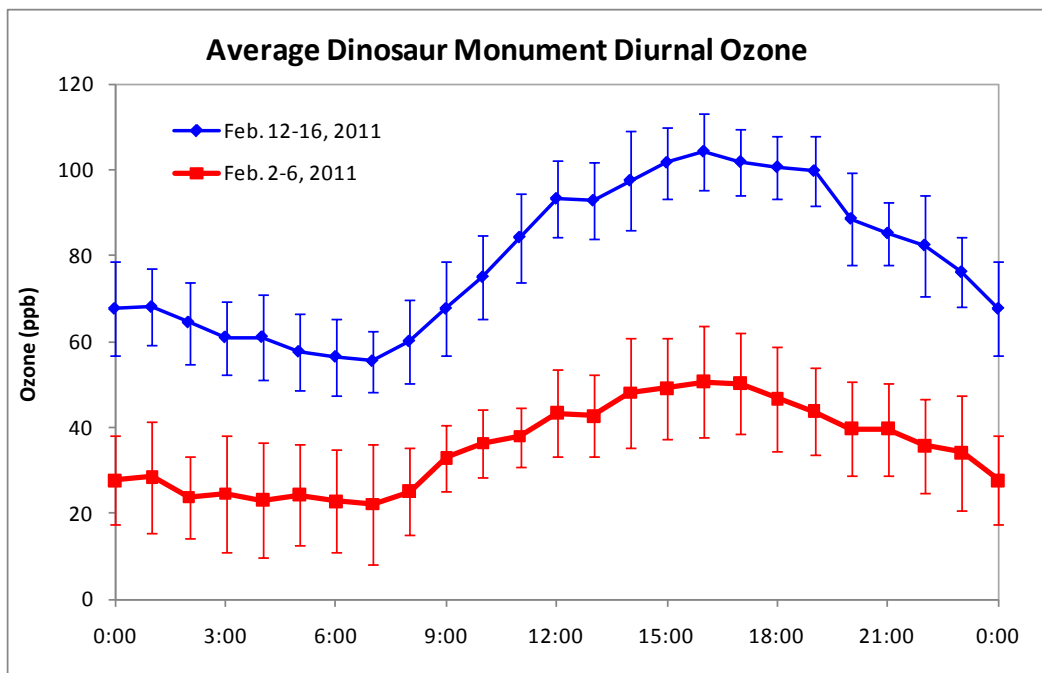
Figure 4-10. Average diurnal ozone measured at the Dinosaur National Monument location for Feb. 2–6 and Feb. 12–16, 2011.

4.2.4   Duchesne
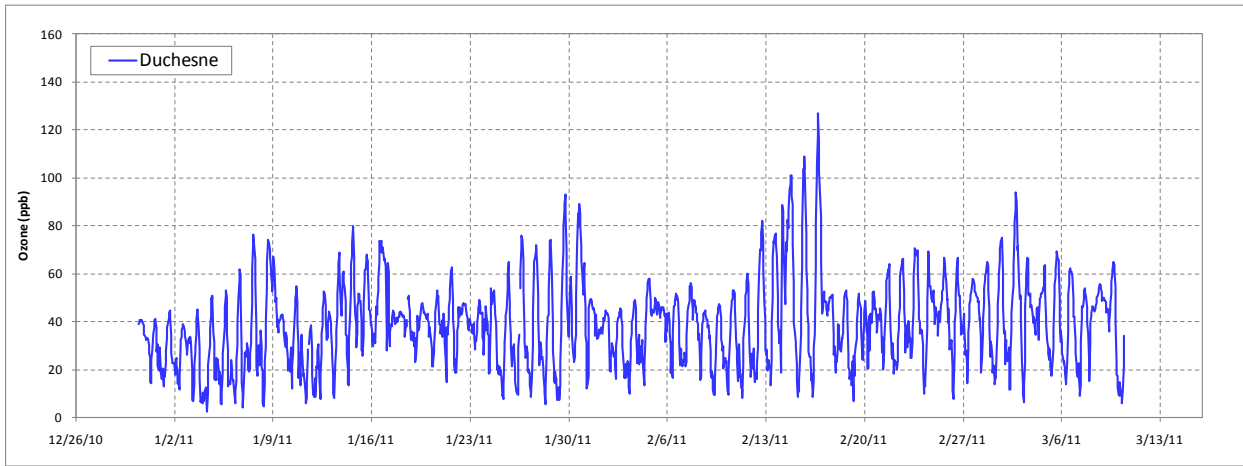
Figure 4-11. Winter 2010–11 Duchesne 1-hr average ozone time series observations.
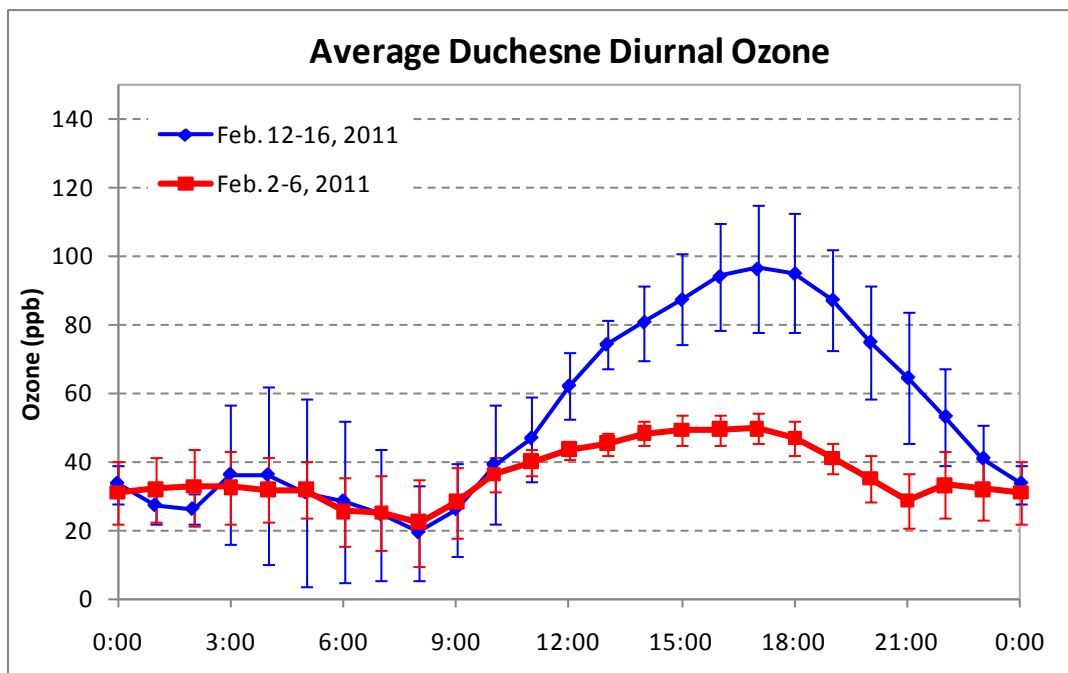
Figure 4-12. Average diurnal ozone measured at the Duchesne location for Feb. 2–6 and Feb. 12–16, 2011.

4.2.5   Fruitland
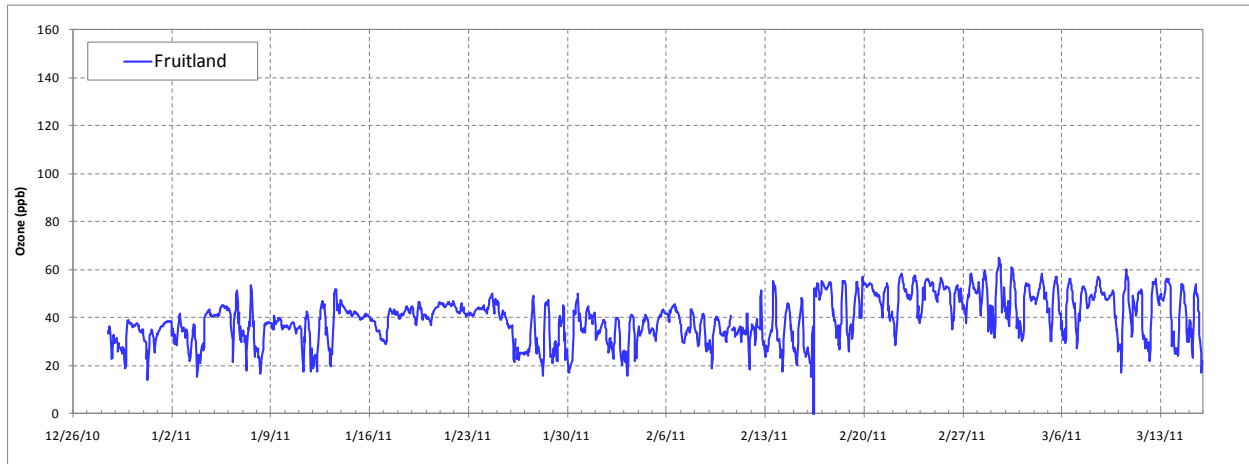
Figure 4-13. Winter 2010–11 Fruitland 1-hr average ozone time series observations.
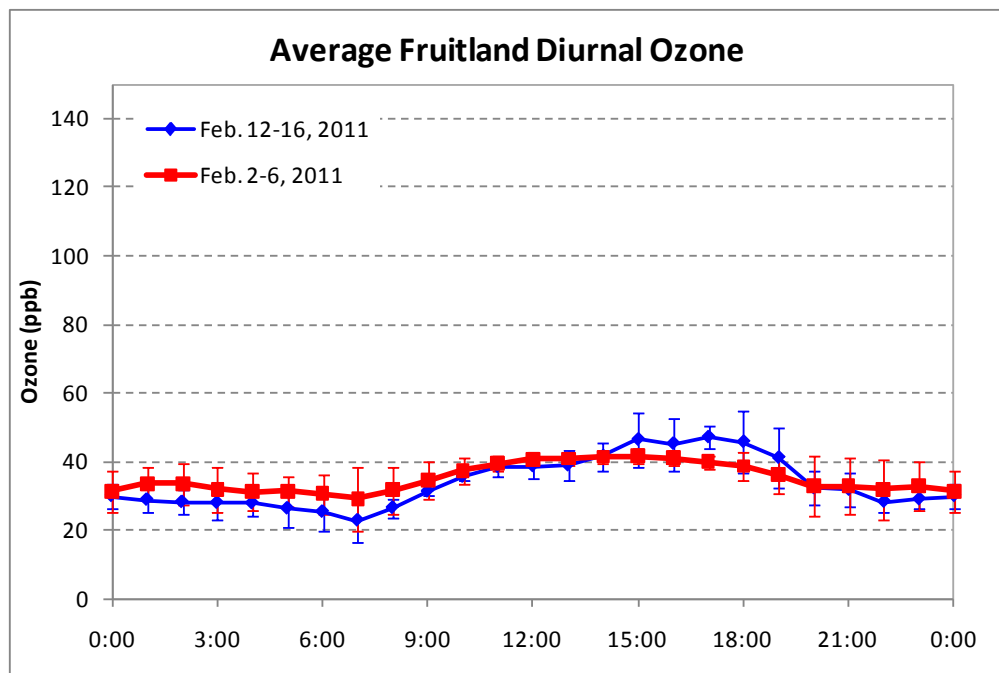
Figure 4-14. Average diurnal ozone measured at the Fruitland location for Feb. 2–6 and Feb. 12–16, 2011.

4.2.6   Horse Pool
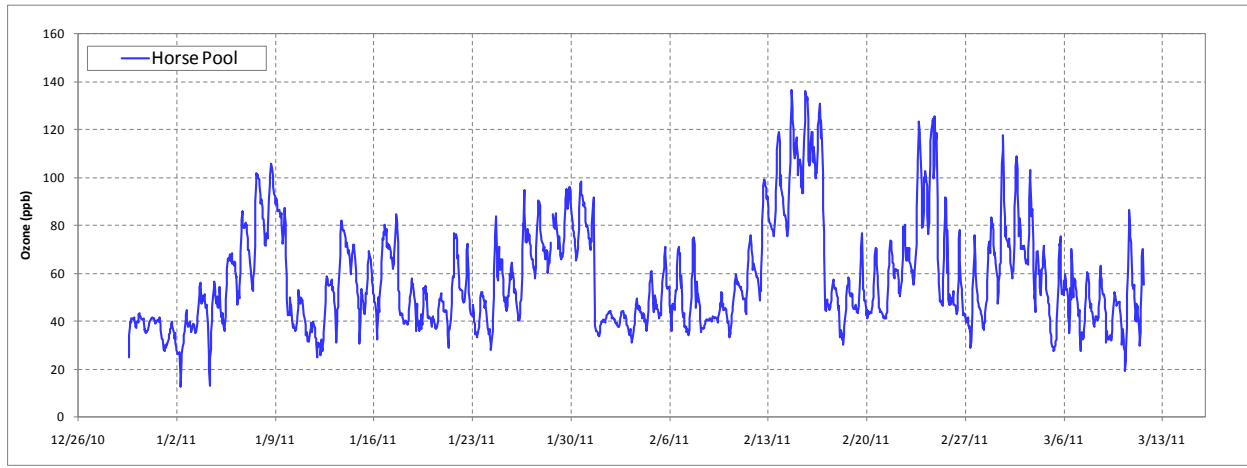
Figure 4-15. Winter 2010–11 Horse Pool 1-hr average ozone time series observations.
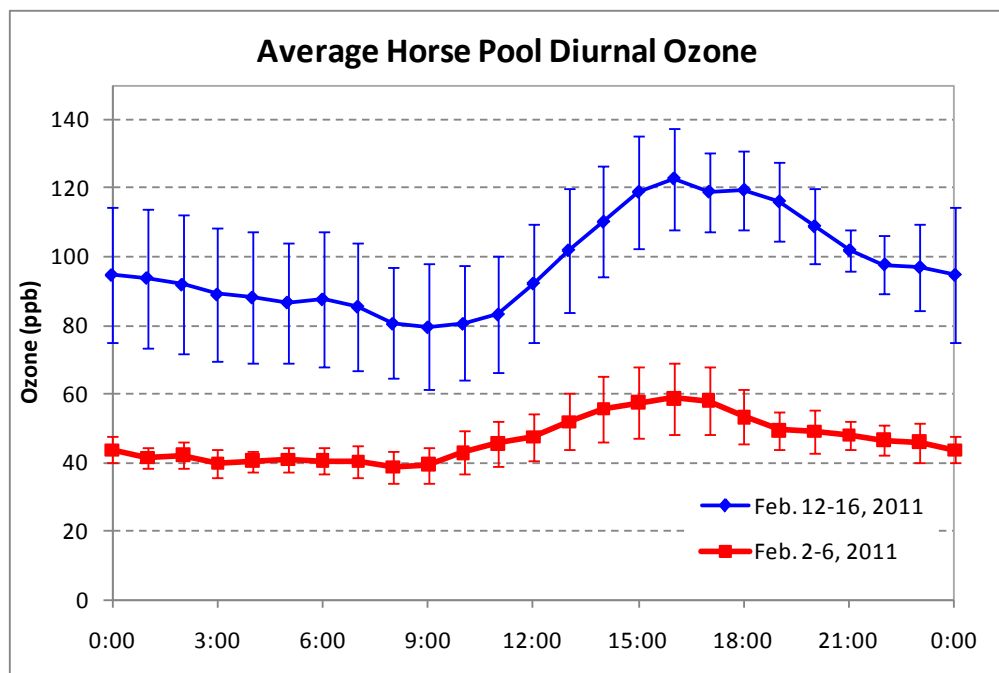
Figure 4-16. Average diurnal ozone measured at the Horse Pool location for Feb. 2–6 and Feb. 12–16, 2011.

4.2.7   Jensen
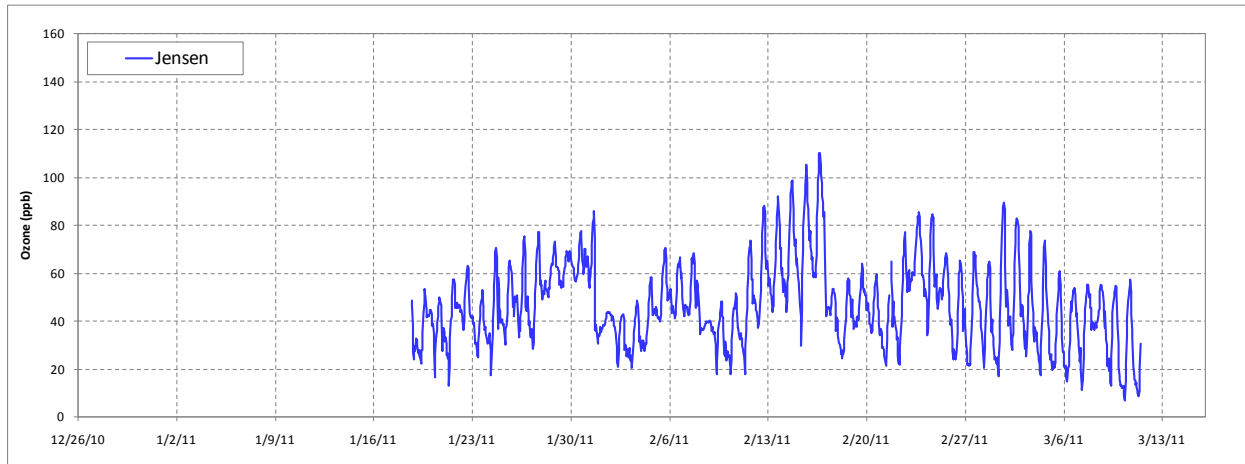
Figure 4-17. Winter 2010–11 Jensen 1-hr average ozone time series observations.
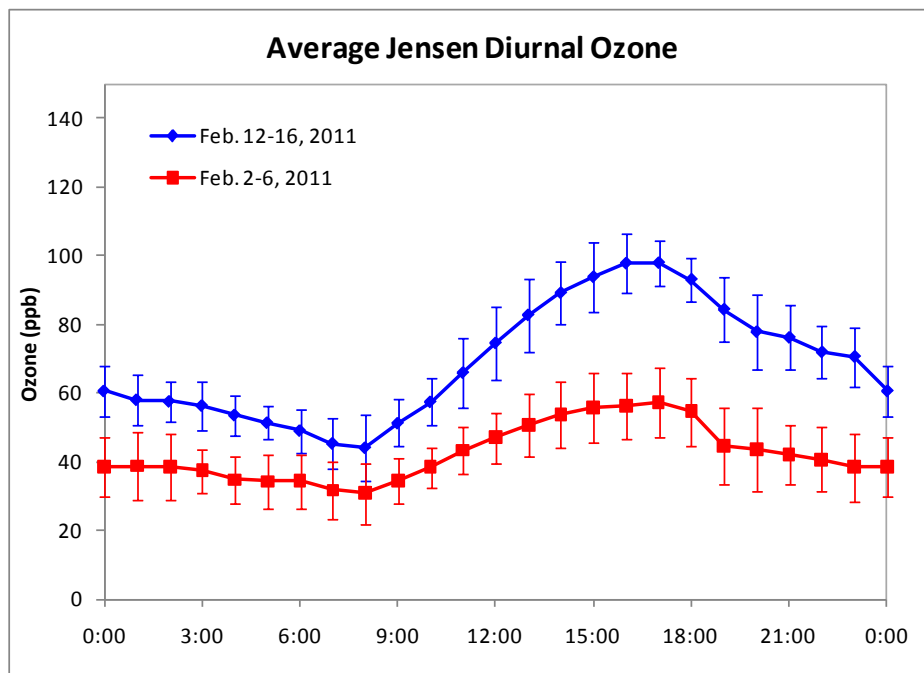
Figure 4-18. Average diurnal ozone measured at the Jensen location for Feb. 2–6 and Feb. 12–16, 2011.

4.2.8   Lapoint
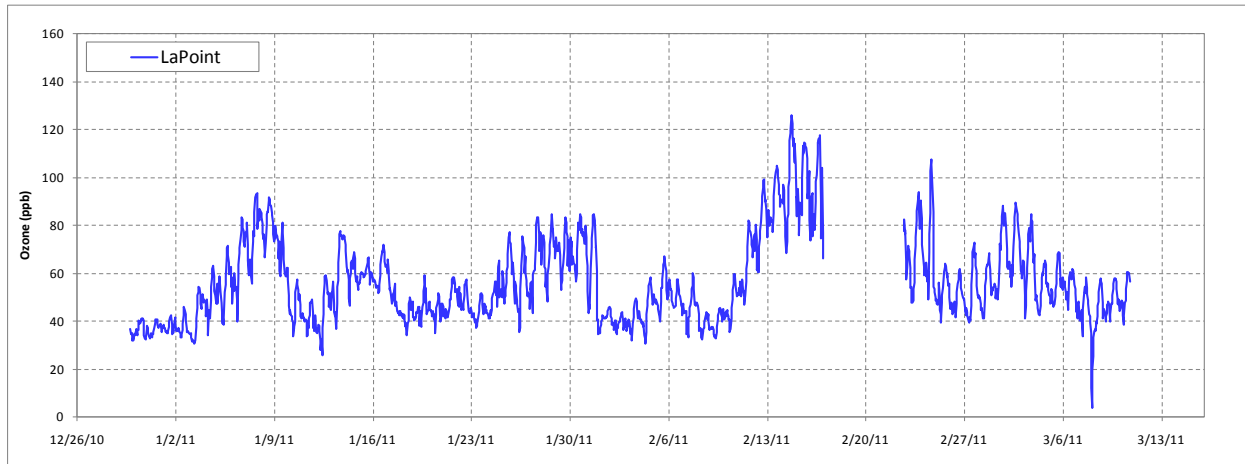
Figure 4-19. Winter 2010–11 Lapoint 1-hr average ozone time series observations. The data gap represents a period when the sample line became blocked by water and ice.
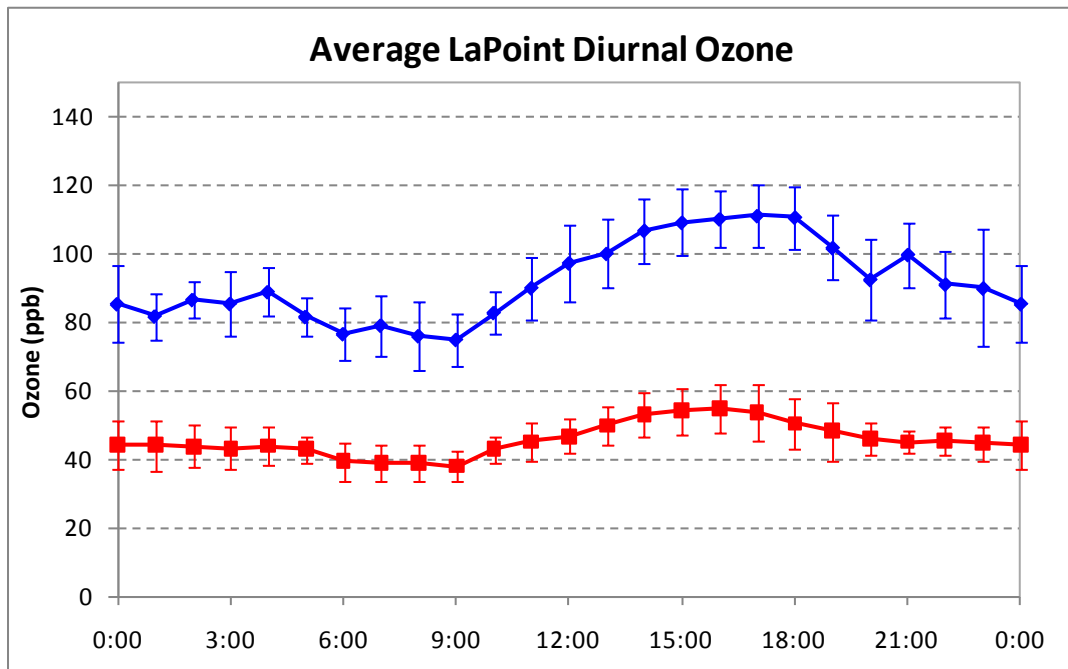
Figure 4-20. Average diurnal ozone measured at the Lapoint location for Feb. 2–6 and Feb. 12–16, 2011.

4.2.9   Nine Mile Canyon
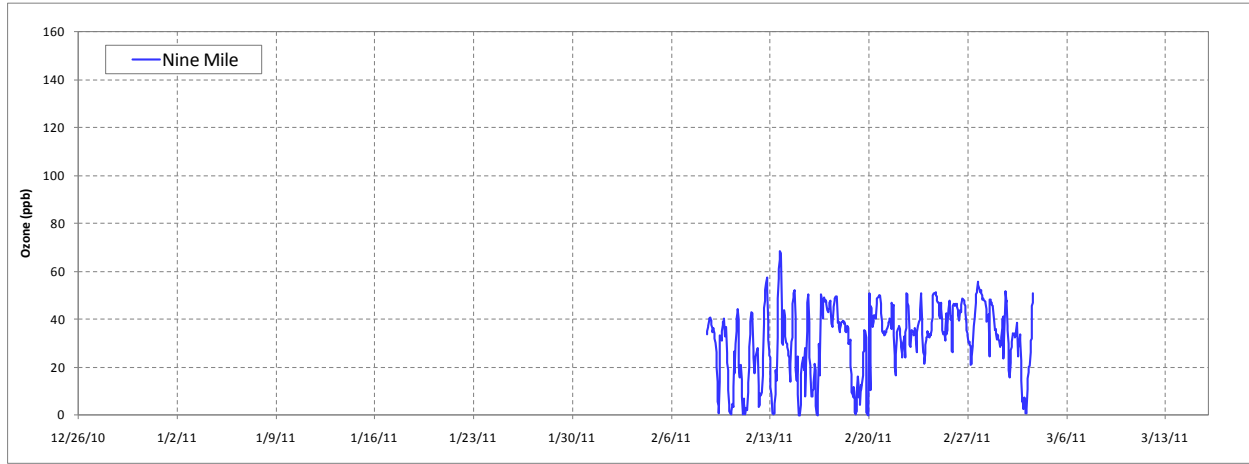
Figure 4-21. Winter 2010–11 Nine Mile Canyon 1-hr average ozone time series observations. Owing to solar power limitations, ozone sampling was not initiated until early Feb. 2011.
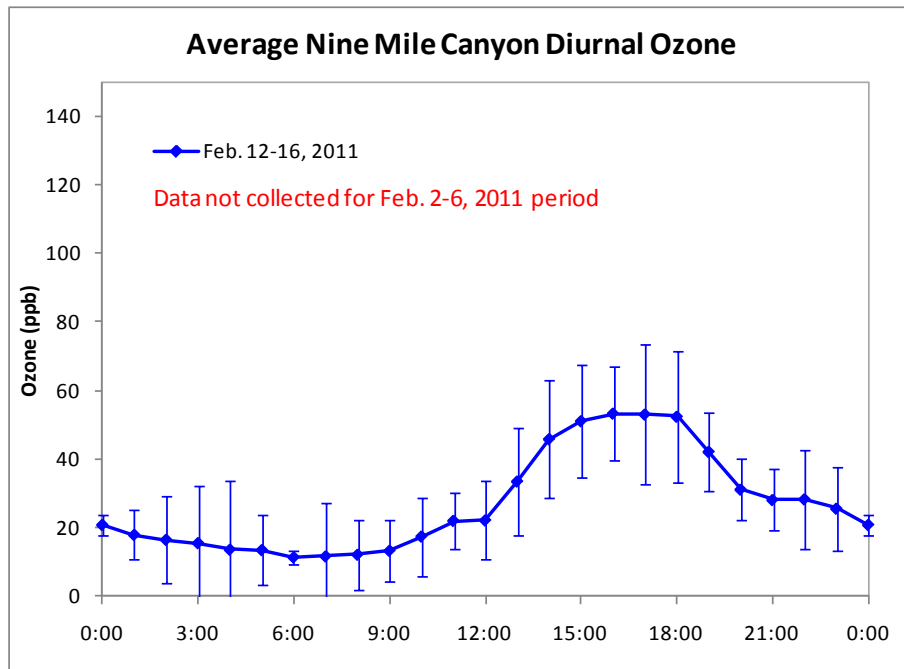
Figure 4-22. Average diurnal ozone measured at the Nine Mile Canyon location for Feb. 12–16, 2011.

4.2.10   Ouray
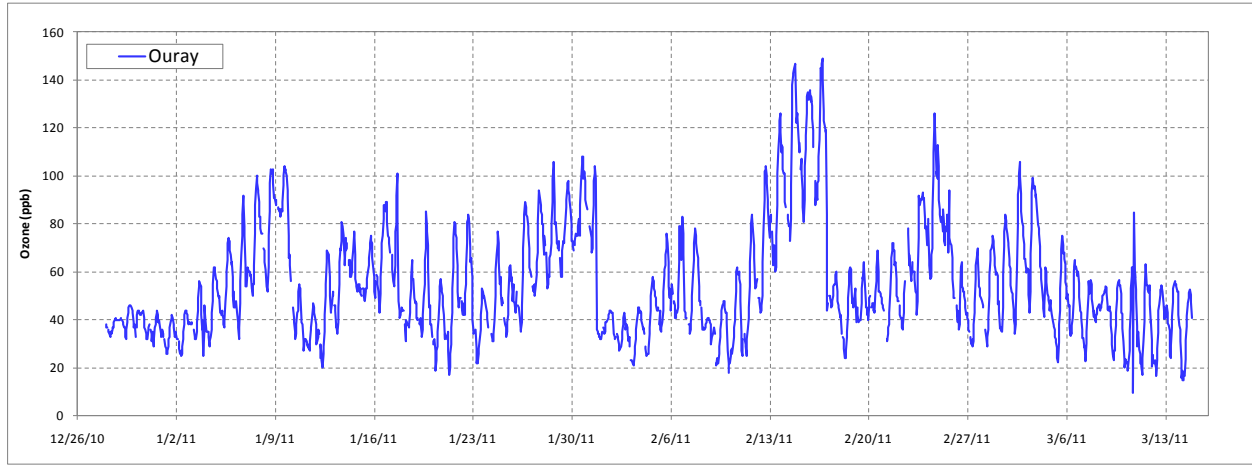
Figure 4-23. Winter 2010–11 Ouray 1-hr average ozone time series observations.
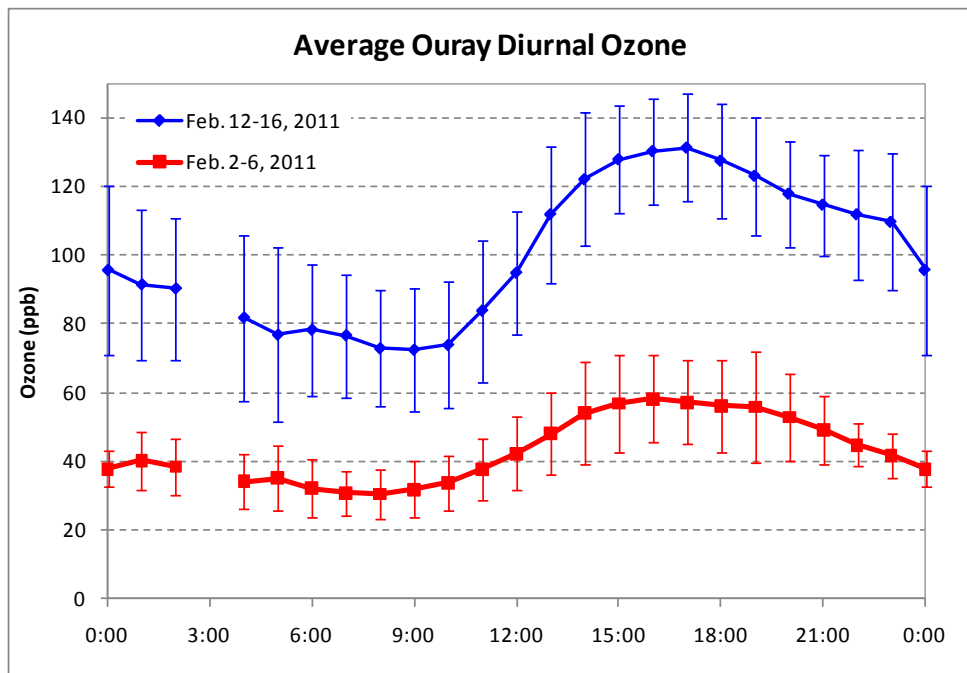
Figure 4-24. Average diurnal ozone measured at the Ouray location for Feb. 2–6 and Feb. 12–16, 2011. The gap in the data at 3:00 represents the automated QA/QC time period.

4.2.11   Pariette Draw
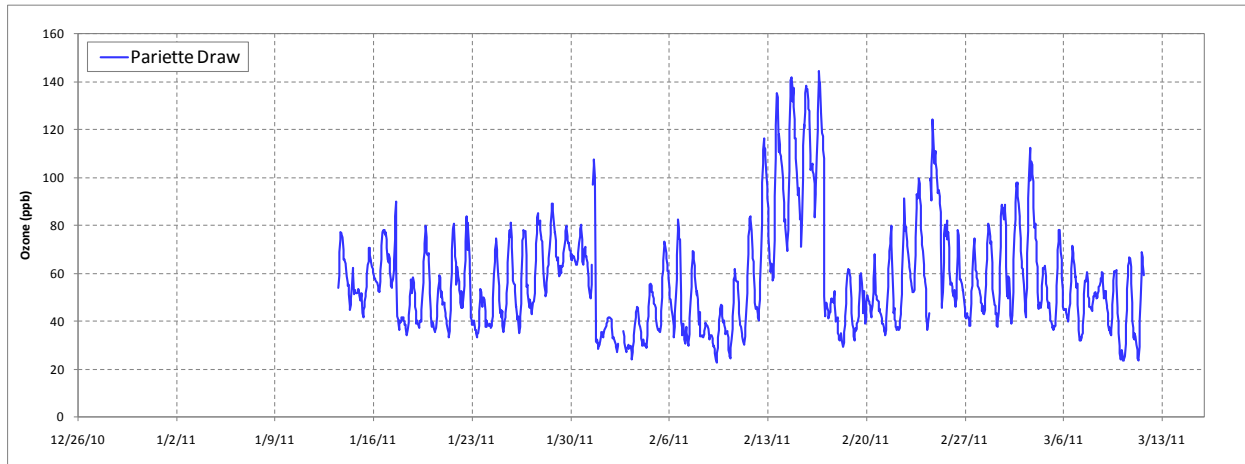
Figure 4-25. Winter 2010–11 Pariette Draw 1-hr average ozone time series observations.
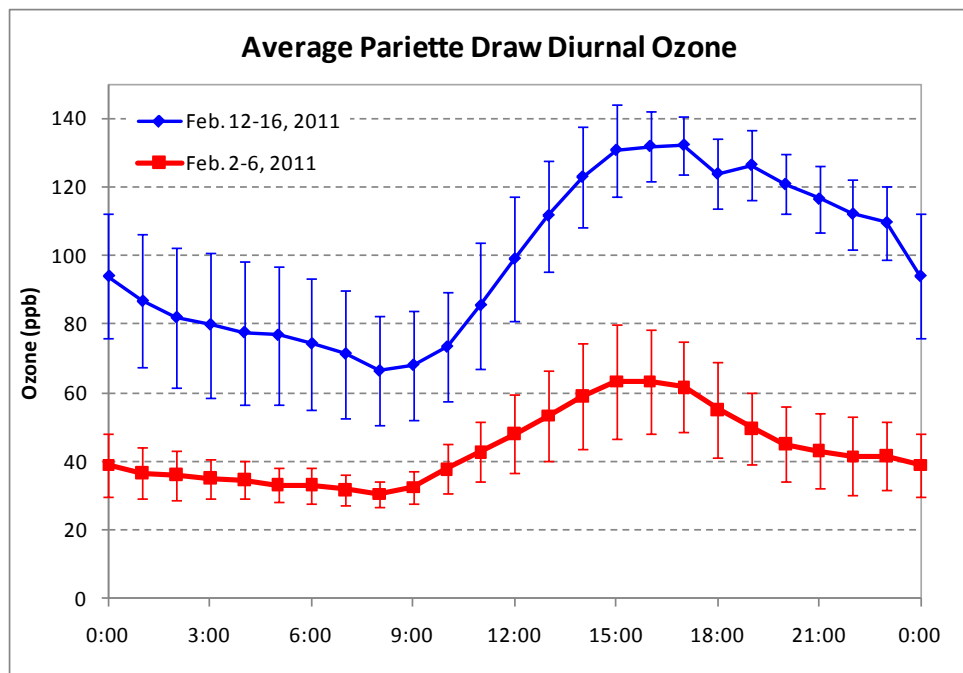
Figure 4-26. Average diurnal ozone measured at the Pariette Draw location for Feb. 2–6 and Feb. 12–16, 2011.
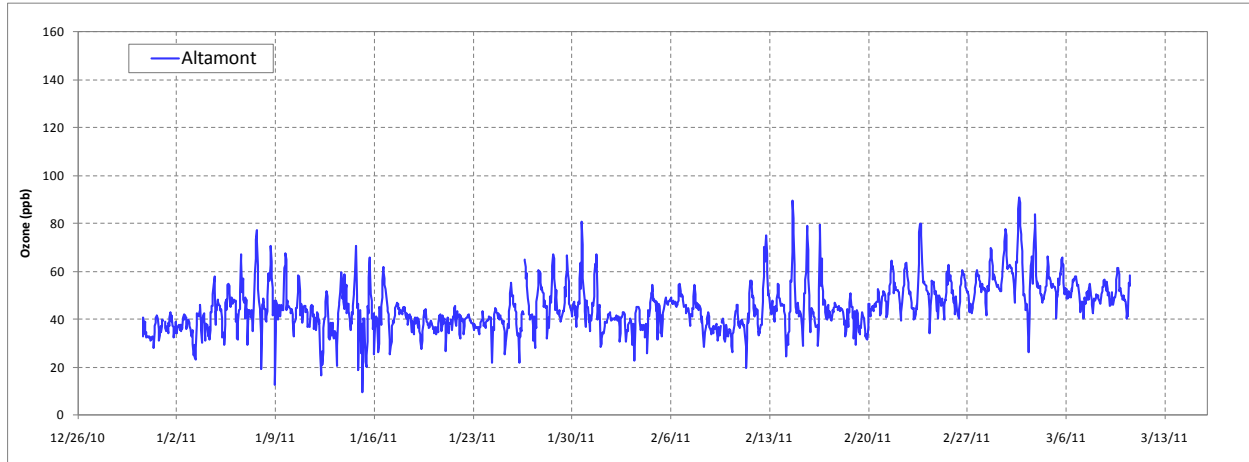
4.2.12   Rabbit Mountain
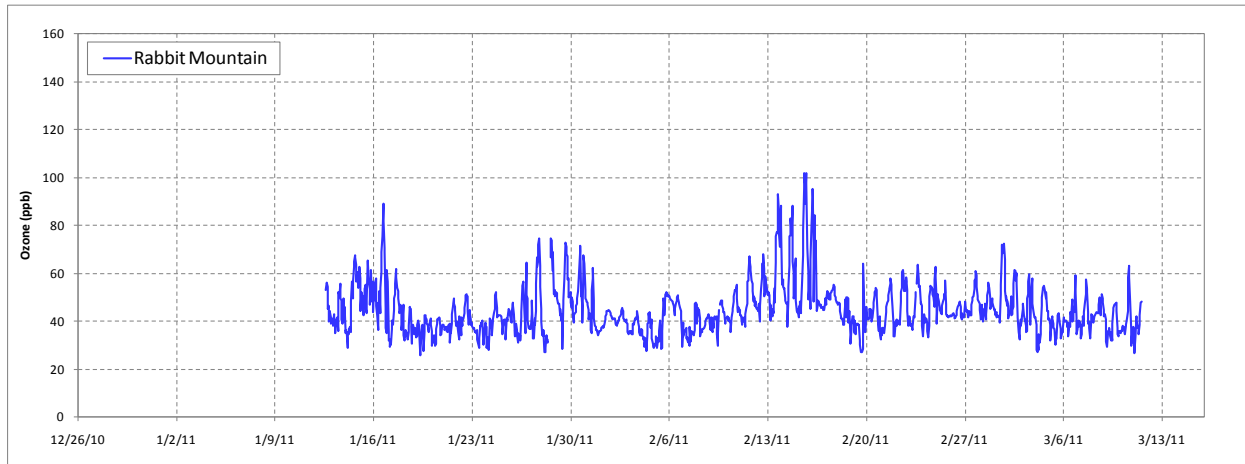
Figure 4-27. Winter 2010–11 Rabbit Mountain 1-hr average ozone time series observations.
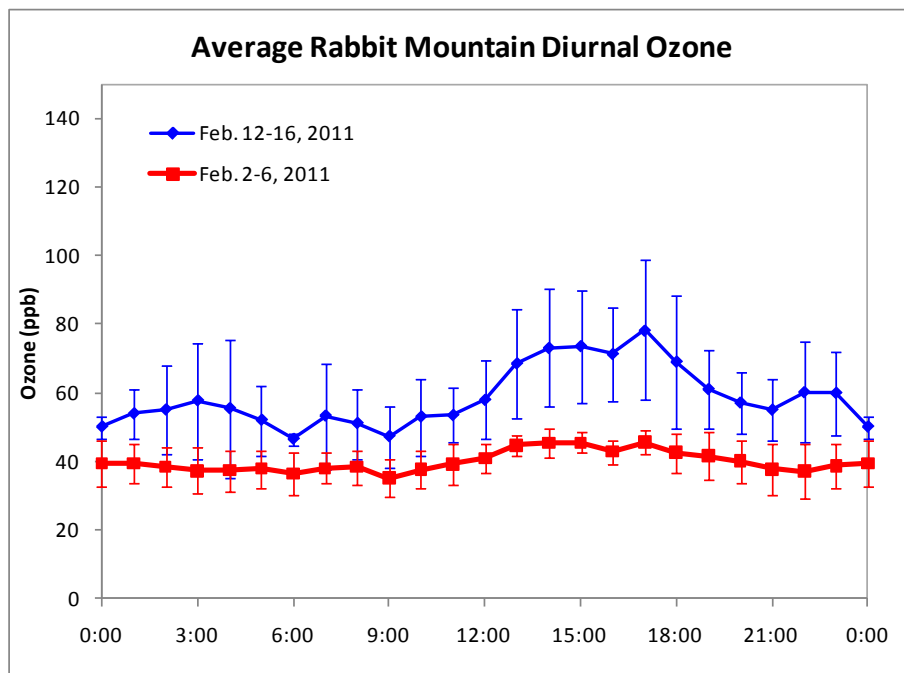
Figure 4-28. Average diurnal ozone measured at the Rabbit Mountain location for Feb. 2-6 and Feb. 12-16, 2011.

4.2.13   Rangely, CO.
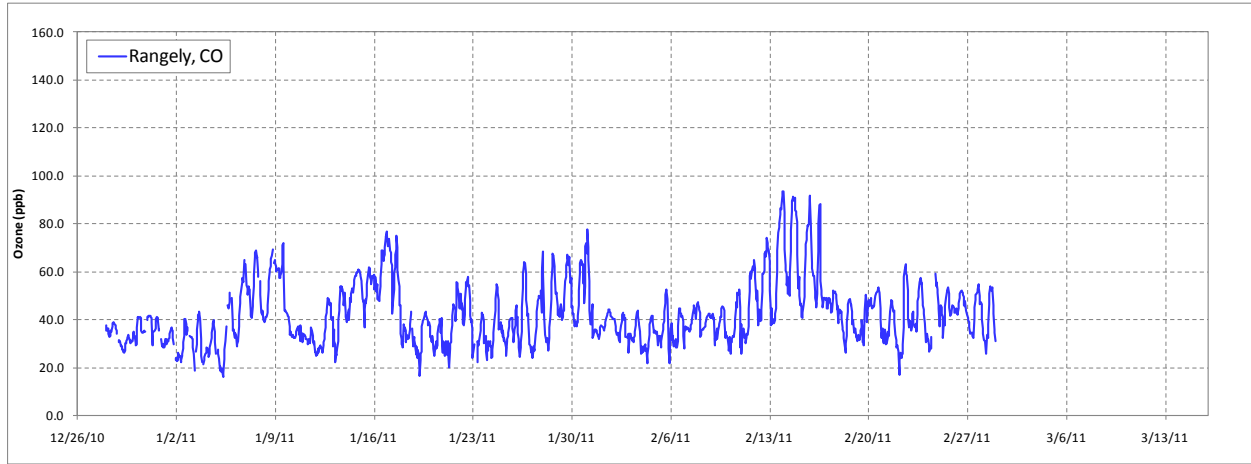
Figure 4-29. Winter 2010–11 Rangely, CO, 1-hr average ozone time series observations.
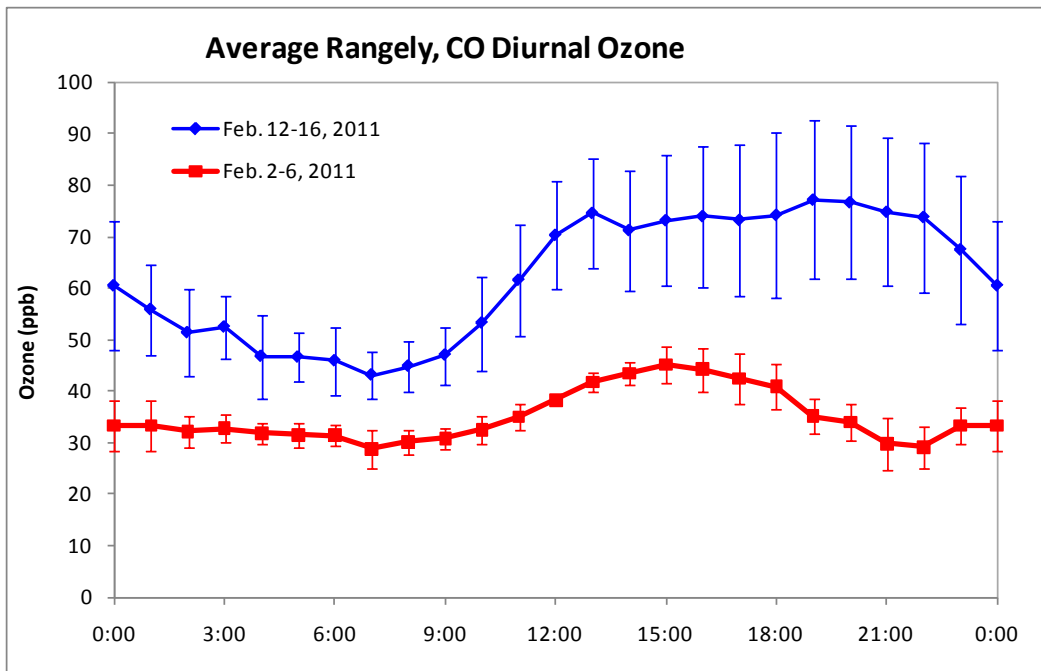
Figure 4-30. Average diurnal ozone measured at the Rangely, CO, location for Feb. 2–6 and Feb. 12–16, 2011.

4.2.14   Red Wash
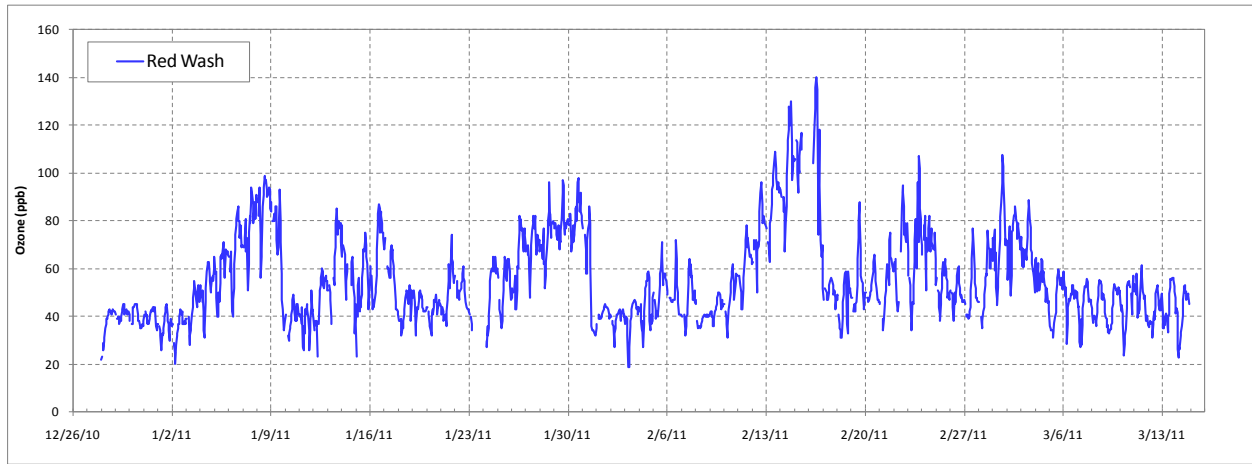
Figure 4-31. Winter 2010–11 Red Wash 1-hr average ozone time series observations.
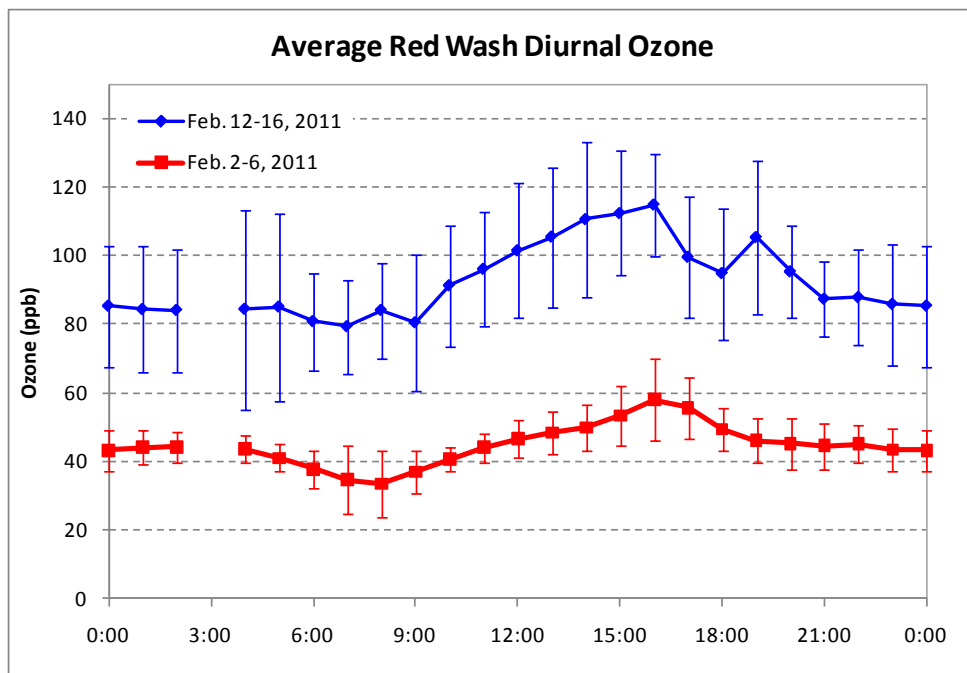
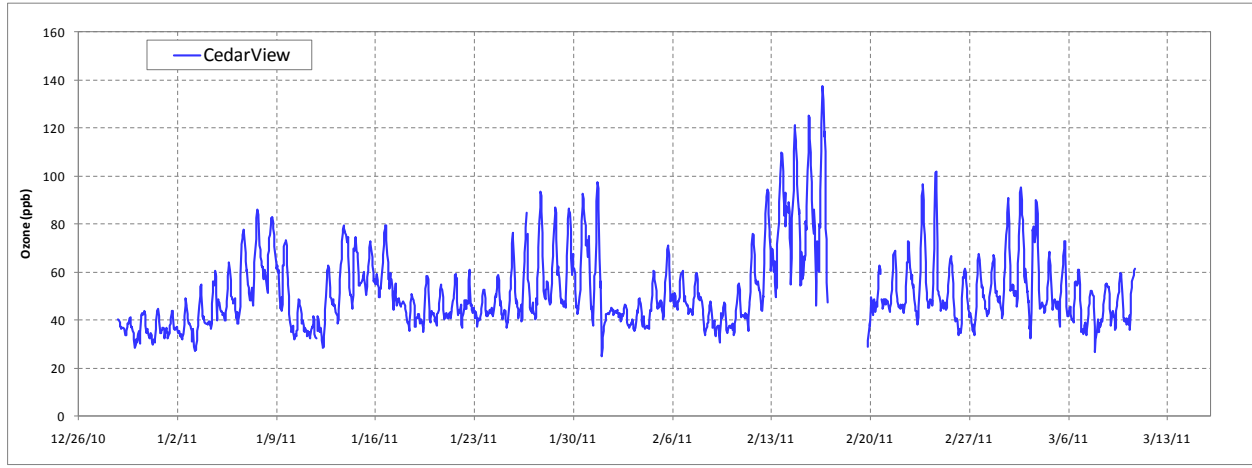**Figure 4-32. Average diurnal ozone measured at the Red Wash location for Feb. 2–6 and Feb. 12–16, 2011. The gap in the data at 3:00 represents the automated QA/QC time period.**

4.2.15   Roosevelt
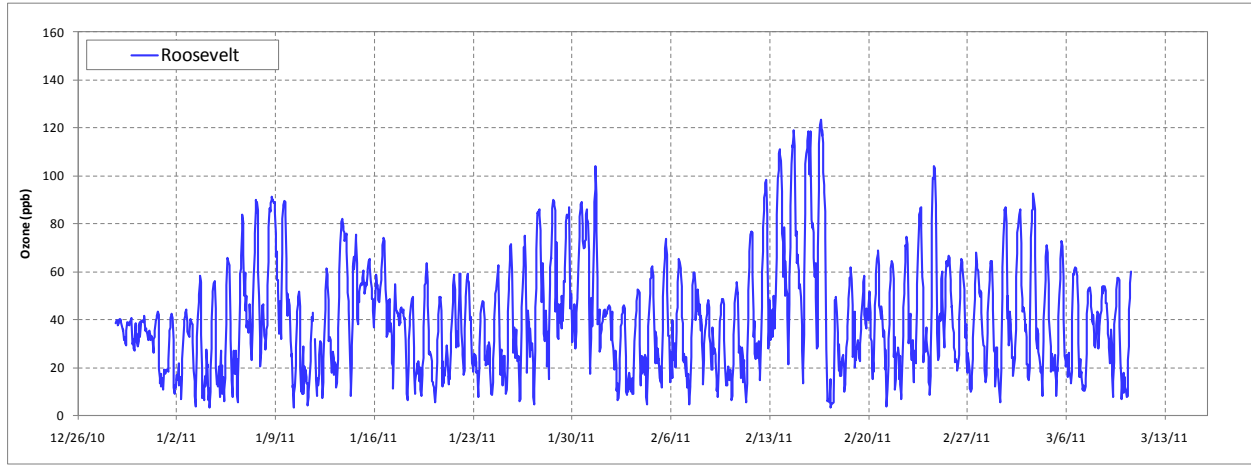
Figure 4-33. Winter 2010–11 Roosevelt 1-hr average ozone time series observations.
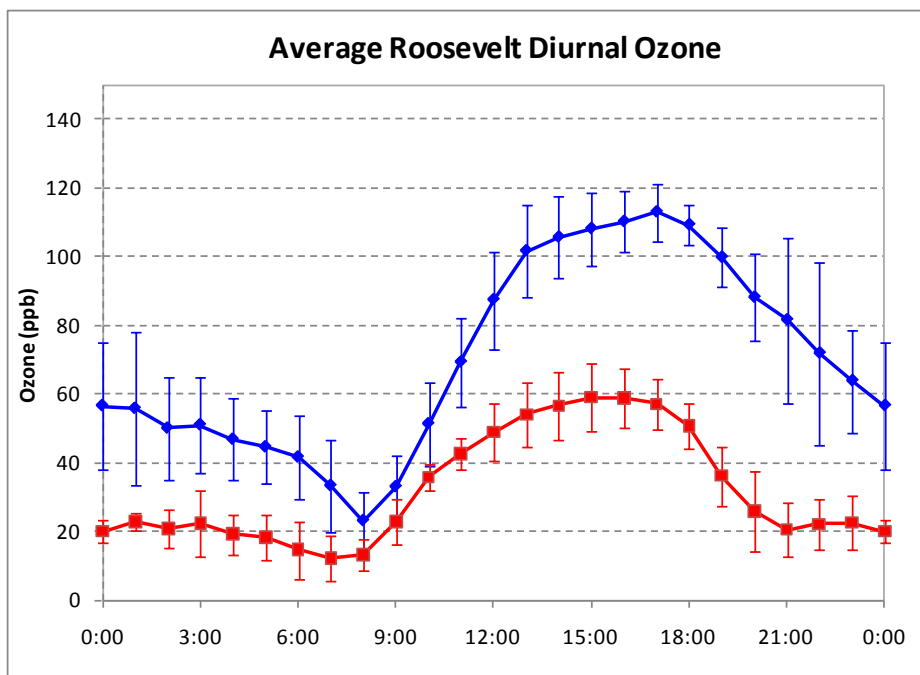
Figure 4-34. Average diurnal ozone measured at the Roosevelt location for Feb. 2–6 and Feb. 12–16, 2011.

4.2.16   Vernal
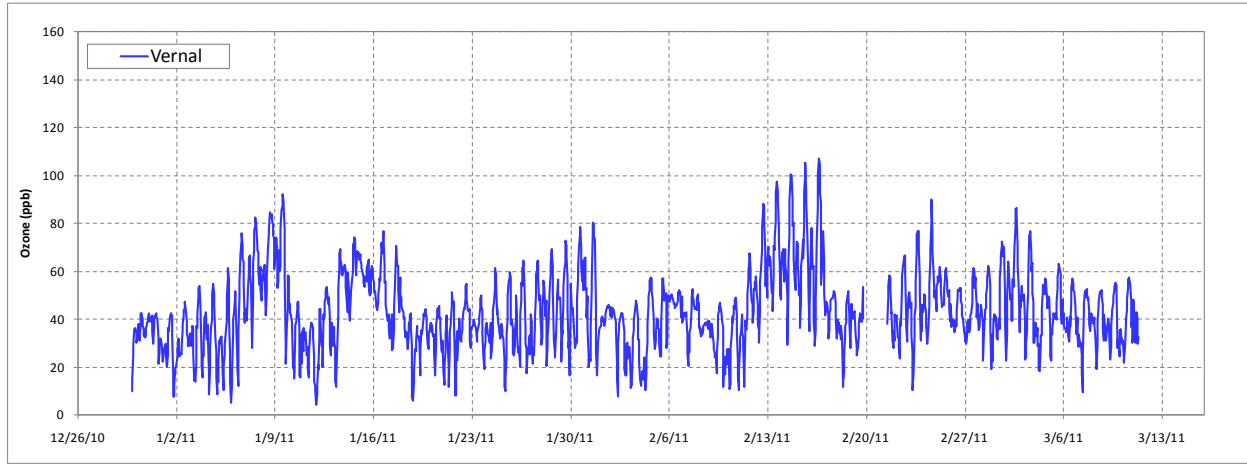
Figure 4-35. Winter 2010–11 Vernal 1-hr average ozone time series observations. The data gap represents a period when the sample line became blocked by water and ice.
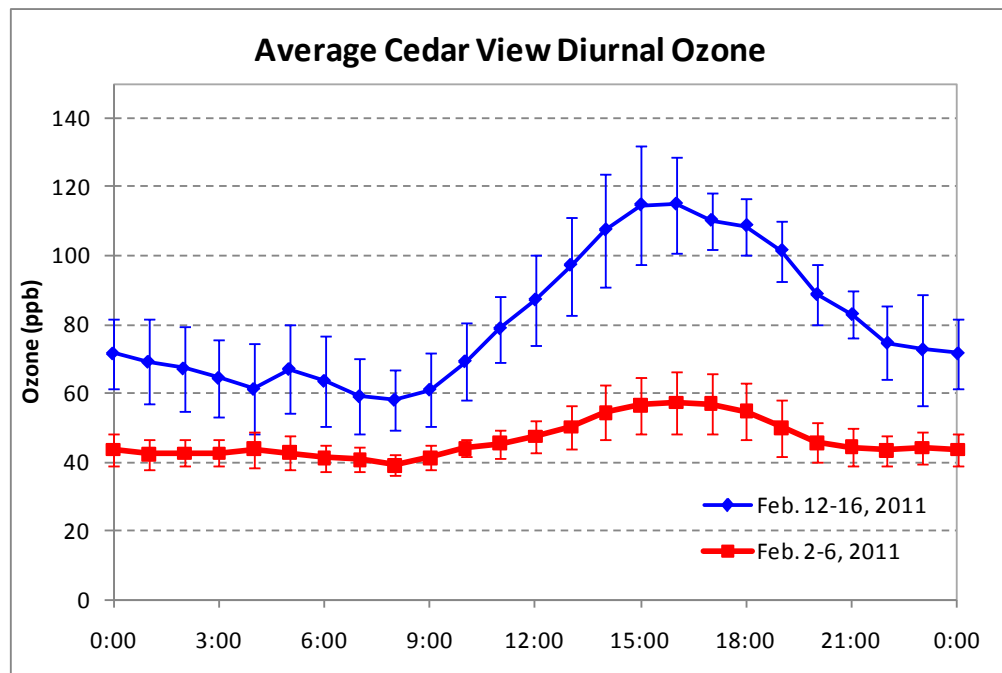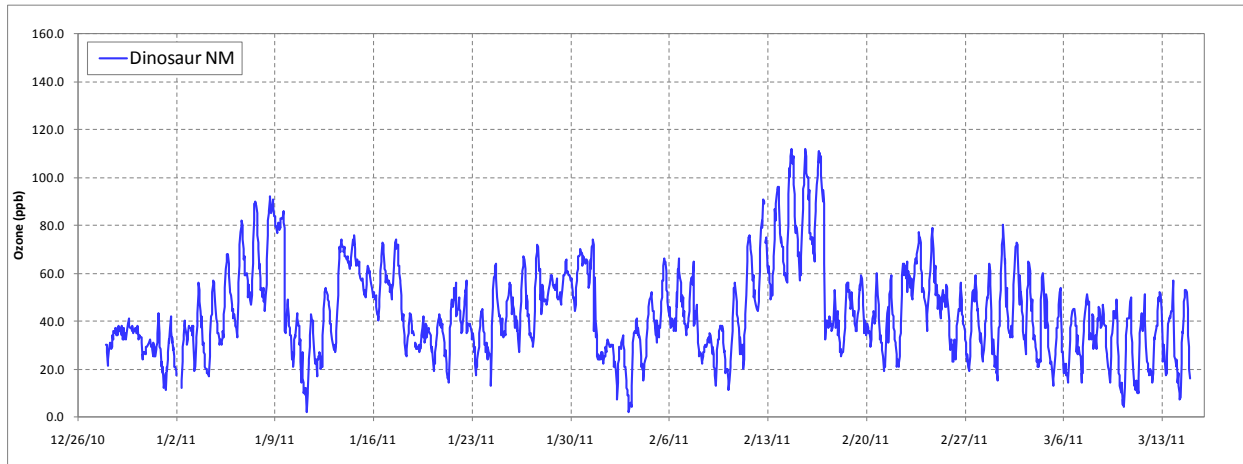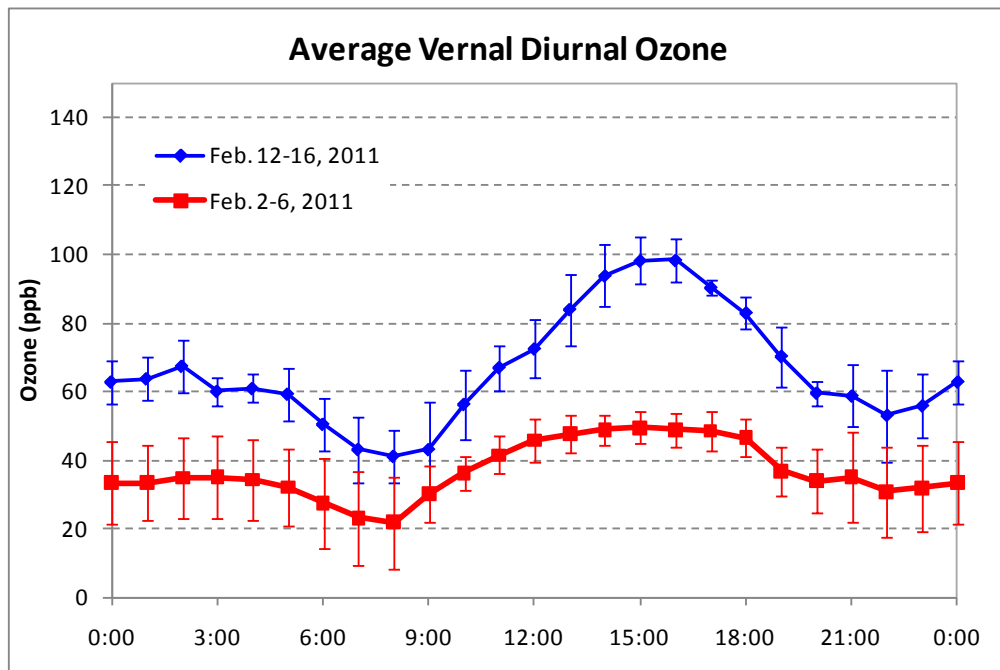

Figure 4-36. Average diurnal ozone measured at the Vernal location for Feb. 2–6 and Feb. 12–16, 2011.

4.3 VERTICAL OZONE PROFILE

Though not part of the original project plan, a tethered balloon-borne modified 2B Technologies ozone monitor was used to examine the vertical ozone profile on a single day at the Red Wash sampling location. Fig. 4-37 shows the four vertical ozone profiles measured on February 24, 2011 at 8:00 MST, 9:00 MST, 13:00 MST and 16:00 MST. As can be seen, the ground level ozone concentrations were greater than the ozone concentrations at higher elevations at all observed time periods throughout the day. Furthermore, it can be seen that the thickness of the zone of higher ozone concentrations seemed to grow throughout the day. In addition, the balloon-borne ground level ozone values were very similar to the values provided by the collocated Golder Associates Red Wash ozone monitor.
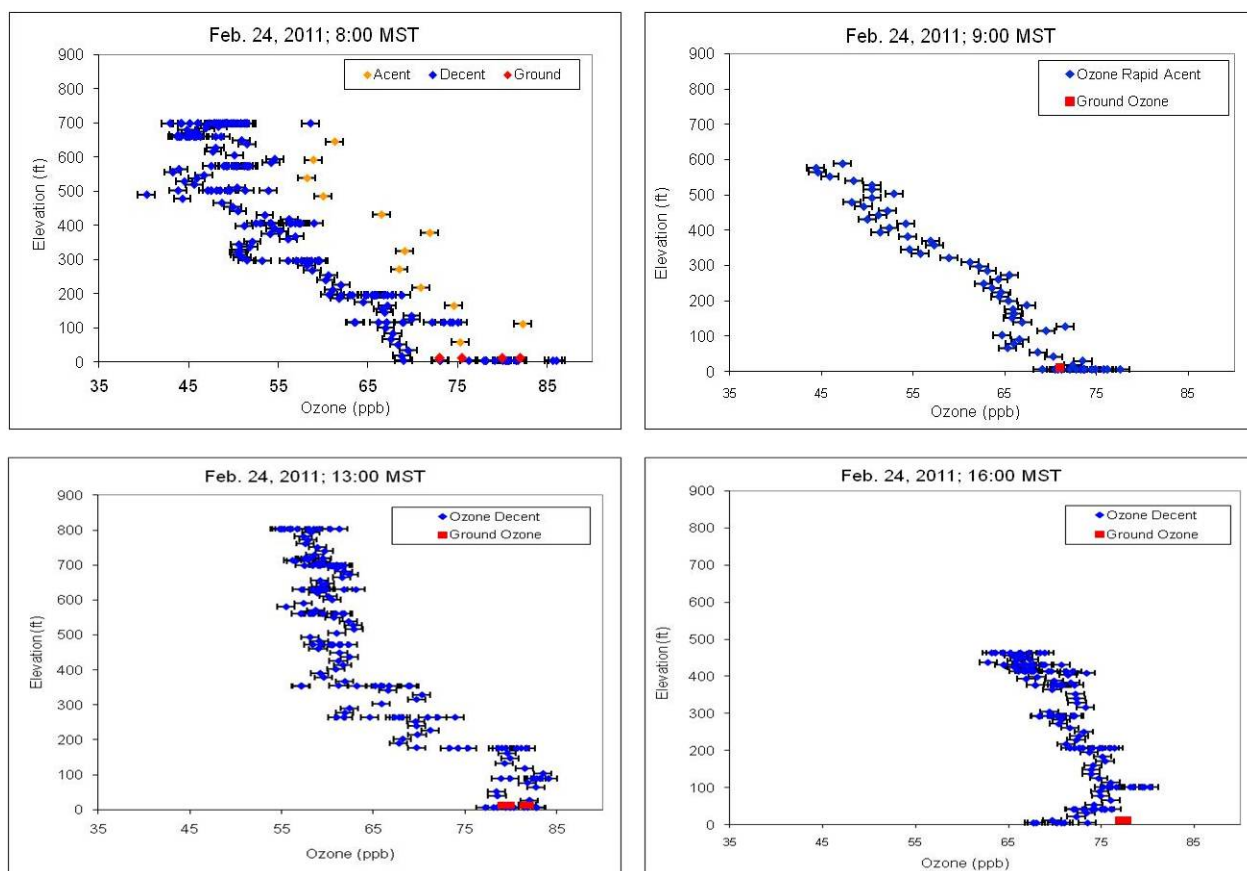
Figure 4-37. Red Wash tethered balloon vertical ozone profiles from Feb. 24, 2011.

The higher ozone concentrations observed at the surface are suggestive of local or near-area precursor emissions and ozone generation, as opposed to long-range transportation. Additionally, the higher elevation (≥ 500 ft agl) ozone concentrations tended to equilibrate around 45-50 ppb. These concentrations are approximately equivalent to the average values observed at the Fruitland location, which was hypothesized to essentially represent free tropospheric (background) ozone concentrations. Fig. 4-38 compares one of the Red Wash site's ozone profiles to a similar measurement in Utah's Cache Valley one week later, but under similar meteorological conditions. As is shown, the higher ozone values for the Cache Valley were observed at the upper elevations, basically opposite of the situation observed at the Red

---

Wash site. It should be noted that the Cache Valley has not observed any wintertime ozone exceedances, but the area is an officially declared nonattainment area for another secondary pollutant, $PM_{2.5}$, partially driven by reaction with ozone and other photochemical oxidants.
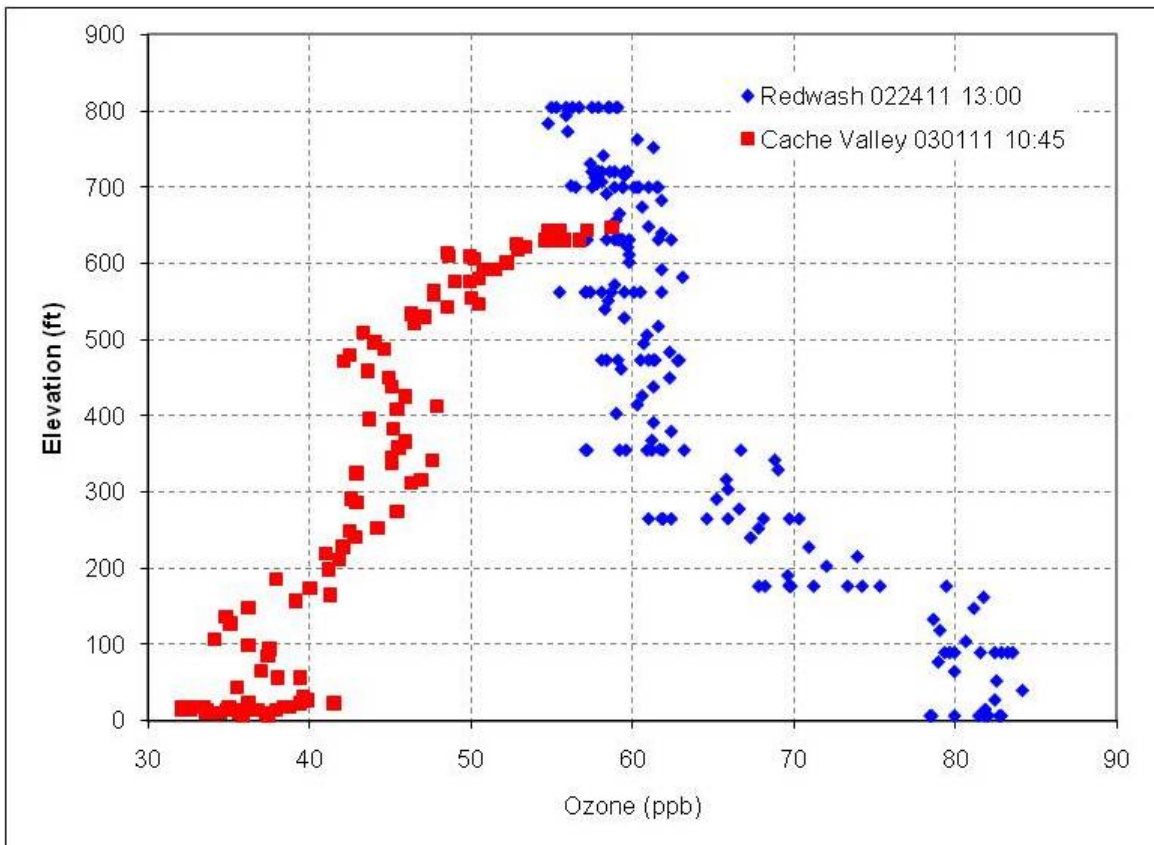
Figure 4-38. Comparison of wintertime vertical ozone profiles for Uinta Basin (Red Wash) and Cache Valley.

4.4 OXIDES OF NITROGEN

Ambient oxides of nitrogen (NO_x) are generally presumed to be the sum of gas-phase nitric oxide (NO) and nitrogen dioxide (NO_2). In anthropogenically impacted areas, NO is typically produced as an unwanted by-product of combustion and often is, therefore, a convenient marker compound for automotive and other combustion exhausts. Once emitted into the atmosphere, NO may be converted to NO_2 by oxidants such as ozone. Air masses dominated by NO (relative to NO_2) are usually considered to be a "fresh" plume, while those dominated more by NO_2 (relative to NO) are considered to be more "aged," or in the presence of a more oxidizing atmosphere (i.e., plentiful in oxidizing compounds). Additionally, NO_2 is a key component in the formation of ozone. It also undergoes photolysis to produce free atomic oxygen, which then readily combines with diatomic oxygen to form ozone.

The observed ambient concentrations of NO_x were typical of semi-urban and rural areas. The time series for NO_x at the Vernal and Red Wash sites, as well as additional data for the Ouray location, are shown in Figures 4-39, 4-40, and 4-41, respectively. Data from the latter two sites were supplied by Golder Associates. The NO_x concentrations originally were planned to be

monitored only during the intensive study period (Feb. 21-25, 2011); however, additional data were also collected through the middle of Mar. 2011.
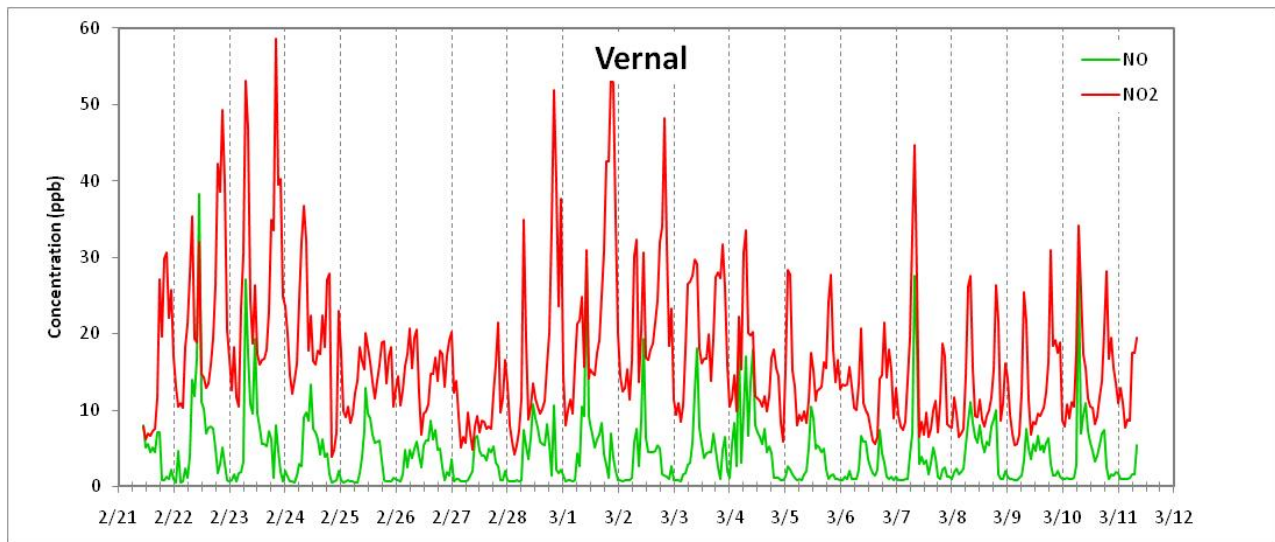
Figure 4-39. Time series of ambient NO and NO_2 as measured at the Vernal sample site from Feb. 21 to Mar. 11, 2011.
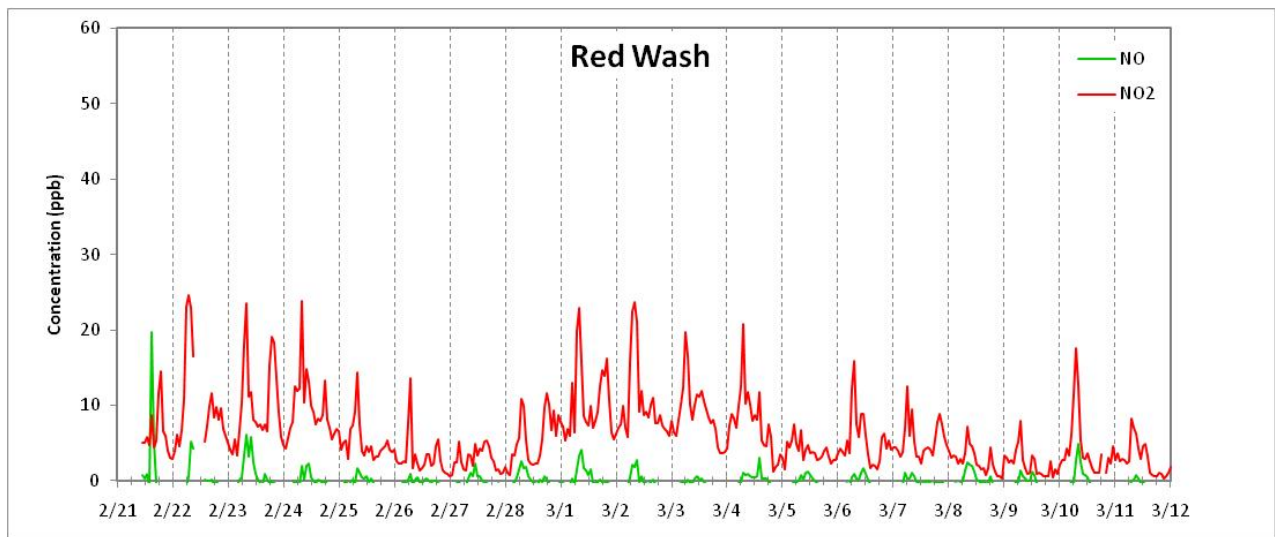
Figure 4-40. Time series of ambient NO and NO_2 as measured at the Red Wash sample site from Feb. 21 to Mar. 11, 2011. Data supplied by Golder Associates.
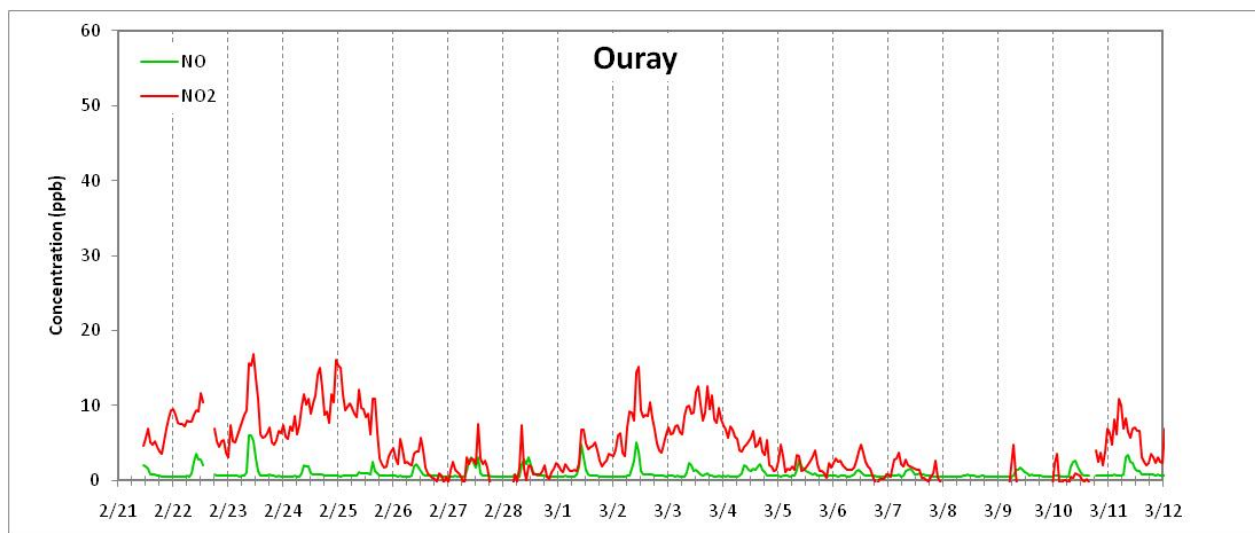
Figure 4-41. Time series of ambient NO and NO$_2$ as measured at the Ouray sample site from Feb. 21 to Mar. 11, 2011. Data supplied by Golder Associates.

As shown in Figures 4-39, 4-40, and 4-41, during the observed period, the Vernal location was found to have the highest concentrations of both NO and NO$_2$ among the observed locations. Vernal's hourly averaged concentrations of NO$_2$ approached as much as 60 ppb on several occasions which were coincident with elevated ozone and observed inversion conditions (see Fig. 4-39). For comparison, oxides of nitrogen, which are regulated as only NO$_2$, has a NAAQS hourly standard of 100 ppb, regulated at the 98th percentile. All observed NO$_2$ concentrations were well below the allowable standard. The NO concentrations observed at Vernal were approximately half of those of NO$_2$, suggesting the observed air mass was an aged plume or in the presence of abundant oxidizing species (i.e., ozone). Maximum NO$_2$ concentrations measured at the Red Wash and Ouray locations approached 25 and 15 ppb, respectively (see Figures 4-40 and 4-41).

Close examination of Fig. 4-39 through Fig. 4-41 shows various concentration spikes in the NO$_2$ and NO at different times on a given day. Calculating the hourly average NO$_2$ and NO concentrations for the February 21-25, 2011 period resulted in the diurnal curves shown in Fig. 4-42 through Fig. 4-44. As can be seen, the Vernal concentration spikes are much more pronounced and demonstrate chronological patterns expected when urban traffic is the assumed dominant source of NO$_x$ compounds. As the monitoring distance from potential immediate sources of NO$_x$ was increased, the observed concentrations and diurnal magnitude changes decreased. For example, NO$_x$ concentrations at the Red Wash site, which is adjacent to Utah State Highway 45, still displayed morning and evening traffic-related NO$_x$ spikes. On the other hand, measurements from the Ouray site, centrally located in the oil and gas fields, reveal much more damped diurnal NO$_x$.

It is also worth noting that comparison of the average NO$_x$ diurnal profiles shown in Figures 4-39, 4-40, and 4-41 with the previously discussed corresponding ozone diurnal profiles, shows that when the NO begins to increase in the early morning hours, the background ozone is quickly titrated (decreased), converting the NO into NO$_2$. Furthermore, as the daily sunlight increases,

NO_2 and VOCs are photolyzed to form ozone and other products; later, the evening NO_x peaks are paralleled by an ozone decrease.
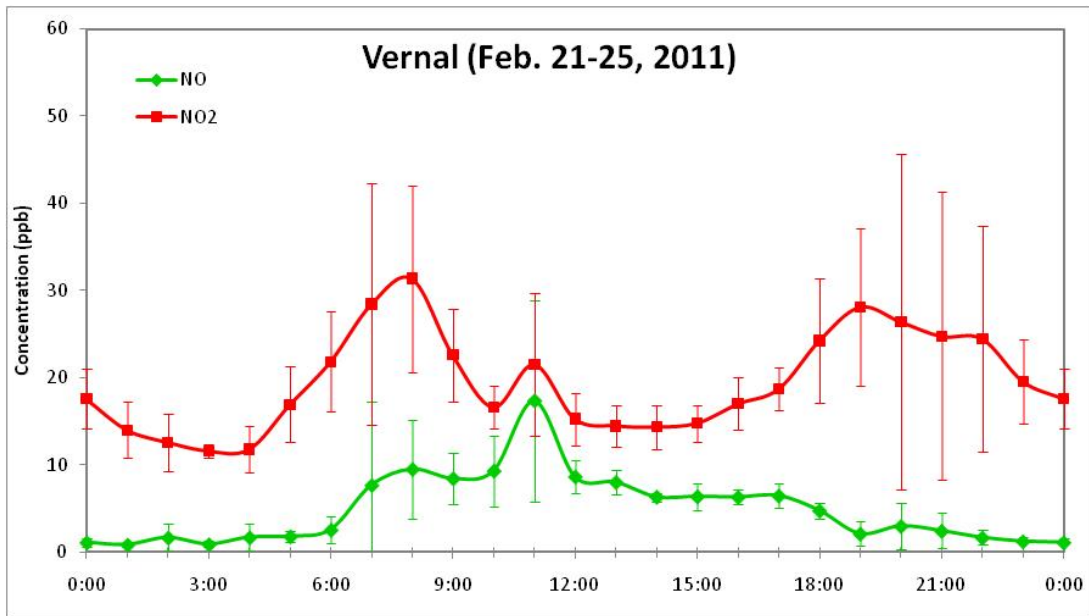
Figure 4-42. Vernal average diurnal NO_2 and NO for Feb. 21-25, 2011.
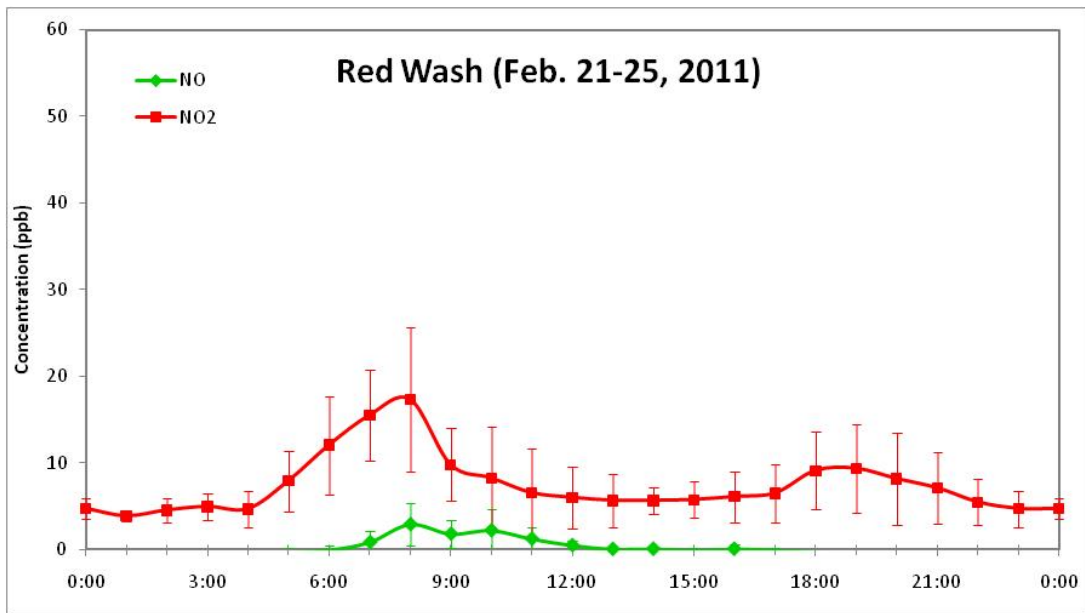
Figure 4-43. Red Wash average diurnal NO_2 and NO for Feb. 21–25, 2011.
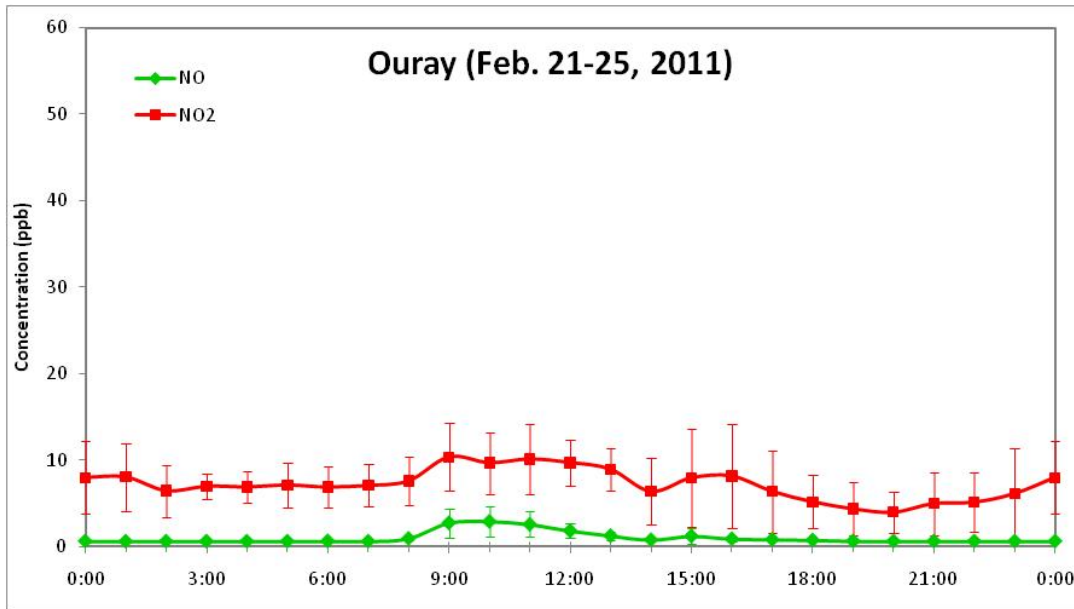
Figure 4-44. Ouray average diurnal NO$_2$ and NO for February 21-25, 2011.

4.5   HYDROCARBONS (INCLUDING CH$_4$)

Ambient methane (CH$_4$) and speciated non-methane hydrocarbons (NMHCs) were characterized at various daytime periods throughout the intensive sampling period of February 21-25, 2011. Methane is not normally considered a tropospherically-reactive hydrocarbon; however, CH$_4$ was added to the sampling scheme in response to research conducted in Pinedale, Wyoming, that revealed CH$_4$ to exist in concentrations where its reactivity became important. The NMHCs were collected over an integrated time period of approximately one hour, and grab samples were collected for CH$_4$ at the start and end of each NMHC sample period.

The average CH$_4$ concentrations, along with the 95% confidence intervals are shown in Fig. 4-45. As can be seen, the Vernal site CH$_4$ averaged 1.76 ± 0.24 ppm and the Red Wash site CH$_4$ averaged 2.78 ± 0.64 ppm. The 95% confidence intervals suggest statistically different concentrations at the two locations. Furthermore, it should be noted that the CH$_4$ concentrations ranged from 0.5 to 2.3 ppm at Vernal and 1.7 to 5.5 ppm at the Red Wash site. Oil and gas well exploration and production is a well-known source for potential CH$_4$ emissions during various process activities. This was consistent with the observed ambient concentrations that were significantly higher in the oil/gas field (Red Wash) than in the semi-urban (Vernal) area. For comparison, background northern hemispheric CH$_4$ is usually taken to be 1.6 – 1.7 ppm. Personal discussions with the other investigators suggest that the Red Wash site values are on the same level as those reported in Wyoming's Pinedale area.

As described in the "Methodologies" section, the analyses for the non-methane hydrocarbons was performed from collocated parallel sorption tubes: one nominally collected for light NMHC analysis (approximately C2 to C6) and the other for heavy NMHC analysis (C6 to C12). In the few cases where the GC analysis overlapped (e.g., benzene and a few other similar chain NMHCs), the analyses were averaged.
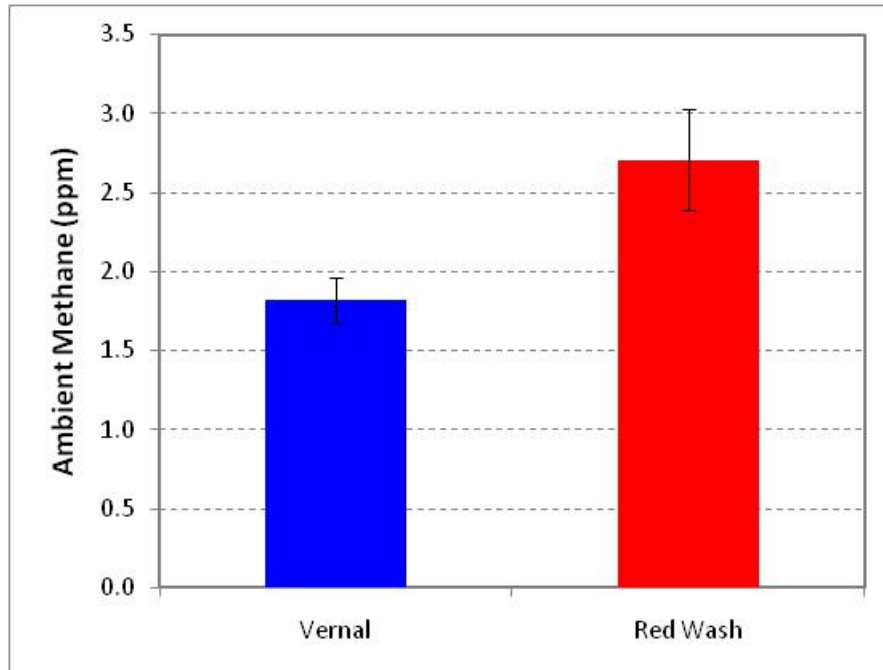
Figure 4-45. Average ambient methane for Vernal and Red Wash observed from instantaneous grab samples on February 21 through February 25, 2011. The error bars represent the 95% confidence interval about the average.

Between the light and heavy VOC gas chromatography analyses, attempts were made to quantify the 56 different compounds which are typically believed to be representative of ozone precursor species. The compiled averaged NMHC concentrations are shown in Table 4-3. It should also be noted that CH_4 has also been included, and its concentrations have been converted to parts per billion (from parts per million) for direct comparison with the other hydrocarbon compounds.

Initial examination of the species in Table 4-3 shows most of the targeted compounds were observed at sub-ppb concentrations. Furthermore, it can be seen that the concentrations of the identified VOC concentrations were greater at the Red Wash site by more than a factor of two for most of the observed compounds.

Table 4-3. Average reactive hydrocarbons measured at the Red Wash and Vernal sampling locations, February 21-25, 2011. The uncertainty represents the 95% confidence interval about the mean.

Compound	Red Wash (ppb)	Vernal (ppb)	Compound	Red Wash (ppb)	Vernal (ppb)
Methane	2780 ± 679	1764 ± 244	2,3-dimethyl pentane	0.09 ± 0.05	0.29 ± 0.13
Ethane	125 ± 35	119 ± 30	3-methyl hexane	0.26 ± 0.15	0.28 ± 0.19
Ethene	51.1 ± 93.0	6.1 ± 2.7	2-methyl hexane	0.15 ± 0.11	0.24 ± 0.11
Propane	20.9 ± 10.9	11.5 ± 8.0	n-heptane	0.51 ± 0.31	0.87 ± 0.49
Propene	0.78 ± 0.34	0.76 ± 0.24	Benzene	0.62 ± 0.22	0.32 ± 0.14
isobutane	5.23 ± 2.95	1.68 ± 2.17	2,2,4-trimethyl pentane	0.03 ± 0.04	0.02 ± 0.02
Acetylene	57.7 ± 111.0	2.07 ± 1.21	2-methyl heptane	0.39 ± 0.17	0.01 ± 0.02
Butane	8.74 ± 4.82	2.21 ± 3.86	3-methyl heptane	0.27 ± 0.14	n.d
trans-2-butene	0.09 ± 0.04	0.05 ± 0.03	Toluene	1.49 ± 0.70	0.05 ± 0.02
1-butene	0.18 ± 0.04	0.16 ± 0.03	n-Octane	0.81 ± 0.41	n.d
cis-2-butene	0.07 ± 0.03	0.04 ± 0.03	Ethylbenzene	0.11 ± 0.07	n.d
cyclopentane	0.28 ± 0.16	0.07 ± 0.10	m,p-xylene	0.33 ± 0.19	n.d
2-methylbutane	4.33 ± 2.60	0.97 ± 1.41	Nonane	0.35 ± 0.13	n.d
Pentane	4.34 ± 2.57	0.91 ± 1.70	Styrene	0.08 ± 0.12	0.07 ± 0.06
trans-2-pentene	0.01 ± 0.02	0.01 ± 0.02	o-xylene	0.15 ± 0.10	n.d
1-pentene	0.02 ± 0.02	0.01 ± 0.02	isopropyl benzene	0.02 ± 0.02	n.d
cis-2-pentene	n.d.	n.d.	n-propyl benzene	0.08 ± 0.04	n.d
methyl cyclopentane	0.54 ± 0.32	0.45 ± 0.23	m-ethyl toluene	0.09 ± 0.10	0.01 ± 0.02
2,2-dimethyl butane	0.16 ± 0.10	0.09 ± 0.05	p-ethyl toluene	0.05 ± 0.05	0.01 ± 0.01
cyclohexane	0.52 ± 0.33	0.48 ± 0.24	1,3,5-trimethyl benzene	0.05 ± 0.04	n.d
2,3-dimethyl butane	0.17 ± 0.12	0.03 ± 0.06	n-decane	0.22 ± 0.11	0.02 ± 0.04
2-methyl pentane	1.69 ± 1.02	0.34 ± 0.67	o-ethyl toluene	0.06 ± 0.04	n.d
3-methyl pentane	0.82 ± 0.50	0.16 ± 0.31	1,2,4-trimethyl benzene	0.18 ± 0.16	n.d
isoprene	2.91 ± 1.10	0.46 ± 0.90	1,2,3-trimethyl benzene	0.08 ± 0.05	0.01 ± 0.01
n-hexane	0.07 ± 0.03	1.13 ± 0.65	m-diethyl benzene	0.04 ± 0.04	n.d
1-hexene	0.03 ± 0.03	0.02 ± 0.02	p-diethyl benzene	0.07 ± 0.06	0.01 ± 0.01
2,4-dimethyl pentane	0.06 ± 0.05	0.05 ± 0.03	n-undecane	0.42 ± 0.19	0.71 ± 1.02
methyl cyclohexane	0.65 ± 0.43	0.39 ± 0.27	n-dodecane	0.61 ± 0.38	0.84 ± 0.81

n.d. = non-detect

Besides methane, the final report "Oil and Gas Emission Inventories for the Western States" (WRAP, 2005) states that benzene, toluene, and the combined xylene compounds are all key VOCs associated with oil and gas exploration and production operations. As can be seen in Table 4-3, at the Red Wash location the average concentrations for benzene, toluene, and m,p-xylene were 0.62 ± 0.22 ppb, 1.49 ± 0.70 ppb, and 0.33 ± 0.19 ppb, respectively. The concentrations observed at the Vernal location for the same compounds were 0.32 ± 0.14 ppb, 0.05 ± 0.02 ppb, and non-detectable, respectively. It should also be pointed out that these same species are also representative of automotive emissions, and the ratio of benzene-to-toluene (B/T) is often used as an indicator of the age of the air mass. As listed in many atmospheric chemistry reference texts, a B/T ratio≈0.4 is usually considered to be evident of fresh vehicular emissions. Benzene-to-toluene ratios >0.4 are presumed to represent an aged air mass, since toluene has a much higher atmospheric reactivity rate than does benzene. The observed B/T ratios from this study were 0.43 and 6.03 for Red Wash and Vernal locations, respectively. The Vernal B/T ratio may be somewhat anomalous due to the very low average concentration observed for toluene (0.05 ppb).

However, the 2005 WRAP document suggests the B/T ratio from oil and gas field operations should range between 0.43 and much greater than one, depending on the process examined. For

example, dehydration/evaporation, storage tanks, and general well operations are estimated to show B/T ratios of 0.433, 0.77, and 31.5-39.5, respectively. In summary, it is reasonable to assume that the abundance of CH_4 and NMHCs observed at the Red Wash site, located on the edge of a dense well field, is a result of the oil and gas exploration and production activities

4.6 PARTICULATE MATTER LESS THAN 2.5 μm (PM$_{2.5}$)

During the intensive sampling period (Feb. 21-25, 2011), four 23-hr PM$_{2.5}$ daily composite samples were collected at the Vernal and Red Wash locations (see Fig. 4-46). The error bars shown represent the 95% confidence interval about the mean of three collocated TFE-filter based MiniVol PM$_{2.5}$ measurements (refer to "Methodologies" discussion). Historical PM$_{2.5}$ measurements in the Vernal area by the Utah Division of Air Quality (UDAQ) have shown some exceedances of the current PM$_{2.5}$ national standard (>35 µg/m^3). The concentrations during this study period were well below the allowable limits. Furthermore, Fig. 4-46 shows that a collocated, continuous, near real-time (E-BAM) PM$_{2.5}$ analyzer operated by an external operator (Golder Associates) found very similar concentrations at the Red Wash site
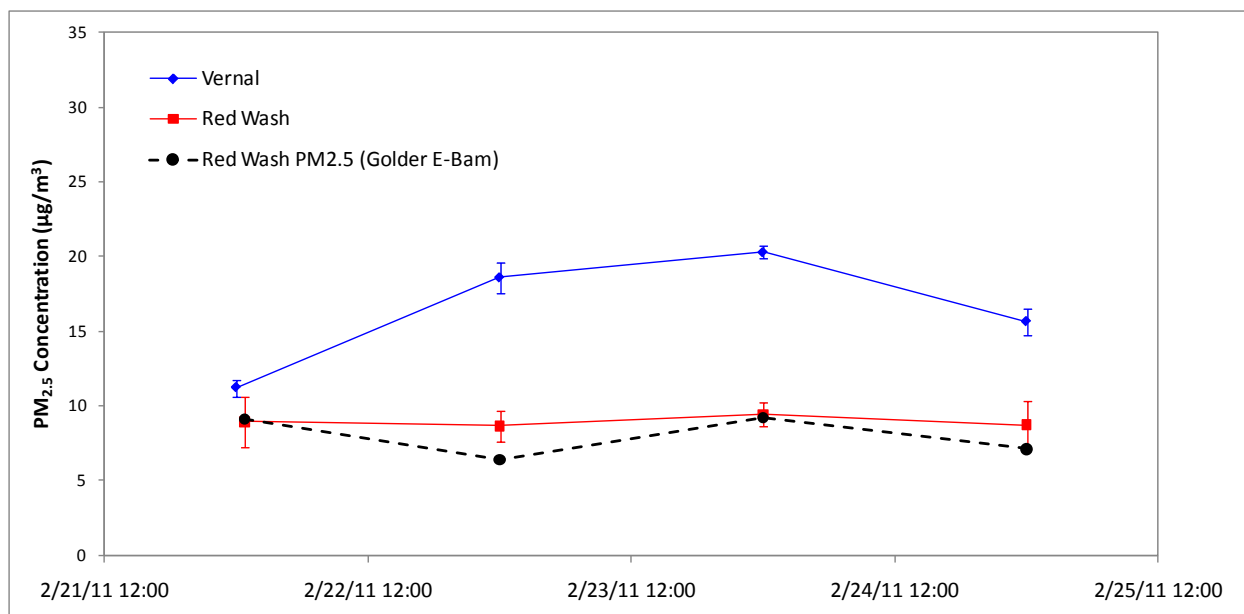
Figure 4-46. Average daily PM$_{2.5}$ at the Vernal and Red Wash sites during late Feb. 2011. The dashed line and associated symbols represent the average values reported by a collocated E-Bam operated by Golder Associates.

Chemical speciation of the collected PM$_{2.5}$ was also determined via multiple methodologies, and these composite analyses are shown in Fig. 4-47. Both sites were dominated by particle-bound carbon, accounting for around 80% of the PM$_{2.5}$ mass. This contrasts with what is observed in other areas of Utah, especially the Wasatch Front and Cache Valley, where the ionic components, most notably ammonium (NH_4^+) and nitrate (NO_3^-), often account for mass percentages similar to that of the carbon component in the Uinta Basin PM$_{2.5}$. The abundance of carbon material suggests either strong local or regional direct sources of primary carbonaceous particles or local/regional formation of photochemical secondary organic aerosols (SOAs). Either scenario adds weight to the likelihood of strong regional contributions of the oil and gas industry to the atmospheric hydrocarbon (VOC) burden of the Uinta Basin's airshed.
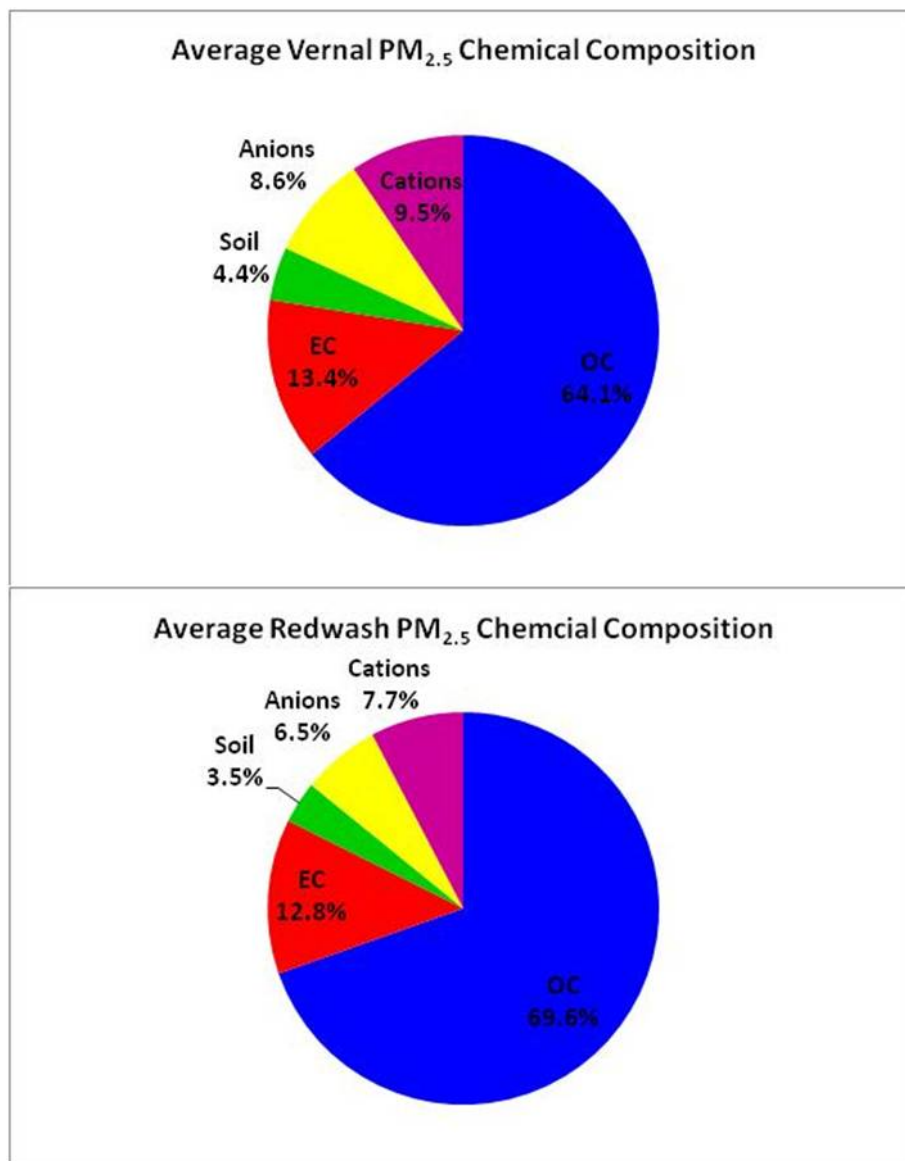
Figure 4-47. Average composite chemical composition of the collected PM2.5 for the Vernal and Red Wash sites during the Feb. 21-25, 2011 sampling period.

4.7 METEOROLOGY (INCLUDING VERTICAL PROFILES)

4.7.1 Vertical Meteorology

Vertical meteorological parameters were successfully characterized at the Red Wash site during four days in late February 2011; a low pressure system with accompanying clouds and precipitation prevented further tethersonde data collection at the end of the test period. Post analyses of the data were performed to determine the above ground level height of the tethersonde package, the stability of the atmosphere, and the depth of the surface layer, all based on measured ambient temperature, pressure, humidity, wind speed, and wind direction. Examples of the collected and calculated data used to determine both the stability of the atmosphere and the depth of the surface layer are shown in Figures 4-48 and 4-49. These figures are from an early

morning and a mid-afternoon profile, the times of day when the surface layer is usually at its lowest and highest levels, respectively.

The potential temperature profiles, calculated from actual temperature profiles with nearly identical trends, show warming temperatures with increasing altitude (i.e., a temperature inversion). Strong temperature inversions were detected during each profile measurement and extended from the ground to beyond the 250-350 m reach of the tethersonde system. Temperature inversions prohibit vertical mixing in the atmosphere, resulting in very stable conditions wherein emitted pollutants remain near the same level as their source. Measured wind speeds throughout the experiment were generally light (< 2 m/s) from the surface up to more than 200 meters. The observed calm/low wind conditions, combined with the strong, persistent temperature inversion, suggest that very little vertical mixing occurred and horizontal movement was limited within the Basin during this measurement period. This combination of surface and vertical meteorology measured during elevated ozone concentrations supports the hypothesis that local sources and their strengths are more influential in determining ozone concentrations than long distance sources or other influences from external airsheds.

The mean value of the surface layer depths estimated during both the ascent and descent of the tethersonde balloon is shown by the dotted lines in Figures 4-48 and 4-49. Note that while the surface layer in the afternoon is higher than in the morning, the level of the surface layer is still below 100 meters. This pattern was seen throughout the experiment, as shown in Fig. 4-50, with extremely shallow surface layer depths at 20-80 m. Such shallow surface layers during the afternoon are indicative of a stable atmosphere with very limited vertical mixing. Vertical wind speed measurements made at the permanent monitoring station at Red Wash (Golder Associates) indicate very little vertical movement from Feb. 21-24, 2011. It should be noted that the Red Wash site was located near the top of a ridge, which may have been near the top or above the winter-time inversion depth in the Uinta and Ashley river valleys, which is supported by personnel observations throughout each day.

Technical and instrumentation problems at the Jensen site prevented the calculation of surface layer depths and, for the most part, the extraction of useful data. However, collected wind speed data throughout the deployment were considered valid. A representative example of the wind speed profiles seen at the Jensen site is shown in Fig. 4-51 for the morning and late afternoon/evening period on Feb. 22, 2011. Wind speeds throughout the measurement period were below 3 m/s at all times. A diurnal pattern was found where calm conditions existed throughout the profile during the mornings and evenings, with low winds present at most altitudes during midday and in the afternoon.
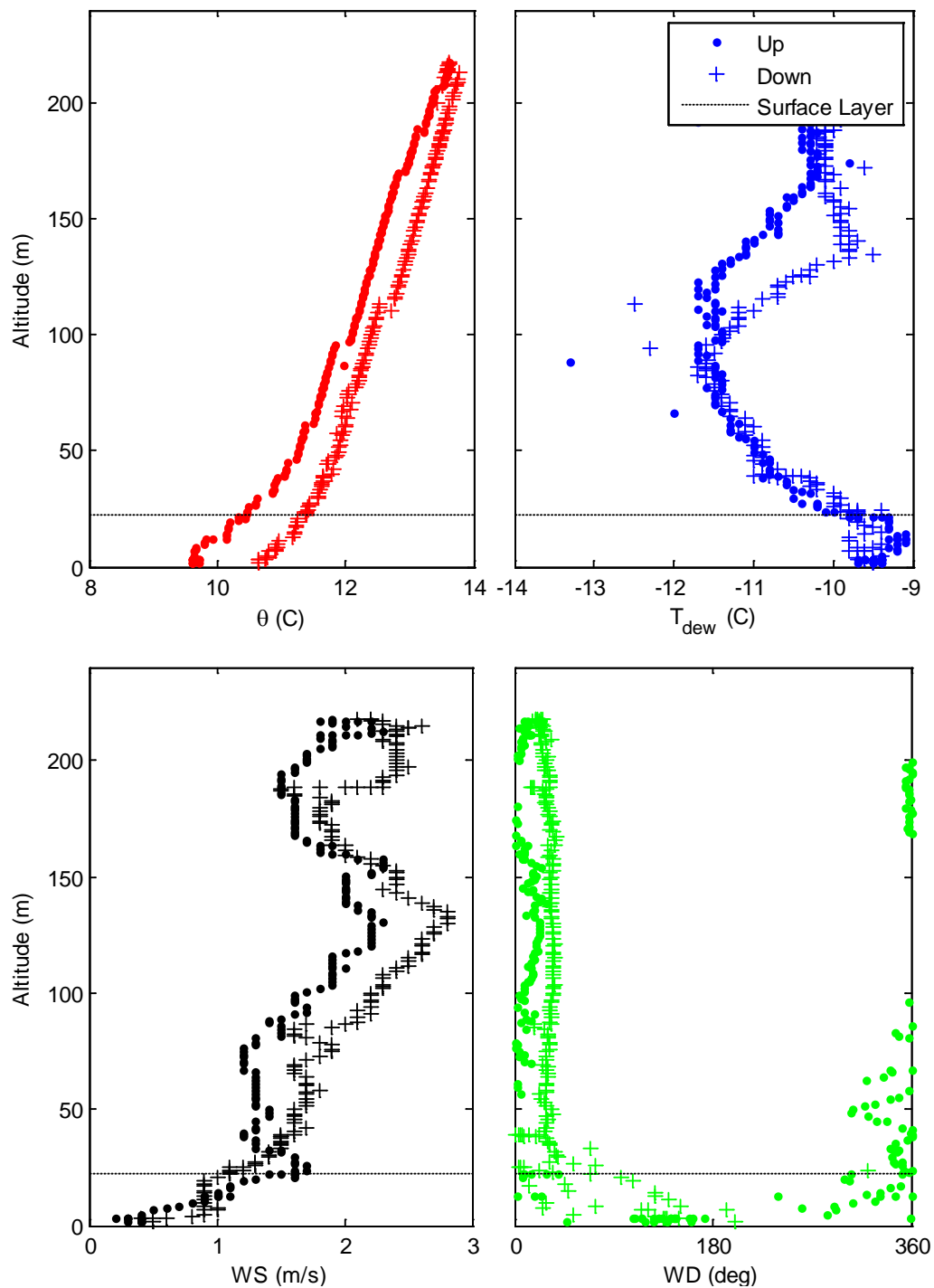
Figure 4-48. Vertical profiles of potential temperature (θ), dewpoint temperature (Tdew), wind speed (WS), and wind direction (WD) for February 22, 2011 around 08:00 hours.
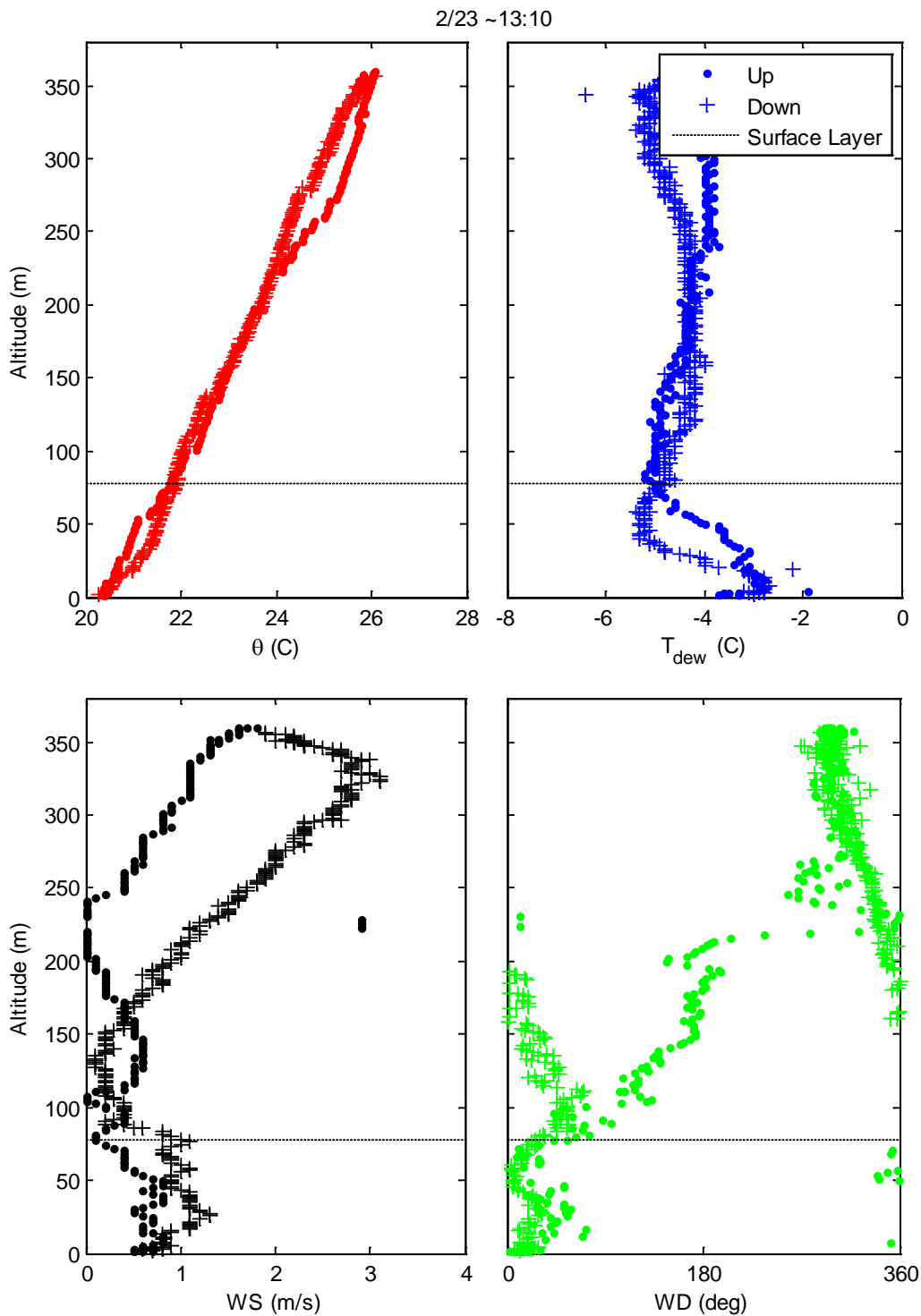
Figure 4-49. Vertical profiles of potential temperature (θ), dewpoint temperature (T_dew), wind speed (WS), and wind direction (WD) for February 23, 2011 around 13:00 hours.
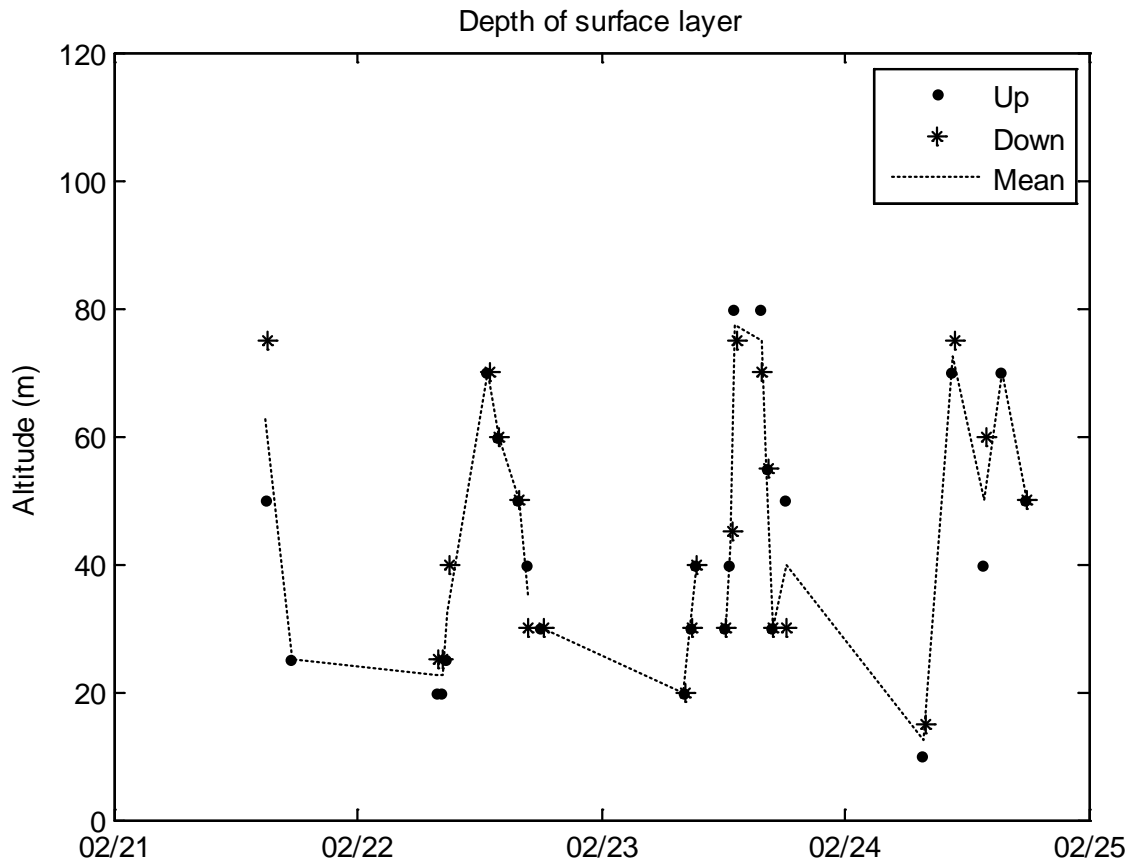
Fig. 4-50. Graphical representation of the depth of the surface layer determined for each vertical profile through examination of the collected and calculated data at the Red Wash location.
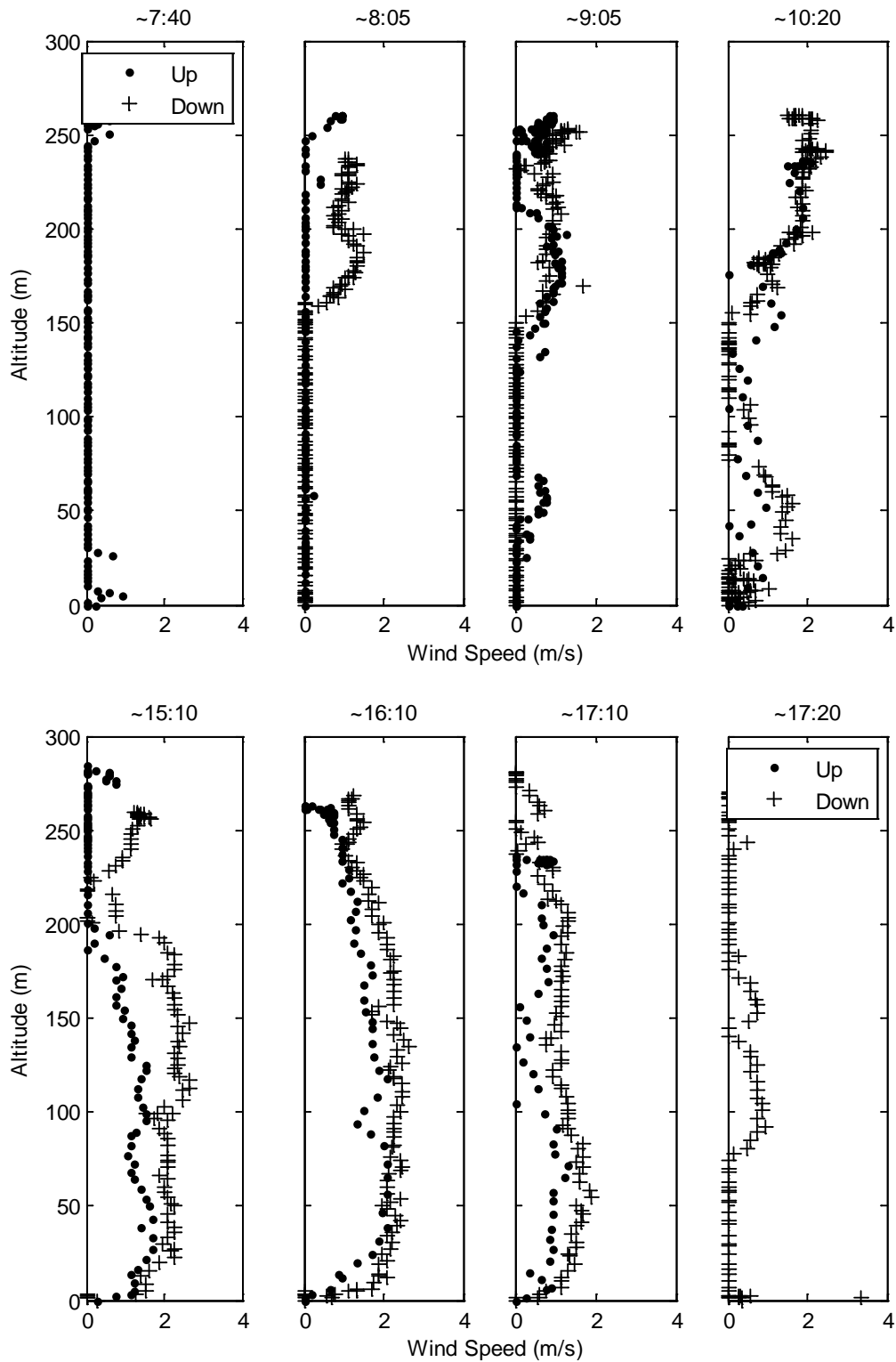
Figure 4-51. Wind speed versus altitude as measured during the morning and late afternoon at the Jensen site on Feb. 22, 2011.

4.8   HORIZONTAL METEOROLOGY

Meteorological stations spread throughout the Uinta Basin that measure, at a minimum, temperature, wind speed, and wind direction, were identified and data were gathered for the December 15, 2010 to March 15, 2011 time period. Data sources include Golder Associates, NPS, UDAQ/BLM, and Mesowest. Wind data were compiled and used to create windroses for periods of interest, as shown in Fig. 4-52, for the months of January and February 2011 for the (a) Fruitland, (b) Rangely, (c) Ouray, and (d) Dinosaur National Monument monitoring sites. Windroses are useful graphical representations of wind data because they can show the relative amount of time the wind _comes from_ a given direction and the wind speed values measured from that direction.

In Fig. 4-52, the Fruitland data show that winds almost exclusively come from the west or northwest directions and tend to have wind speeds greater than 2 m/s. The Rangely data show that winds usually originate from the east and west with most winds less than 2 m/s. The winds at Ouray are more evenly spread from all directions and almost always have low speeds. Winds measured at Dinosaur National Monument are dominantly from the southwest direction and exclusively have wind speeds below 2 m/s. One parameter that is not represented in the graph is the number of calm hours, or hours with an average wind speed below 0.5 m/s. Calm hours accounted for 48.6% of the total hours at Dinosaur National Monument, 13.4% at Ouray, 3.9% at Rangely, and 0.2% at Fruitland.

A collection of spatially separated windroses, such as that shown in in Fig. 4-52, can be more easily understood when overlaid onto a surface map of the area of interest. Figures 4-53 and 4-54 show windroses for wind measurements from several meteorological stations located throughout the Basin for the February 2-6, 2011 and February 12-16, 2011 periods. The February 12-16, 2011 period was chosen as representative of stagnant meteorology and high pollution episodes, while the February 2-6, 2011 period was a period of dynamic meteorology and low ozone levels between strong storms. The compass grids were removed to allow map details to be seen, but all windroses used equal scales with the maximum percentage of a single bar being about 25% at the Diamond Rim and Five Mile stations on the February 12-16, 2011 map in Fig. 4-54. As can be seen from these figures, the stations at higher elevations surrounding the Basin, such as Dragon Road, Diamond Rim, Five Mile, and Upper Sand Wash recorded similar wind patterns that are very different from those measured within the valley regions of the Basin. The strong differences for both periods in the winds measured within the valley regions and at higher elevations on the edges of the Basin show that the valley is isolated from the regional air mass movement. The low wind speed dominance within the valley demonstrates the stagnant nature in the surface layer under the strong temperature inversions.
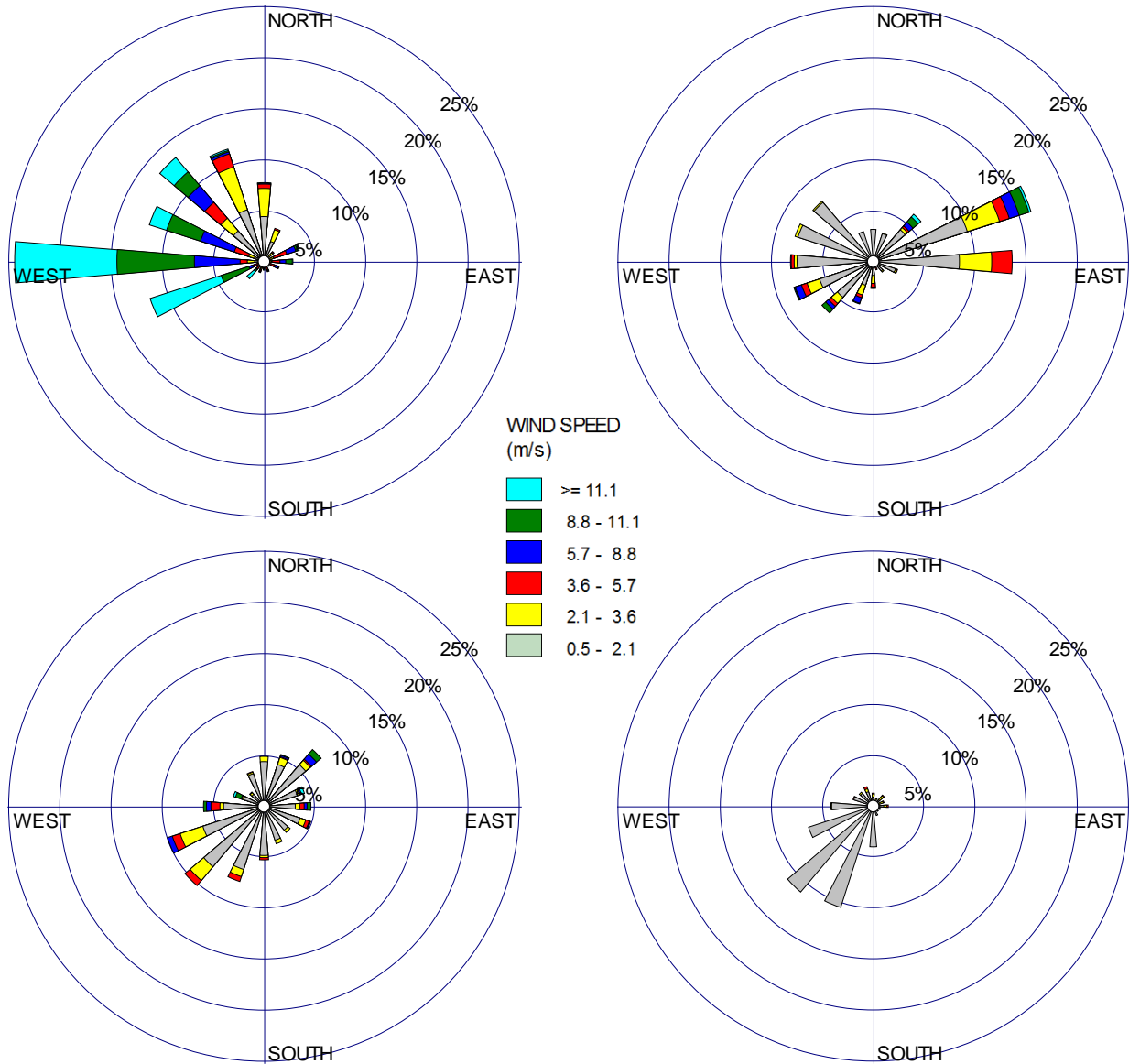
Figure 4-52. Windroses created for (a) Fruitland, (b) Rangely, (c) Ouray, and (d) Dinosaur National Monument monitoring locations for the Jan. 1 - Feb. 28, 2011 period. Calm hours were 0.2% for Fruitland, 3.9% for Rangely, 13.4% for Ouray, and 48.6% for Dinosaur National Monument.
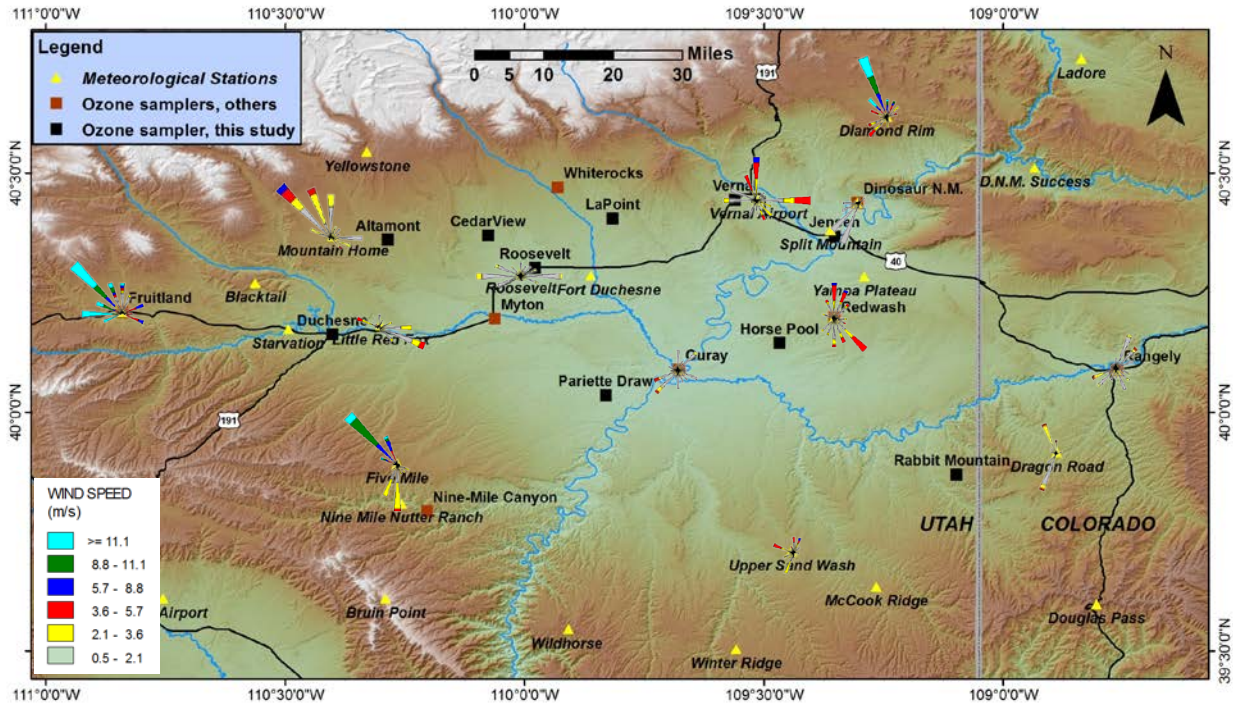
Figure 4-53. Spatially located windroses for the Feb. 2-6, 2011 period overlaid on a map of the Basin. For scale, Five Mile winds came from the northwest approximately 15% of the time.
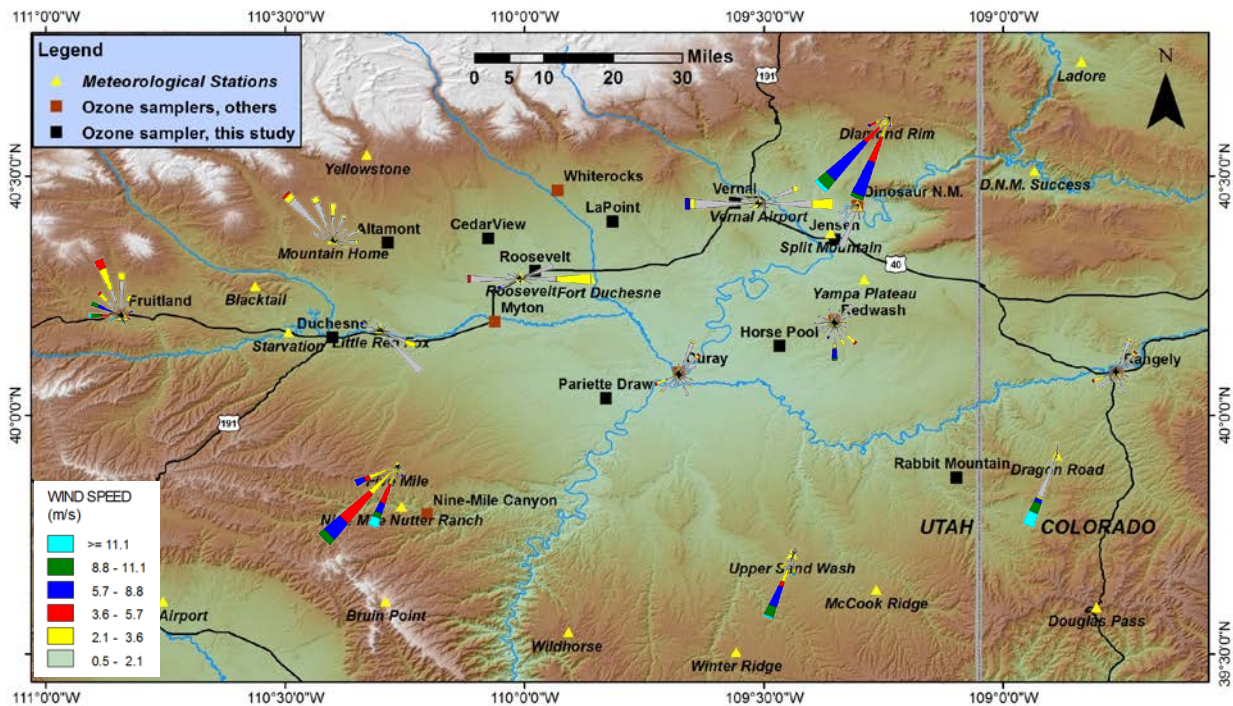
Fig. 4-54. Spatially located windroses for the Feb. 12-16, 2011 period overlaid on a map of the Basin. For scale, Diamond Rim winds came from the southwest approximately 25% of the time.

5.   OZONE MODELING

5.1   INTRODUCTION

Computer models of atmospheric ozone require two interacting components: airflow and chemistry. The airflow component is required to predict how a pollutant moves about and is dispersed. The chemistry component is necessary because concentrations rise and fall as ozone is generated and consumed by chemical reactions. There are, however, some models that neglect airflow and focus on chemistry. These "box models" examine the chemical reactions occurring in a column, or "box," of air, and may also include provisions for chemical constituents entering and leaving the box through its boundaries. Box models are directly applicable to laboratory smog chamber experiments, and they can also be used to model processes in flowing air, under the assumption that the box represents a column of air moving with the ambient flow. Furthermore, box models are applicable to most ozone events, including those in the Uinta Basin, because such events occur during thermal inversions when the air is stagnant and the constituents are relatively homogeneous within the inverted layer. Given the preliminary, short-term nature of the present study, it was decided to focus on box modeling, and, in particular, on ozone chemistry at lower, wintertime temperatures. Most of our studies employed OZIPR, the EPA-approved box-model system.

Because of its low stability and high reactivity (it reacts with practically any other molecule), ozone is considered "promiscuous," and since it is hazardous at low concentrations, effective chemical modeling requires that we consider ozone's reactions even with trace gases in the atmosphere. Needless to say, atmospheric ozone chemistry is extremely complex. At the core of any chemical model of ozone production is the "mechanism," which, in the present context, consists of three components: (1) the chemical species considered by the model, (2) the chemical reactions by which the chemical species interact, and (3) a specification of the kinetic rate laws or mathematical formulas required for calculating the rate of each reaction. The rate of a given reaction depends on the concentrations of reacting species, temperature, pressure, and, for photochemical reactions, on the actinic flux (total available solar radiation). All of these dependencies are included in the reaction rate expression. There are several different "state-of-the-art" mechanisms employed in contemporary ozone models, including CB05, SAPRC, RADM, and Morphecule (Gery et al., 1989; Dodge 2000; Yarwood et al., 2005; Sarwar et al. 2008; Carter 2010). CB05 incorporates about 50 chemical species and 160 reactions, and many of these are "lumped" species or reactions, meaning that similar compounds have been grouped together to simplify the mechanism. SAPRC defines over 100 species and over 250 reactions, again with lumping (Carter 2010). According to one estimate, a mechanism that did not resort to lumping would require several thousand species and around 20,000 reactions (Dodge 2000).

Reaction rate expressions must be determined empirically, and extensive measurements are required to completely specify dependence on concentration, temperature, pressure, and actinic flux. Needless to say, it is doubtful that measurements have been performed to determine the reaction rate expressions for all the 20,000 reactions mentioned above at the sub-zero temperatures at issue in the present study. It is likely that most measurements were performed near room temperature since no motive existed to consider ozone reactions at lower temperatures when convention viewed tropospheric ozone as a summertime problem.

Three concerns about CB05 or similar mechanisms at low temperatures will be listed in the following paragraphs. Our best estimate is that current predictions of winter ozone are probably about 10 ppb too high, but with an uncertainty (one standard deviation) of about 11 ppb. Mollner et al. (2010) discussed the significance of a 10 ppb modeling mistake. The motivation of this section is not to indict the researchers who studied these reactions or who assembled CB05 or any other mechanism. The reactions are complex, their rates are difficult to measure, and for obvious reasons such measurements have focused on summertime temperatures. Rather, our motivation is, first, to indicate the limitations of applying the current mechanisms to predictions of winter ozone; and, second, to specify areas for possible future research to improve predictive capabilities at low temperatures.

5.1.1   Concern I: Temperature dependence of photolytic reactions.

The CB05 mechanism neglects the temperature dependence of the more than 20 photolytic reactions in that mechanism (Tonnesen 2011). Based on explicit calculations for five different photolytic reactions, the rate of a photolytic reaction decreases by roughly 1% for every 5 K drop in temperature. This effect leads to a decrease of 5-10 ppb in the predicted ozone concentration at temperatures near -10°C.

5.1.2   Concern II: Negative empirical activation energies.

The empirical activation energies of about 45 reactions in CB05 are negative. The most likely explanation (Tonnesen, 2011) is that the true activation energy is positive but small in magnitude. A negative activation energy reflects temperature dependence of the pre-exponential factor. There is nothing inherently wrong with a negative activation energy if it provides a reasonable empirical fit to the data; however, an extrapolation to temperatures beyond the temperature range of the data used to develop the rate expression is suspicious. In "Reactions with Negative Activation Energies" below, a comparison is shown of a "power-Arrhenius" rate law (an Arrhenius form with a pre-exponential factor that is a power function of temperature with negative exponent) with a positive activation energy against an ordinary Arrhenius form with a negative activation energy. The two equations are respectively concave up and concave down, which means that they have fundamentally different extrapolation properties. Making this change with low temperature extrapolations leads to a decrease of about 0.5 to 1 ppb in the predicted ozone concentration near -10°C.

5.1.3   Concern III: Other reactions appearing without temperature dependence.

Apart from the photolytic reactions mentioned above, about 40 reactions appearing in CB05 are displayed without any temperature dependence. This *may* indicate that the reaction is independent of temperature; however, the more likely explanation is that the rate of the reaction has only been measured at one temperature. Monte Carlo calculations shown below in "Sensitivity of the Base Model to Adjustments in Reaction Rates" are based on the premise that any reaction appearing in CB05 without temperature dependence will actually follow an Arrhenius law whose activation energy is selected randomly from a spectrum representative of all tabulated activation energies in CB05. These calculations indicate that the most-probable value of predicted ozone drops by approximately 3 ppb, but there is an uncertainty on the order of about 11 ppb.

Of the 160 reactions occurring in CB05, about 110 fit into one of the three categories of concern discussed above. Of the remaining reactions, one (OH + NO$_2$ + M $\rightarrow$ HNO$_3$ + M, where M represents a generic air molecule) is particularly noteworthy. As a result of new, precise measurements, the rate of this reaction has recently been revised. The predicted ozone maximum turns out to be very sensitive to the rate of this reaction (see below), and the revision leads to an increase of 5-10 ppb in the predicted summertime ozone concentrations (Mollner et al., 2010). Unfortunately for our purposes, these new measurements were performed near room temperature, providing little guidance for adjusting the rate at low temperatures.

Fortunately, it is common practice to validate mechanisms against both field data and smog chamber measurements, and the results of such validations indicate that well-designed and properly-executed computer models are very useful tools (Dodge 2000). Low-temperature validations, however, are not available at present.

Two important caveats exist concerning computer modeling of winter ozone events. The first relates to the above discussion regarding deficiencies in applying the mechanisms at low-temperature: *None of the mechanisms has been adequately validated at low temperatures.* The second caveat relates to the fact that although VOCs in general play a role in ozone chemistry, each compound has its own reactivity: *Modeling results will be tentative until VOC speciation has been measured.* Because of several years' lead-time, VOC speciation in the Upper Green River Basin is better understood than in the Uinta Basin.

Dr. Gail Tonnesen, EPA District 8, supplied us with the computer code for OZIPR, a standard EPA-approved box-model software platform for modeling ozone events. This implementation of OZIPR utilizes the CB05 mechanism. Dr. Tonnesen also supplied a test case, including VOC speciation data, representing a typical late-winter ozone event (Feb. 20, 2008) in the UGRB (Tonnesen, 2011). The average temperature for this test case is –9°C = 264 K, and the ozone concentration rises from 24 ppb at dawn to a maximum of 122.5 ppb in the afternoon. It is noteworthy that the CB05 mechanism predicts a significant winter ozone event, but as already mentioned, we believe that the mechanism has not been adequately validated at low temperatures. The UGRB test case was used as a base model to investigate the applicability of CB05 to low temperatures (see below). Although we believe it is advisable to revise CB05 to reflect recent findings relative to the OH + NO$_2$ + M reaction (Mollner et al., 2010), such a revision was not done in the current study; rather, CB05 was used as it was delivered to us for the calculations discussed in this report.

An important consideration when adjusting reaction rates in a mechanism is the sensitivity of the base model to a change in any given reaction. A formal definition and discussion is given in the following section. In subsequent sections, we present calculations that estimate the effects of each of the three concerns mentioned above.

In the following sections, we define two scenario temperatures: T_h = 300 K = 27°C = 80.6°F (the "hot" temperature), typical of the temperatures for which CB05 was developed, and T_c = 264 K = –9°C = 15.8°F (the "cold" temperature), typical of the temperatures occurring during the winter ozone phenomenon. We also use a 'P' (with assorted subscripts and qualifiers to designate adjustments to the mechanism) to indicate the predicted ozone peak, or predicted daily maximum ozone concentration.

5.2 SENSITIVITY OF THE BASE MODEL TO ADJUSTMENTS IN REACTION RATES

For each one of the 160 reactions in the CB05 mechanism, simulations were performed in which individual reactions were artificially accelerated and decelerated, and the change in the predicted maximum ozone concentration was monitored. The simulations quantified the sensitivity, S_i, of the base model to the rate of reaction i. The 22 reactions with the highest sensitivities are shown in the Table 5-1. Each S_i has the units of concentration and is given in Table 5-1 in ppb units. The technical definition of S_i is given at the end of this section, but a simple example will illustrate its role: For every 1% increase in the rate of reaction i, the maximum ozone peak increases by 1% of S_i. A negative sensitivity designates that the ozone peak decreases rather than increases. The highest sensitivities are approximately ±60 ppb. There are many reactions for which the sensitivity is near 0. The column headed "Suspicious?" indicates whether the reaction belongs to one of the three categories mentioned above: P indicates a photolytic reaction, N indicates an Arrhenius law with negative activation energy, and C denotes a reaction appearing without temperature-dependence.

Table 5-1. The 22 reactions in CB05 with high sensitivities relative to the base model. See Sarwar, et al. (2008) for definitions of species' names.

Reaction	Suspicious?	S_i, ppb
[1] $NO_2 + h\nu \rightarrow NO + O$	P	+60
[3] $O_3 + NO \rightarrow NO_2 + O_2$		−60
[28] $NO_2 + OH \rightarrow HNO_3$		−58
[138] $OH + XYL \rightarrow 0.7\ HO_2 + 0.5\ XO_2 + 0.2\ CRES + 0.8\ MGLY + 1.1\ PAR + 0.3\ TO_2$	N	+39
[74] $FORM + h\nu \rightarrow 2\ HO_2 + CO$	P	+31
[88] $C_2O_3 + NO_2 \rightarrow PAN$		−16
[31] $HO_2 + NO_2 \rightarrow PNA$		−15
[30] $HO_2 + NO \rightarrow OH + NO_2$	N	+14
[32] $PNA \rightarrow HO_2 + NO_2$		+14
[87] $C_2O_3 + NO \rightarrow MEO_2 + NO_2$	N	+14
[140] $MGLY + h\nu \rightarrow C_2O_3 + HO_2 + CO$	P	+14
[75] $FORM + h\nu \rightarrow CO$	P	−12
[101] $ALDX + h\nu \rightarrow MEO_2 + CO + HO_2$	P	+12
[128] $TOL + OH \rightarrow 0.44\ HO_2 + 0.08\ XO_2 + 0.36\ CRES + 0.56\ TO_2$	N	+11
[9] $O_3 \rightarrow O_2 + O(^1D)$	P	+9
[10] $O(^1D) + M \rightarrow O + M$	N	−9
[11] $O(^1D) + H_2O \rightarrow 2\ OH$	C	+9
[129] $TO_2 + NO \rightarrow 0.9\ NO_2 + 0.9\ HO_2 + 0.9\ OPEN + 0.1\ NTR$	C	+9
[130] $TO_2 \rightarrow CRES + HO_2$	C	−8
[86] $ALD2 \rightarrow MeO_2 + CO + HO_2$	P	+5
[159] $NO_2 \rightarrow NO_2S$	P	+5
[160] $NO_2S + H_2O \rightarrow OH + HONO$	C	+5

Obviously, if a reaction has either a large positive or negative sensitivity, then it is important to have an accurate determination of its reaction rate. With smaller sensitivities, accurate determination of the reaction rate is perhaps less critical. For example, reaction [28], $OH + NO_2$

+ M $\rightarrow$ HNO$_3$ + M, is the reaction whose rate was recently modified by Mollner, et al., and with a sensitivity of –58 ppb, it is among the most sensitive reactions in the model. The room-temperature revision of its rate constant constitutes a decrease of approximately 15% in the reaction rate. If we can expect a similar decrease at lower temperatures, then we would expect this revision to generate a change of ln(0.85) × (–58 ppb) = +9 ppb in the predicted ozone peak. As already mentioned, the new measurements were only done at 298 K, and the precise extent to which the low-temperature rate should be modified is not clear.

These sensitivities can also be used to indicate useful mitigation strategies. For example, reactions 128 and 138 are the only reactions in the mechanism that involve toluene and xylene respectively, and their respective sensitivities are +39 and +11 ppb. Because both reactions are first-order in toluene and xylene, respectively, then a 10% reduction in the concentration of both is predicted to change the ozone concentration by ln(0.9) × (39 + 11) ppb = –5 ppb.

The formal definition of S_i is shown in Eq. 5-1, where $P(0)$ represents the ozone peak concentration of the base model, $P_i(+)$ and $P_i(-)$ represent the ozone peak concentrations of the models for which reaction i has been accelerated or decelerated by the factors $e^{+0.15} = 1.162$ and $e^{-0.15} = 0.861$.

$$S_i = \frac{1}{2}\left(\frac{P_i(+) - P(0)}{0.15} + \frac{P(0) - P_i(-)}{0.15}\right) = \frac{P_i(+) - P_i(-)}{0.3}$$

(Eq. 5-1)

Eq. 5-1 is equivalent to the numerical estimation of a derivative, so an alternative definition is

$$S_i = \frac{\partial P}{\partial(\ln z_i)}$$

(Eq. 5-2)

where z_i represents the speed of reaction i. In practice, the rate of the reaction can be accelerated by multiplying the acceleration factor $e^{\pm 0.15}$ by all of the coefficients in the rate expression that contain units of time^{-1}. Because the MS-DOS implementation of OZIPR rounds off all P values to the nearest 0.1 ppb, the detection level of S_i by this formula is about ±1 ppb.

5.3 TEMPERATURE DEPENDENCE OF PHOTOLYTIC REACTIONS

CB05 and other standard mechanisms neglect the temperature dependence of photolytic reactions. This is not a problem for summer ozone but does affect the prediction of winter ozone as discussed below. The rate of any photolytic reaction, $j(T)$, is given by Eq. 5-3 (Finlayson-Pitts & Pitts, 2000, p. 76):

$$j(T) = \int_{\lambda_{min}}^{\lambda_{max}} d\lambda\, F(\lambda)\sigma(\lambda,T)\Phi(\lambda,T)$$

(Eq. 5-3)

where $F(\lambda)$ is the actinic flux, $\sigma(\lambda,T)$ is the absorption cross-section, and $\Phi(\lambda,T)$ is the quantum yield (Note: the temperature dependence of each term is explicitly shown). The noontime value of $j(T)$ was calculated for several reactions at different temperatures. Actinic flux values in every case were taken from the 80%-albedo tabulation of Finlayson-Pitts & Pitts (2000, p.71) using the minimum solar zenith angle for the UGRB on Jan. 31, which was 59.8°. Absorption cross-sections and quantum yields are available from two sources, either a pdf document (Sander et al., 2006) or as downloadable text files (Keller-Rudek and Moortgat). The following paragraphs summarize these calculations. The integration resolution was 1 nm, using linear interpolation whenever the tabulated values were not available at that resolution.

Fig. 5-1 displays each integrand of Eq. 5-3, i.e., the product $F\sigma\Phi$, as a function of wavelength for each of the integrations. The final value of each rate constant is equal to the area under the corresponding curve in Fig. 5-1, and is reported in Table 5-2.

- Reaction: $O_3 \rightarrow O_2 + O$ at $T = 218$ K. The integration range is $\lambda \in [290$ nm, 340 nm]; σ data are available in the interval $\lambda \in [196$ nm, 342 nm] from Table 4-5 of Sander et al. (2006), as downloaded directly from Keller-Rudek & Moortgat. The quantum yield splits into two channels: Φ_1 and Φ_2, corresponding to the production of $O(^1D)$ and O, respectively; hence, Φ_2 applies to this reaction. (As a point of clarity, $O(^1D)$ refers to the higher energy "singlet" state of the oxygen atom, and O represents the more common "triplet" state.) An empirical formula is given (Sander et al., 2006, pp. 4-16, 4-17) for Φ_1 in the interval $\lambda \in [306$ nm, 328 nm] and over the temperature range $T \in [200$ K, 300 K]; outside that interval, the recommendations are $\Phi_1 \approx 0.08$ for $\lambda \in [329$ nm, 340 nm] and $\Phi_1 \approx 0.90$ for $\lambda < 360$ nm, both recommendations being independent of temperature. No recommendation is given above 340 nm, except for a warning that Φ_1 might be non-zero. The upper bound for the integration was, therefore, set at 340 nm. Then Φ_2 was calculated as $1 - \Phi_1$.

- Reaction: $O_3 \rightarrow O_2 + O$ at $T = 295$ K. The integration range is $\lambda \in [329$ nm, 340 nm]; σ data are available in the interval $\lambda \in [185$ nm, 825 nm] from Table 4-5 of Sander et al. (2006), and downloaded directly from Keller-Rudek & Moortgat. The source for Φ is the same as at $T = 218$ K.

- Reaction: $O_3 \rightarrow O_2 + O(^1D)$ at both $T = 218$ K and 295 K. Sources for σ and Φ are the same as for the $O_3 \rightarrow O_2 + O$ reaction, except that now the quantum yield corresponds to the Φ_1 channel.

- Reaction: $NO_2 \rightarrow NO + O$, lower T. Absorption cross-sections are available at 220 K, and quantum yields at 248 K. For this calculation, therefore, the temperature will be reported as 234 K. The integration range is $\lambda \in [290$ nm, 422 nm]. σ-data are from Table 4-12 of Sander et al. (2006), and downloaded directly from Keller-Rudek and Moortgat in the interval $\lambda \in [241$ nm, 662 nm]. Φ-data in the interval $\lambda \in [300$ nm, 422 nm] are obtained from Table 4-13 of Sander et al. (2006) and downloaded directly from Keller-Rudek and Moortgat, and extrapolated to 290 nm.

- Reaction: $NO_2 \rightarrow NO + O$, higher T. Absorption cross-sections are available at 294 K, and quantum yields at 298 K. The temperature will be reported as 296 K for this integral.

The integration range is $\lambda \in [290 \text{ nm}, 422 \text{ nm}]$. Sources for σ and Φ are the same as this reaction at lower temperatures.

- Reaction: $H_2O_2 \rightarrow OH + OH$. No σ data are available above 350 nm, while Fig. 5-1 indicates that absorption above 350 nm is significant. Consequently, an extrapolation was applied equivalent to a 15% augmentation of the integral truncated at 350 nm. The integration range is $\lambda \in [290 \text{ nm}, 350 \text{ nm}]$. Two different sources for σ are provided by Sander et al.: a tabulation, Table 4-9, downloadable from Keller-Rudek and Moortgat, and an empirical formula, Table 4-10; both were employed in separate integrations. The source for Φ is Sander, et al. (2006, p. 4-19): "At and above 248 nm the quantum yield for OH production is 2." The relevant yield for the current calculation is production of a pair of OH radicals; therefore, $\Phi = 1$ was employed. All results appearing in Table 5-2 include the 15% correction.

- Reaction: $MeOOH + O_2 \rightarrow HCHO + HO_2 + OH$. No σ data are available above 365 nm, while it appears that absorption still occurs at higher wavelengths; therefore, just as with the hydrogen peroxide reaction, the final integral is augmented by 7%. A temperature is not given; hence, $T \approx 300 \text{ K}$ is assumed. The integration range was set at $\lambda \in [290 \text{ nm}, 365 \text{ nm}]$. σ was obtained from Sander et al., Table 4-37, downloadable from Keller-Rudek and Moortgat. Sander et al., p. 4-53 report that the quantum yield is unity. The result appearing in Table 5-2 includes the 7% correction.

- Reaction: $HCHO + 2O_2 \rightarrow 2HO_2 + CO$. The quantum yield for photodissociation of formaldehyde involves three separate channels, designated channels 1 through 3 by Sander et al. (Channel 2 is considered below; channel 3 will not be considered here.) The current reaction corresponds to channel 1, whose quantum yield is reported to be independent of T and P, and given by an empirical formula (Sander et al., p. 4-44). Cross-section data are available at two temperatures. The integration range is taken to be $\lambda \in [290 \text{ nm}, 365 \text{ nm}]$. σ came from Sander et al., Table 4-30 and 4-31, downloaded from Keller-Rudek and Moortgat.

- Reaction: $HCHO \rightarrow H_2 + CO$. Sander et al. (2006) report that three channels are involved in the photodissociation of formaldehyde, with the current reaction corresponding to channel 2. It is found in Sander et al., Table 4-32, but only tabulated at 298 K, and reported to have a complex temperature dependence. Only a single temperature, therefore, was considered for this reaction. The integration range was set at $\lambda \in [290 \text{ nm}, 361 \text{ nm}]$. σ was obtained from Sander et al., Table 4-30, downloaded from Keller-Rudek and Moortgat.
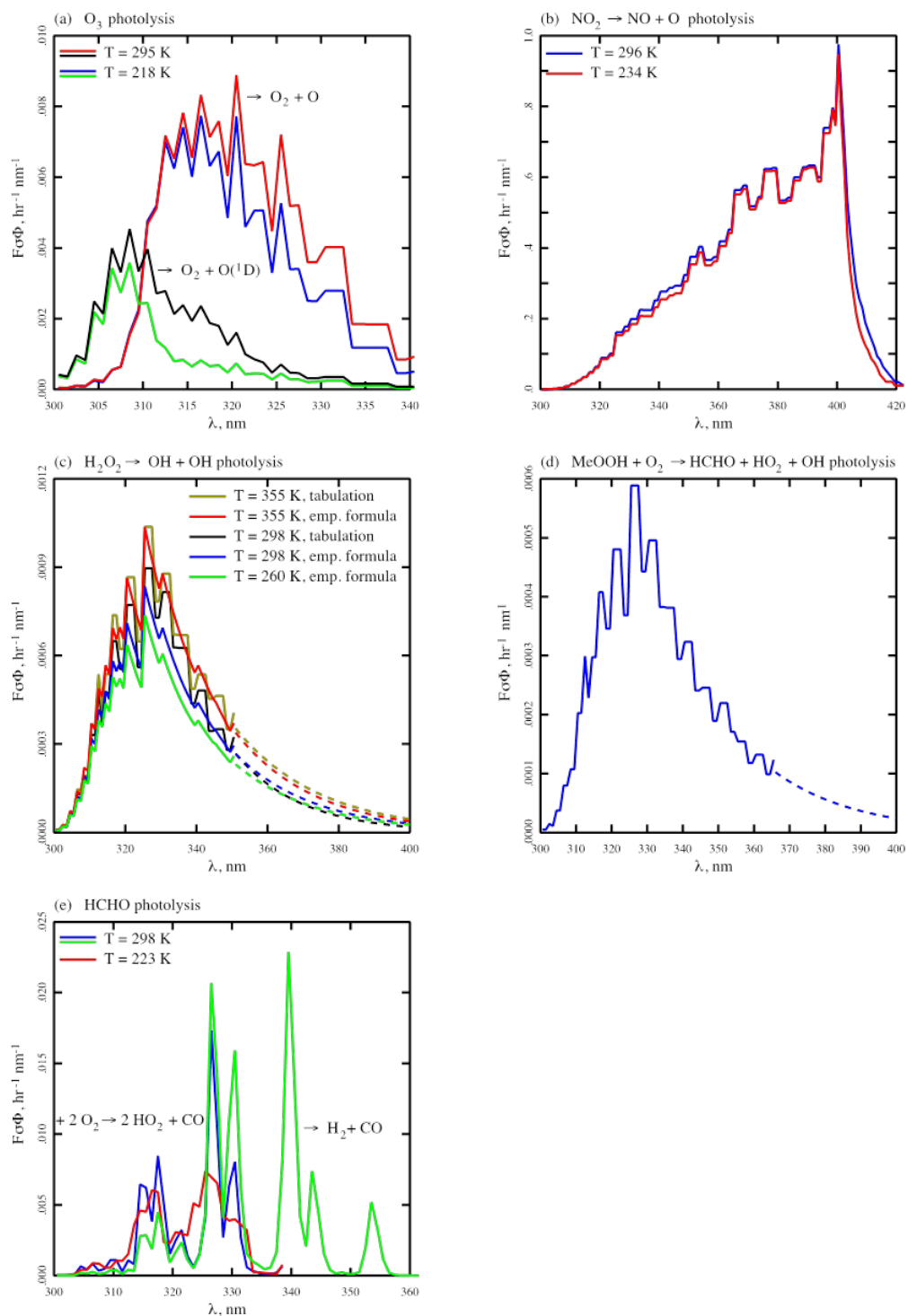
Figure 5-1. The products $F\sigma\Phi$ (F = actinic flux, σ = absorption cross-section, Φ = quantum yield) for the indicated reactions at the indicated temperatures. In panels (c) and (d), dashed curves represent extrapolations explained in the text.

With results at two temperatures, a linear interpolation can be applied to estimate temperature-dependence. Three temperatures are available for the hydrogen peroxide reaction, but in this case there is sufficient scatter that a linear regression is most appropriate. Therefore, we will represent the temperature dependence of photolytic reactions with the following linear formula:

$$j = j_h + \Gamma\left(T - T_h\right)$$

(Eq. 5-4)

j_h is the rate constant at $T = T_h$, while Γ is the slope. Values of j_h and Γ, obtained by linear interpolation or linear regression, are collected in Table 5-2. For comparison, we also display j_{CB05}, or the value of the rate constant as assigned in CB05. There is generally good agreement between j_h and j_{CB05} values; the variation can probably be attributed to use of different data sets for σ and Φ, different assumptions about actinic flux and albedo, or to different conventions in performing the numerical integrations. The one exception to this is the reaction $O_3 \rightarrow O_2 + O$, for which the rate employed in CB05 is about 10 times larger than the rate we calculate. The sensitivity value for this reaction, however, is undetectably low, and a direct modification of the rate by one order of magnitude changes P by only 0.1 ppb.

Table 5-2. Results of computations of photolytic rate constants.

Reaction	j, current result,[a] min^{-1}	j_{CB05}, min^{-1}	j_h,[d] min^{-1}	Γ, min^{-1} K^{-1}	Γ/j_h, 10^{-3} K^{-1}
$O_3 \rightarrow O_2 + O$	2.60×10^{-3} (218) 3.15×10^{-3} (295)	3.56×10^{-2}	3.18×10^{-3} (0.09)	7.2×10^{-6}	2.3
$O_3 \rightarrow O_2 + O(^1D)$	7.43×10^{-4} (218) 1.19×10^{-3} (295)	1.14×10^{-3}	1.22×10^{-3} (1.07)	5.8×10^{-6}	4.8
$NO_2 \rightarrow NO + O$	0.727 (248) 0.768 (296)	0.711	0.772 (1.09)	6.7×10^{-4}	0.86
$H_2O_2 \rightarrow OH + OH$	4.40×10^{-4} (260)[b] 4.98×10^{-4} (298)[b] 5.48×10^{-4} (298)[c] 6.17×10^{-4} (355)[b] 6.22×10^{-4} (355)[c]	5.07×10^{-4}	5.20×10^{-4} (1.03)	1.8×10^{-6}	3.5
$MeOOH + O_2 \rightarrow HCHO + HO_2 + OH$	3.63×10^{-4} (?)	3.63×10^{-4}	N.A. (1.00)	N.A.	N.A.
$HCHO + 2O_2 \rightarrow 2HO_2 + CO$	1.97×10^{-3} (223) 2.07×10^{-3} (298)	1.91×10^{-3}	2.07×10^{-3} (1.08)	1.3×10^{-6}	0.65
$HCHO \rightarrow H_2 + CO$	3.67×10^{-3} (298)	3.29×10^{-3}	N.A. (1.12)	N.A.	N.A.

[a]Kelvin temperature appears in parentheses. [b]Empirical formula, Sander et al., Table 4-10. [c]Tabulation, Sander et al., Table 4-9. [d]The quantity in parentheses is the ratio j_h/j_{CB05}.

Note that the values of Γ, as calculated for five different reactions, are always positive. This indicates that each of the photolytic reactions is slower at lower temperatures. Note also that the rates j can vary over several orders of magnitude; nevertheless, the value of Γ/j_h is relatively invariant, with a median value of about 0.002 K^{-1}. Taking this value to be typical of all photolytic reactions in the mechanism, and using the sensitivity values defined in the previous

section, we can estimate the severity of neglecting the temperature dependence of these reactions. The corrected estimate of the ozone peak concentration is given by Eq. 5-5:

$$P = P(0) + \sum_i \frac{\partial P}{\partial(\ln j_i)} \frac{\partial(\ln j_i)}{\partial T}(T_c - T_h)$$

(Eq. 5-5)

where $P(0)$ represents the ozone peak in the base model, $P(0) = 122.5$ ppb. The sum extends over all of the photolytic reactions in the mechanism. Note that the first partial derivative is S_i, and the second partial derivative is Γ/j_h for the ith reaction, which is estimated as 0.002 K^{-1}. CB05 has 11 photolytic reactions with detectable sensitivities, $\sum_i S_i$ for these 11 reactions is +131 ppb. We estimate, therefore, that

$$\Delta P = (0.002\,K^{-1}) \times (-36\,K) \times (131\,ppb) = -9\,ppb$$

(Eq. 5-6)

A more accurate determination of the effect can be achieved by modifying the base mechanism. Let j_{CB05} represent the base rate for any particular photolytic reaction as it is defined in CB05. We assume that its value in the lower temperature range can be estimated as

$$j*_{CB05} = j_{CB05}\left[1 + \left(\frac{\Gamma}{j_h}\right)(T_c - T_h)\right]$$

(Eq. 5-7)

Γ/j_h has only been determined for 5 reactions; for all others, we use the estimate 0.002 K^{-1}. Let CB05* represent the mechanism for which all photolytic reactions are modified in this way, and for which all other reactions maintain the same rate expressions as in CB05. When the base model is run with the CB05* mechanism, we obtain

P(CB05*) = 115.8 ppb

(Eq. 5-8)

or a decrease of 6.7 ppb. (The main reason that this correction is smaller than that of Eq. 5-6 is that the most sensitive reaction, that of NO$_2$, has a Γ/j_h value smaller than 0.002 K^{-1}.)

5.4 REACTIONS WITH NEGATIVE ACTIVATION ENERGIES

As mentioned above, it is conjectured that the reactions with negative activation energies might be giving poor extrapolations at lower temperatures. The empirical rate law is written

$$k = A \exp\left(\frac{-E_{ae}}{T}\right)$$

(Eq. 5-9)

(We report all activation "energies" in Kelvin units – the activation energy divided by the gas constant.) Fig. 5-2 is based on the reaction OH + XYL (hydroxyl radical and xylene), which has the highest sensitivity, +39 ppb, among all the reactions with negative activation energies. In CB05, its rate expression is shown in Eq. 5-9 with Arrhenius parameters $E_{ae} = -116$ K and $A = 0.17 \times 10^{-10}$ cm^3 molecule^{-1} min^{-1}. A more appropriate extrapolation law could be a "power-Arrhenius" law:

$$k = B \left(\frac{T}{T_h} \right)^x \exp\left(\frac{-E_a}{T} \right)$$

(Eq. 5-10)

where E_a is constrained to be positive. Given some constrained value of E_a, we determine B and x such that the two curves are tangent at $T = T_h$. This implies

$$\ln B = \ln A + \frac{(E_a - E_{ae})}{T_h} \quad \text{and} \quad x = \frac{(E_{ae} - E_a)}{T_h}$$

(Eq. 5-11)

For the OH + XYL example, employing $E_a = +300$ K gives $x = -1.387$ and $B = 0.6803 \times 10^{-10}$ cm^3 molecule^{-1} min^{-1}. Fig. 5-2 shows that the two curves are respectively concave up and concave down, and that they are detectably different at $T = T_c$. The power-Arrhenius extrapolation at T_c is 1.2% lower than the Arrhenius extrapolation. With a sensitivity of +39 ppb, the adjustment in this reaction alone will lead to a –0.5 ppb change in the ozone peak concentration.

OZIPR calculations were made to illustrate this effect, and rather than replace the existing Arrhenius law with a power-Arrhenius law, a new Arrhenius law was used:

$$k = A' \exp\left(\frac{-E'_{ae}}{T} \right)$$

(Eq. 5-12)

This was chosen to be tangent to the power-Arrhenius law at $T = T_c$. The parameters of the new law obey

$$E'_{ae} = T_c x + E_a$$

(Eq. 5-13)

and

$$\ln A' = \ln B - \frac{(E_a - E'_{ae})}{T_c} + x \ln\left(\frac{T_c}{T_h} \right)$$

(Eq. 5-14)

This modification was applied to all the Arrhenius laws that appear in the CB05* mechanism with negative activation energies, using three different values of E_a calculated at different

temperatures: $E_a = 0$ K, 200 K, and 300 K. The three modifications of the mechanism were denoted CB05*0, CB05*2, and CB05*3, respectively, and resulted in the following peak ozone concentrations:

P(CB05*0) = 115.5 ppb;   P(CB05*2) = 115.2 ppb;   P(CB05*3) = 115.0 ppb   (Eq. 5-15)

These results show that this modification of the mechanism has a weaker effect, less than 1 ppb for the cases we examined.
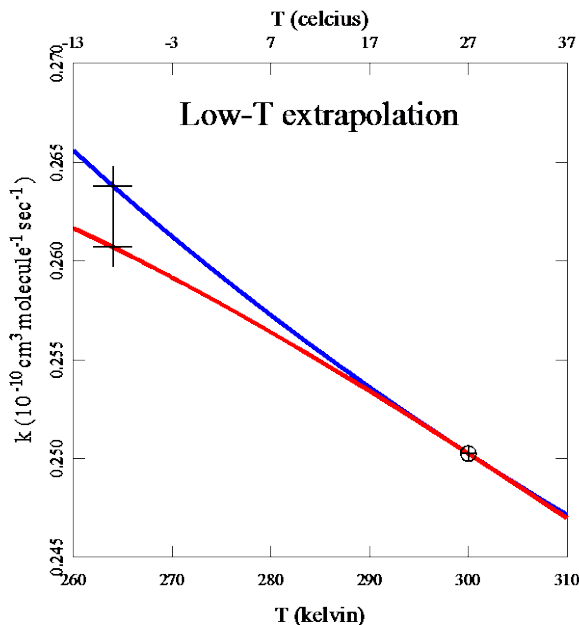
Figure 5-2. An Arrhenius law with negative activation energy (blue) overestimates the rate constant at low temperature.

5.5   REACTIONS WITHOUT TEMPERATURE DEPENDENCE

We now examine the effect of another modification of the CB05 mechanism. Approximately 40 reactions appear in the mechanism without any temperature dependence. Several of these have sensitivities approaching ±10 ppb (See Table 5-1). In most cases, this probably means that the reaction has only been measured near T_h. The following discussion shows the change in the predicted ozone peak concentrations if a typical Arrhenius structure is used for these reactions.

One way to estimate the effect is to assume that all the reactions in question have precisely the same activation energy. For consistency with other reactions, we will assume an activation energy, $E_a = 336$ K, which is the average activation energy taken of all the Arrhenius reactions in the mechanism. The change in the peak ozone concentration is given by Eq. 5-16:

$$\Delta P \approx \sum_i \frac{\partial P}{\partial (\ln k_i)} \Delta (\ln k_i) \approx \sum_i \frac{\partial P}{\partial (\ln k_i)} E_a \left(\frac{1}{T_h} - \frac{1}{T_c} \right)$$

(Eq. 5-16)

where the sum extends over all of the reactions appearing without temperature-dependence. The partial derivative corresponds to our definition of sensitivity, S_i. In addition,

$$\Delta \ln k_i = E_a \left(\frac{1}{T_h} - \frac{1}{T_c} \right) = -0.153$$
(Eq. 5-17)

The net sum of S_i over all the relevant reactions is +19 ppb. Therefore, our prediction is a –2.9 ppb change in the maximum ozone level:

$$P(\text{CB05*3*}) = 112.1 \text{ ppb}$$
(Eq. 5-18)

where "CB05*3*" denotes this latest version of the mechanism.

Monte Carlo techniques were also used to investigate the assumption of a single activation energy. In each independent Monte Carlo calculation, the activation energy was selected from a normal distribution with a pre-specified mean $\langle E_a \rangle$ and standard deviation σ. The rates of all other reactions were given by the CB05*3 modification described above. Separate runs were performed with $\langle E_a \rangle$ = ±336 K, ±200 K, ±100 K, and 0 K; and with σ = 1620 K, 1000 K, and 100 K. +336 K and 1620 K are the mean and standard deviation, respectively, of all of the Arrhenius laws in the original CB05 mechanism. Therefore, for the run at $\langle E_a \rangle$ = +336 K and σ = 1620 K, the proposed Arrhenius expressions are drawn from a spectrum of values that is typical of and statistically similar to the known Arrhenius expressions. Additional runs with different values of $\langle E_a \rangle$ and σ illustrate the dependence on the activation energy spectrum. Each separate run included 10,000 simulations. Fig. 5-3 shows the distribution in simulated ozone obtained for $\langle E_a \rangle$ = +336 K and σ = 1620 K. The mode of each Monte Carlo distribution, $P(\text{mode})$ (the most probable value of P or maximum in the distribution) is well represented by a variant of Eq. 5-16,

$$P(\text{mode}) \approx P(CB05*3) + \sum_i S_i \langle E_a \rangle \left(\frac{1}{T_h} - \frac{1}{T_c} \right) \approx P(CB05*3) - \langle E_a \rangle \left(0.0086 \frac{ppb}{K} \right)$$
(Eq. 5-19)

while the standard deviation of each distribution is approximately proportional to the standard deviation in the input activation energies:

$$\sigma(P) = \left(0.007 \frac{ppm}{K} \right) \sigma$$
(Eq. 5-20)

Therefore, the most probable P is still given by equations such as 5-16 or 5-19 and, therefore, at about $P(\text{CB05*3*})$ = 112.1 ppb. Uncertainty in individual activation energies (σ = 1620 K), however, generates uncertainty in the final value of the ozone maximum concentration, with a standard deviation of $\sigma(P)$ = 11 ppb.

5.6 SUMMARY

Winter ozone events have been observed in both the Uinta Basin in Utah and the UGRB in Wyoming. Modeling of these events relies on chemical mechanisms such as CB05 that were originally designed for predicting summer ozone concentrations. During the modeling efforts of this project, three areas of concern were identified with applying CB05 at lower temperatures, and calculations were performed to estimate the severity of each of these concerns. For these calculations, a base model was designed to simulate a late-winter day, Feb. 20, 2008 in the Upper Green River Basin (Tonnesen, 2011). Table 5-3 and Fig. 5-3 summarize the results of these calculations.

The first concern is that CB05 neglects temperature-dependence of all photolytic reactions. The temperature-dependence was calculated for five different reactions, which show that photolytic reactions slow down by roughly 1% for each 5 K drop in temperature. This slowdown decreases the predicted ozone concentration by about 7 ppb when the temperature changes from 27° C to -10° C (Table 5-3 and Fig. 5-3).

The second concern is that many reactions in CB05 appear with negative activation energies. If we assume that the true activation energies are positive and that the negative activation energy reflects a temperature dependence of the pre-exponential factor (Tonnesen, 2011), it follows that extrapolations to lower temperatures might not be valid. Consequently, "power-Arrhenius" rate laws were used to obtain new low-temperature extrapolations. The effect in this case is estimated to be weak, resulting in changes in predicted ozone concentrations of less than 1 ppb.

The third concern is that many reactions appear in the mechanism with no temperature dependence at all. The obvious conclusion is that most, if not all, of the reaction rates were only measured at a single temperature in the vicinity of 300 K. There are two possible approaches to estimating these rate constants at lower temperatures. The first approach is to assume that they all have the same constant activation energy set equal to the mean of all other tabulated activation energies in the mechanism, resulting in an additional 3 ppb decrease in the predicted ozone levels (See Table 5-3 and Fig. 5-3). The second approach is to assume a spectrum of activation energies for these reactions that was typical of all the tabulated activation energies in the mechanism. This approach was applied in Monte Carlo calculations, with the result that the most-probable value of predicted ozone concentrations agrees well with the value obtained for the constant activation energy case (the same –3 ppb change), but that predicted ozone concentration now has an uncertainty of about 11 ppb (one standard deviation).

The incremental differences in simulated ozone levels discussed previously are shown in Fig. 5-3 as vertical bars of different colors. The white bar shows the base prediction obtained using the unmodified CB05 mechanism. The yellow bar shows the prediction of the CB05*3 mechanism, with the modifications accounting for temperature-dependence of photolytic reactions and reactions with negative empirical activation energies. The red bar displays the prediction of the CB05*3* mechanism, with the above modifications and the modification that any reaction appearing without temperature dependence follows an Arrhenius law with a typical activation energy. The complete bar graph displays the prediction based on the assumption that activation energies for reactions appearing without temperature dependence may be drawn from a typical spectrum of activation energies. These incremental adjustments also appear in Table 5-3. According to the final distribution in Fig. 5-3, there is an 80% chance that a mechanism with the

discussed modified temperature dependence will predict ozone values lower than the values predicted with the original CB05 mechanism.

It is our recommendation that the CB05 mechanism be modified to incorporate the recent measurements of the $OH + NO_2 + M$ reaction. Such a modification will probably produce an increase of 5 to 10 ppb in the predicted ozone peak concentrations (see Mollner et al., 2010 as well as calculations summarized above). All calculations discussed in this report, however, employed the standard CB05 mechanism, in part at least because the new measurements were only done at room temperature. To a first approximation, revision of the rate parameters for this reaction would apply equally to all of the results summarized in Fig. 5-3 or Table 5-3. Finally, our calculations indicate that the rate expression in CB05 for the photolytic reaction $O_3 \rightarrow O_2 + O$ is about a factor of 10 too large; however, the sensitivity of the CB05 mechanism to this reaction, at least relative to the calculations for this project, is very low, and revisions to this reaction did not affect our results.

It is hoped that these results will stimulate additional interest in measuring reaction rates at lower temperatures. The reactions listed in Table 5-1, especially those designated as "suspicious" and having large sensitivities, deserve special attention.

Table 5-3. Estimates of the effects of including improved temperature-dependence on predicted winter ozone concentrations.

| Description	Designation	[O3] max, ppb
Base model	CB05	123
With temperature-dependent photochemistry.	CB05*	116
With power-Arrhenius extrapolation when empirical activation energy is negative.	CB05*0	116
	CB05*2	115
	CB05*3	115
With 336 K activation energy applied to all temperature independent non-photo reactions.	CB05*3*	112
Random activation energies assigned to all temperature independent non-photo reactions.		112 ± 11 (one s.d.)
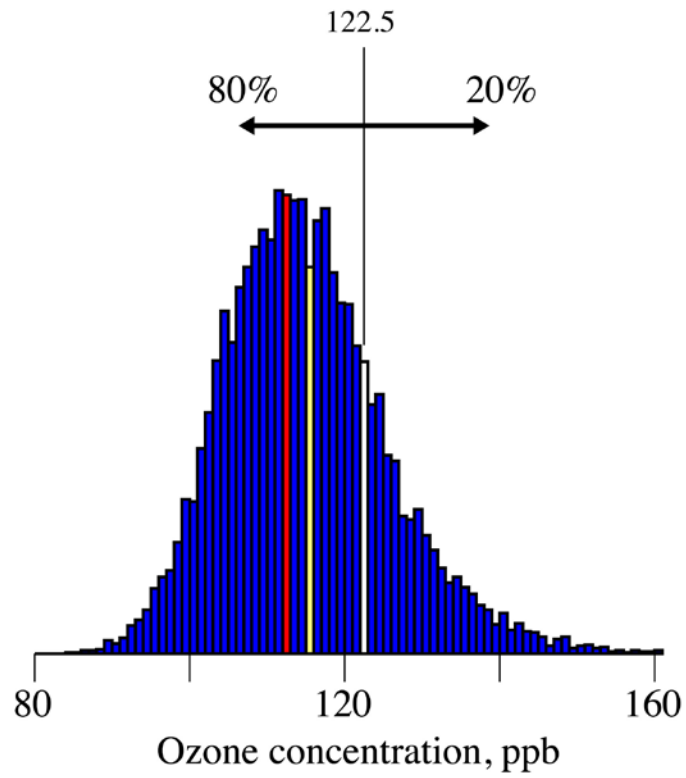
Figure 5-3. Predicted ozone concentration showing the effect of incremental adjustments in the mechanism.

6.   SUMMARY/CONCLUSIONS

The results of the Basin-wide winter ozone study showed that elevated wintertime ozone concentrations were observed throughout most of the Uinta Basin during wintertime inversion events. The inversion events have the effect of reducing the movement of ozone precursors, resulting in increased ozone formation below the inversion layer. Although the data collected for this study cannot be used for regulatory purposes, the elevated ozone levels resulted in a high number of 8-hr exceedances at multiple locations throughout the Basin, with the fewest exceedances occurring in the higher elevations along the periphery of the study area. The highest ozone values typically were observed in the area centered along the Ouray/Pariette Draw locations and extending north to the Cedarview/Lapoint area, east to the Red Wash area, and west to Duchesne. The highest 1-hr value was observed at Ouray (149 ppb), and Pariette Draw was the site of both the highest observed 8-hr value (134.6 ppb) and the greatest observed fourth-highest (regulatory) ozone value (121.6 ppb). The highest number of 8-hr exceedances (25) was observed at both the Ouray and Horse Pool sites. And while Fruitland and Nine Mile Canyon were the only sites to show no exceedances of the 8-hr standard, the Altamont, Rabbit Mountain, and Rangely, CO, sites (one, three, and three exceedances, respectively) would also be considered attainment areas under the current ozone NAAQS.

The study indicated that two factors, proximity to oil/gas wells and elevation, figured prominently in ozone concentration levels at a given location. Closer proximity to oil/gas wells resulted in higher ozone levels, with the exception of those locations at higher elevations which were probably above the top of the inversion layer that occurred at ~5500 to 6000 ft. Only a limited number of vertical ozone profiles were measured, but these showed higher levels of ozone near the ground, indicative of a local formation rather than an external transportation of ozone precursors into the Basin.

NO_x measurements were highest at the Vernal location but at levels typically observed in rural/semi-urban areas. NO_x measurements also displayed a typical traffic-related diurnal profile. All observed levels of NO_2 were well below the NAAQS (100 ppb maximum, 1-hr average). The observed dominance of NO_2 suggests the presence of a readily oxidized air mass, which indicates sufficient available ozone or other oxidants to convert initially emitted NO to NO_2.

The observed CH_4 concentrations at Vernal were consistent with Northern Hemispheric background levels (1.7-1.8 ppm); however, the CH_4 concentrations measured at the Red Wash site (2.7-5.5 ppm) were significantly above the Northern Hemispheric background levels. CH_4 is usually considered non-reactive due to its relative slow reaction rates, but at levels observed at the Red Wash site, CH_4 could be a significant player in atmospheric photochemistry of ozone formation. NMHC measurements at the Red Wash location also were more than twice the observed concentrations at the Vernal site. The observed ratio of indicator compounds, benzene-to-toluene, is suggestive of oil and gas exploration and production.

Observed $PM_{2.5}$ concentrations were well below the NAAQS (35 $\mu g/m^3$) at both the Vernal and Red Wash sites, but concentrations at the Vernal location were approximately twice those of the Red Wash location. These results are inconsistent with previous UDAQ measurements in the mid-2000s that observed some exceedances of NAAQS. The chemical composition of the particulate matter measured at both sites was approximately 80% carbonaceous material, with

just under 70% being organic carbon (as opposed to elemental/black carbon). This percentage indicates an abundance of long-chain VOCs characteristic of the oil and gas industry.

Measurements of vertical meteorology at the Red Wash site indicate that during an inversion event, the mixing height (surface layer) was on the order of 20-80 m agl (65-265 ft agl) and was dependent on time of day. This conclusion was also supported by vertical ozone measurements at the Red Wash location. Meteorological data collected from ground stations throughout the Basin indicate that horizontal winds were generally light (< 2 m/s) during observed inversion conditions. The higher elevation stations (> 6500 ft asl) showed more between-station consistency for both wind direction and wind speed. These higher elevation areas were probably located above the inversion and under the influence of regional wind patterns.

7.   REFERENCES

[Carter 2010] W.P.L. Carter, "Development of the SAPRC-07 Chemical Mechanism and Updated Ozone Reactivity Scales," Report to the California Air Resources Board, www.cert.ucr.edu/~carter/SAPRC.

[Dodge 2000] M.C. Dodge, "Chemical oxidant mechanisms for air quality modeling: critical review," Atmospheric Environment, 34, 2103-2130 (2000).

[Finlayson-Pitts & Pitts, 2000] B.J. Finlayson-Pitts and J.N. Pitts, *Chemistry of the Upper and Lower Atmosphere*, Academic Press, London, 2000.

[Gery et al., 1989] M.W. Gery, G.Z. Whitten, J.P. Killus, M.C. Dodge, "A Photochemical Kinetics Mechanism for Urban and Regional Scale Computer Modeling," Journal of Geophysical Research, 94, 12925-12956 (1989).

[Keller-Rudek and Moortgat] H. Keller-Rudek and G.K. Moortgat, *UV-VIS Spectral Atlas of Gaseous Molecules*, Max-Planck-Institut für Chemie, Mainz, Germany, http://www.atmosphere.mpg.de/enid/2295

[Mollner et al., 2010] A.K. Mollner, S. Valluvadasan, L. Feng, M.K. Sprague, M. Okumura, D.B. Milligan, W.J. Bloss, S.P. Sander, P.T. Martien, R.A. Harley, A.B. McCoy, W.P.L. Carter, "Rate of Gas Phase Association of Hydroxyl Radical and Nitrogen Dioxide," Science, 330, 646-649 (2010).

[Sander et al., 2006] S.P. Sander, R.R. Friedl, D.M. Golden, M.J. Kurylo, G.K. Moortgat, H. Keller-Rudek, P.H. Wine, A.R. Ravishankara, C.E. Kolb, M.J. Molina, B.J. Finlayson-Pitts, R.E. Huie, V.L. Orkin, "*Chemical Kinetics and Photochemical Data for Use in Atmospheric Studies, Evaluation Number 15*," JPL Publication 06-2 (2006), PDF version available for download at: http://jpldataeval.jpl.nasa.gov

[Sarwar et al., 2008] G. Sarwar, D. Luecken, G. Yarwood, G.Z. Whitten, W.P.L. Carter, "Impact of an Updated Carbon Bond Mechanism on Predictions from the CMAQ Modeling System: Preliminary Assessment," Journal of Applied Meteorology and Climatology, 47, 3-14 (2008).

[Seinfeld & Pandis, 2006] J.H. Seinfeld and S.N. Pandis, *Atmospheric Chemistry and Physics*, 2nd Ed., Wiley, Hoboken, New Jersey (2006).

[Tonnesen 2011] Private communications with Dr. Gail Tonnesen, EPA District 8, Denver, CO.

[Yarwood et al. 2005] G. Yarwood, S. Rao, M. Yocke, G.Z. Whitten, "Updates to the Carbon Bond Chemical Mechanism: CB05," Final Report to the EPA, RT-04-00675, www.camx.com.

8.   RECOMMENDED FUTURE WORK

8.1   OVERVIEW

One of the main objectives of this first year study was to provide insights and direction for the design of a future, multi-year program to mitigate ozone levels in the Uinta Basin. The program would have two main components:

1. The design and implementation of a multi-year air quality study to provide sufficient understanding of ozone reactions in the Uinta Basin; and
2. The design, implementation, and validation of a mitigation strategy specific to the Uinta Basin based on the results of this and future air quality monitoring and modeling studies.

The list of tasks is intended only as a starting point for discussion of a more detailed task list to be assembled by stakeholders currently engaged in discussions regarding broader air quality management strategies. The broader strategies under consideration include (1) the creation of a Memorandum of Understanding between the Bureau of Land Management, the Department of Agriculture, and the Environmental Protection Agency; (2) the implementation of the Utah Governor's 10-year Energy Plan and Seven-Point Plan to address air quality in Utah; and (3) the implementation of the Bureau of Land Management's proposed Air Resources Management Strategy (ARMS) which includes recommendations of a regional photochemical grid model, robust monitoring program, and pollution controls/mitigation measures. The decisions reached on each of these important strategies will depend on the tasks being recommended in this document, including funding and designation of a responsible agency.

8.2   STAKEHOLDERS

Below is a list of potential stakeholders who might play key roles in the future study in such areas as leadership, design, monitoring, analysis, policy design and implementation, results interpretation, and so on. It is recommended that a lead agency (i.e., UDEQ) bring together representatives of each stakeholder group to solicit input on the design and implementation of an air quality program for the Uinta Basin. Such a strategic program will prove much more efficient and cost-effective if supported by all stakeholders and if all existing data is made available for the study.

8.2.1   State of Utah

Utah Department of Environmental Quality (UDEQ), Department of Natural Resources (DNR) Department of Oil, Gas, and Mining (DOGM), School Institutional Trust Lands Administration (SITLA), Utah Science Technology and Research Initiative (USTAR).

8.2.2   Federal Agencies

U.S. Bureau of Land Management (BLM), U.S. Environmental Protection Agency (EPA-Region 8), U.S. Forest Service (USFS).

8.2.3　Industry

Western Energy Alliance, National Oil Shale Association

8.2.4　Ute Indian Tribe

8.2.5　Local Government and Local Health District

Uintah County, Duchesne County, Carbon County, Uintah Impact Mitigation Special Service District, TriCounty Health Department

8.2.6　Research Institutes

Several universities and organizations in the state of Utah have a wealth of experience in air quality studies and could contribute significantly to this program. Utah State University/Energy Dynamics Laboratory (including the USU Uintah Basin Regional Campus) performed the initial study for ozone monitoring discussed previously.

8.3　TASKS

To accomplish project objectives, the proposed tasks are outlined below. The schedule of the various tasks will depend on available funding and on the results of related tasks.

8.3.1　Task 1: Air Quality Monitoring Program

- Perform detailed wintertime ozone, NO_y, and VOC chemistry at receptor and source locations to determine region-specific photochemistry and limiting reactions.
  - o Designate Horse Pool and Roosevelt as primary study sites.
  - o Obtain statistical confidence over a two to three year period.
  - o Deploy cooperative team from USU, EDL, UDAQ, NOAA, EPA, BLM and others.
- Expand ozone survey network to verify the winter 2010-11 study and to procure understanding of untested areas, particularly in the Basin's southern region. In addition to ozone concentrations, ozone precursor pollutants (NO_x and VOCs) and meteorological conditions should be measured at locations collocated with the ozone measurements.
  - o Utilize up to 20 ozone stations to be operated by project investigators.
  - o Include four to six additional sites to be operated by other agencies/groups (e.g., BLM, NPS, Golder Associates, etc.).
  - o Collocate passive NO_x and VOC samplers with ozone survey monitors to assess generalized precursor plumes and concentrations (week-long exposure).
  - o Install meteorological instrumentation at ozone monitor locations (utilizing pre-existing met stations when possible).
  - o Assess potential for a similar summertime ozone/air quality survey (to date, there is no evidence of a summertime concern in the Uinta Basin).

8.3.2 Task 2: Air Quality Modeling Program

- Develop and apply OZIPR (EPA-approved ozone chemistry modeling package) for the Uinta Basin.
- Adapt photochemical grid models (CAM_x, CMAQ, etc.) to the Basin (would require parallel or pre-development of an acceptable meteorological model, e.g., WRF).
- Validate photochemical grid models using monitoring data (Task 1).
- Apply validated grid models to investigate Basin air quality characteristics:
  - Outside transport of precursors
  - Elevation effects

8.3.3 Task 3: Policy Development

- Create focus group with stakeholders previously discussed.
- Develop industry credit program for implementing Best Available Practices (BAP) to mitigate impacts to air quality.
- Develop mitigation policy.

8.3.4 Task 4: Winter Ozone Assessment Program

- Complete detailed review of winter ozone studies performed in UGRB of Wyoming to determine if any information can benefit efforts in the Uinta Basin.

8.3.5 Task 5: Emissions Inventory of Ozone Precursors

- Develop understanding of major sources of ozone precursors in the Uinta Basin to prepare for the development of a mitigation strategy for reducing ozone levels.
- Perform preliminary assessment of ozone precursor sources in the Uinta Basin.
- Quantify significant ozone precursor sources.
- Measure fugitive emissions from representative sources of ozone precursors.
- Facilitate industry self-assessment of pollutant emissions.
- Characterize produced water ponds during winter and summer periods.

8.3.6 Task 6: Mitigation Potential Assessment

- Perform detailed study of mitigation efforts in Wyoming's UGRB.
- Encourage industry to perform self-assessment of pollutant emissions:
  - Improve drilling (consolidated)
  - Improve transportation (consolidated)
  - Implement Best Available Practices (BAP)
- Conduct study of potential Basin-wide mitigation options.
- Conduct study of available and emerging technologies for relevant mitigations options.
- Implement and validate mitigation options at specific locations.
- Apply validated photochemical grid models to specific mitigation options.

8.3.7   Task 7: Basin Pollutant Mitigation Strategies Development

- Design Basin-wide mitigation plan based on results of Task 5.
- Apply validated photochemical grid models to Basin-wide mitigation plan.
- Refine Basin-wide mitigation plan using modeling results.

8.3.8   Task 8: Basin Pollutant Mitigation Strategies Implementation

- Perform precursor and ozone monitoring at representative locations prior to implementing mitigation strategy.
- Implement Basin-wide mitigation plan.
- Perform precursor and ozone monitoring at representative locations after implementing mitigation strategy.

8.3.9   Task 9: Air Quality Modeling Program (incorporate most recent monitoring data)

- Continue utilization of OZIPR for the Uinta Basin.
- Continue application of photochemical grid models (CAM_x, CMAQ, etc.).
- Continue validation of photochemical grid models using all monitoring data.
- Continue application of grid models to characterize Basin air quality.

9.   APPENDIX

The compiled, hourly averaged ozone concentrations for the winter 2010-11 study sites are available online at http://uintahbasin.usu.edu/htm/edl.

For more information, please contact the following:

Dr. Scott C. Hill, Program Manager

Utah State University Research Foundation
Energy Dynamics Laboratory
Eastern Utah Field Operations
320 North Aggie Boulevard
Vernal, Utah 84078
(435) 722-1766
scott.hill@energydynamicslab.com

Dr. Randal Martin, Technical Manager

Dept. of Civil & Environmental Engineering
Utah State University
Utah Water Research Laboratory
8200 Old Main Hill
Logan, UT 84322
(435) 797-1585
randy.martin@usu.edu